UNIVERSITÀ
DEGLI STUDI
FIRENZE
DINFO
DIPARTIMENTO DI
INGEGNERIA
DELL'INFORMAZIONE

Advanced Multiresolution Bayesian Methods and SAR Image Modelling for Speckle Removal

by

Alessandro Lapini

Submitted to the Department of Information Engineering
in partial fulfillment of the requirements for the degree of

DOCTOR OF PHILOSOPHY

in Computer Science, Systems and Telecommunications

Cycle XXVI, Disciplinary Scientific Area ING-INF/03

February 2014

Author .....
Department of Information Engineering
December 28, 2013

Certified by .....
Fabrizio Argenti
Associate Professor, Thesis Supervisor

Certified by .....
Luciano Alparone
Associate Professor, Thesis Supervisor

Accepted by .....
Luigi Chisci
Ph. D. Coordinator

Years 2011/2013

Acknowledgments

I would like to express my thanks to my supervisors, Prof. Fabrizio Argenti and Prof. Luciano Alparone, and to Dr. Tiziano Bianchi for their guidance during the course of my doctoral studies.

I would like to specially thank Dr. Gianluca Montani, for being my Virgilio on the dark side of the moon.

I am very grateful to my mom for her endless support. Last, but not least, I am very grateful to Benedetta for her love and patience, day–by–day at my side during the last five years.

Contents

Chapter 1

Introduction

1.1 Motivation of the work

A synthetic aperture radar (SAR) is a coherent micro-wave remote sensing system which offers a number of advantages over optical remote sensing, mainly the all-day, all-weather acquisition capability. However, the main drawback of SAR images is the presence of a signal dependent granular phenomenon, that is usually called *speckle*. Speckle is inherent of all active coherent imaging systems and it is a radiometric feature of the imaged terrain, but it visually degrades the appearance of images. Furthermore, it may severely diminish the performances of automated scene analysis and information extraction techniques, as well as it may be harmful in applications requiring multiple SAR observations. For these reasons, speckle is considered as noise in incoherent SAR imaging; hence, a preliminary processing of real-valued detected SAR images aimed at speckle reduction, or *despeckling*, is of crucial importance for a number of applications. On the other hand, despeckling methods are required to preserve some features like local mean of backscatter, point targets and textures, in order to avoid the loss of informations useful for further processing.

A steadily increasing number of papers specific on despeckling has appeared in the literature over the last ten years, presumably because the new generation of satellite SAR systems has dramatically raised the attention of researchers in signal processing towards this problem. The COSMO-SkyMed constellation–four satellites launched by the Italian Space Agency (ASI) between 2007 and 2010–features X-band SAR with low revisit-time; as a second generation mission, two additional satellites are foreseen in 2014 and 2015. The twin-satellite constellation TerraSAR-X/TanDem-X (2007/2010) launched by the German Space Agency (DLR) and the upcoming Sentinel-

1a/-1b satellite constellation (2013/2015) from the European Space Agency (ESA), which shall extend the EnviSat mission, complete the European scenario of satellite SAR. Also, the Canadian RADARSAT 3 mission is expected in a near future, with 3 satellites operating at C-band, to be launched in 2017.

The most recent advances in despeckling pursue the technological objective of giving an extra value to the huge amount of data that are routinely collected by current and upcoming SAR systems mounted on orbiting platforms. In fact, with the exception of applications related to production of digital elevation models (DEMs) or interferometric phase maps useful for studies of terrain deformation (landslides, subsidence, etc..), SAR data do not find the same full utilization, as optical data do, by either users' or scientists' communities. As an example, the functional development of efficient techniques for fusion between optical and SAR data would constitute an enabling technology that would allow a relevant number of new applications to bring benefits both for data providers and for producers of software applications. Unfortunately, speckle is the main obstacle towards the development of an effective optical SAR fusion, together with the different acquisition geometry of optical and SAR systems.

In this thesis the overall results of the study that has been carried out within the topic of SAR images despeckling during the Ph.D. Course are presented. In the first part, the class of Bayesian estimators in the undecimated wavelet domain are discussed, proposing some interesting despeckling filters and analysing their performance with different image formats. The second part of this thesis is dedicated to other topics related to the despeckling: the removal of correlated speckle and the quality assessment for the despeckling. In the former issue, a solution that allows to improve the performances of filters designed for uncorrelated speckle is proposed, demonstrating that, under some assumptions, it is formally the optimal solution; in the latter case, the problem of assessing the quality of despeckled images is analyzed and a method based on the scatter plot which does not require the reference image is presented.

1.2 Organization of the thesis

The achievements and the results presented in this thesis have been also published in specific magazine, journal or conference papers. In the following, the list of topics and the relative contribution to publications is presented.

Chapter 2: Signal models for despeckling of SAR images

The first part of this chapter is dedicated to the fundamentals modeling of reflectivity, speckle and SAR imaging system, which are introduced under a signal processing perspective. In the second part, the most used models of SAR data exploited for despeckling applications are introduced

This chapter is mainly based on the following paper:

- F. Argenti, A. Lapini, T. Bianchi, and L. Alparone, "A tutorial on speckle reduction in synthetic aperture radar images," *IEEE Geoscience and Remote Sensing Magazine*, vol. 1, no. 3, pp. 6–35, 2013.

Chapter 3: Bayesian methods in the wavelet domain

The adoption of the Bayesian estimation framework and the introduction of the multiresolution analysis for the despeckling are presented in the first part of this chapter, with a specific attention to the undecimated wavelet transform domain. In the second part, despeckling filters working in the undecimated wavelet domain are proposed and compared. A fast filter adopting classification of wavelet coefficients is proposed in the third part of the chapter and its performance is shown by means of experimental results.

This chapter is mainly based on the following papers:

- F. Argenti, A. Lapini, T. Bianchi, and L. Alparone, "A tutorial on speckle reduction in synthetic aperture radar images," *IEEE Geoscience and Remote Sensing Magazine*, vol. 1, no. 3, pp. 6–35, 2013,
- F. Argenti, T. Bianchi, A. Lapini, and L. Alparone, "Fast MAP despeckling based on Laplacian–Gaussian modeling of wavelet coefficients," *IEEE Geoscience and Remote Sensing Letters*, vol. 9, no. 1, pp. 13–17, Jan. 2012.

and also on the following conference papers:

- F. Argenti, T. Bianchi, A. Lapini, and L. Alparone, "Bayesian despeckling of SAR images based on Laplacian–Gaussian modeling of undecimated wavelet coefficients," in *Proc. IEEE Int. Conf. on Acoustics, Speech and Signal Processing (ICASSP)*, 2011, pp. 1445–1448,
- F. Argenti, T. Bianchi, A. Lapini, and L. Alparone, "Simplified MAP despeckling based on Laplacian-Gaussian modeling of undecimated wavelet coefficients," in *Proc. 19th European Signal Processing Conf. (EUSIPCO)*, 2011, pp. 1140–1144.

Chapter 4: Image formats for despeckling

In this chapter, the problem of despeckling SAR images when the input data is either an intensity or an amplitude signal is revisited. Firstly, it is shown that there exists a unique formulation for Bayesian estimators in the undecimated wavelet transform domain; second, the different methods are compared by assessing their performances on both true SAR images and synthetically speckled test images in order to determine the best filtering strategy.

This chapter is mainly based on the following paper:

- T. Bianchi, F. Argenti, A. Lapini, and L. Alparone, "Amplitude vs intensity Bayesian despeckling in the wavelet domain for SAR images," *Digital Signal Processing*, , no. 5, pp. 1353–1362, Sep. 2013,

and also on the following conference paper:

- T. Bianchi, F. Argenti, A. Lapini, and L. Alparone, "Amplitude vs intensity despeckling in the wavelet domain using Bayesian estimators," in *Proc. Tyrrhenian Workshop on Advances in Radar and Remote Sensing*, 2012, pp. 267–274.

Chapter 5: Removal of correlated speckle noise

Despeckling filters are usually designed on the hypothesis of uncorrelated speckle, despite of the transfer function of SAR acquisition systems can introduce a statistical correlation which decreases the despeckling efficiency of such filters. In this chapter, the influence of speckle correlation on the despeckling accuracy of single-look images is addressed. Furthermore, a pre–processing stage, which allows despeckling methods derived for uncorrelated speckle to be successfully applied also for the case of correlated speckle, is proposed.

This chapter is mainly based on the following paper:

- A. Lapini, T. Bianchi, F. Argenti, and L. Alparone, "Blind speckle decorrelation for SAR image despeckling," *IEEE Transactions on Geoscience and Remote Sensing*, vol. 52, no. 2, pp. 1044–1058, 2014,

and also on the following conference papers:

- A. Lapini, T. Bianchi, F. Argenti, and L. Alparone, "Blind whitening of correlated speckle to enforce despeckling of single-look high-resolution SAR images," in *SAR Image Analysis, Modeling, and Techniques XII*, 2012, vol. 8537 of *Proc. of SPIE*, pp. 85370Z–85370Z–8,

- A. Lapini, T. Bianchi, F. Argenti, and L. Alparone, "Blind whitening of correlated speckle to enforce despeckling of single-look high-resolution SAR images," in *Proc. SPIE 8537, Image and Signal Processing for Remote Sensing XVIII*, Nov. 2012, vol. 8537, p. 85370Z.

Chapter 6: Quality assessment of despeckling methods

Quality assessment is a non-trivial task in the remote sensing field because of the lack of the *reference* image. In this chapter, the development and evaluation of a fully automatic method for the quality assessment of despeckled SAR images is proposed.

This chapter is mainly based on the following paper:

- B. Aiazzi, L. Alparone, F. Argenti, S. Baronti, T. Bianchi, and A. Lapini, "An unsupervised method for quality assessment of despeckling: an evaluation on COSMO-SkyMed data," 2011, vol. 8197 of *Proc. of SPIE*, pp. 81790D–81790D–10,

Chapter 7: Conclusions

The last chapter is dedicated to the conclusions about the work carried out during the Ph.D. Course.

Chapter 2

Signal models for despeckling of SAR images

The aim of this chapter is to introduce the most used SAR signal models for incoherent imaging, which are the bases for developing despeckling methods. Under a statistical signal processing perspective, despeckling filters aim at estimating the noise-free radar reflectivity from the observed noisy SAR image [11]. In order to describe the estimation methods that have been developed for the despeckling problem, we need firstly to introduce models for speckle, SAR system and reflectivity separately; such models are mainly related to the description of the several features involving all the acquisition process. In the second part of this chapter, a signal model, which is suitable for incoherent signal processing, is presented.

2.1 Modelling of SAR signal features

2.1.1 Speckle models

SAR is an active acquisition instrument that produces a radiation and captures the signals backscattered from a small area of the imaged scene (*resolution cell*). The received signal, as output from the in-phase and quadrature channels, is complex. If we assume that the resolution cell contains several scatterers and that no one yields a reflected signal much stronger than the others (*distributed target*), then the received signal can be viewed as the incoherent sum of several backscattered waves, i.e., $Ae^{j\phi} = \sum_i A_i e^{j\phi_i}$, as shown in Figure 2.1. The amplitudes A_i and phases ϕ_i are the results of several factors, including propagation attenuation, scattering of the illuminated targets, antenna directivity. Each individual component, however, can

not be resolved within a resolution cell. A first approach to modeling the received signal is solving the Maxwell's equations according to the propagation geometry and scattering medium [12, 13]. By using this approach, the way each propagation path interferes gives us basic information about the observed scene. On the other hand, if we consider that the phases of each path are highly different and that they may sum in a constructive or destructive way, then the amplitude of the received signal varies randomly. So, even if the underlying reflectivity field is uniform, it appears as affected by a "granular" noise after the imaging system. For visual inspection and for specific applications that involve visual information retrieval, such as mapping and segmentation, the highly varying nature of the signal may be considered as a disturbance and is commonly denoted as "speckle".

It should be remarked that speckle is *considered* a noise from the perspective of incoherent imaging, but it is actually a radiometric feature emerging by using a coherent system and it has information content (even if difficult to exploit).

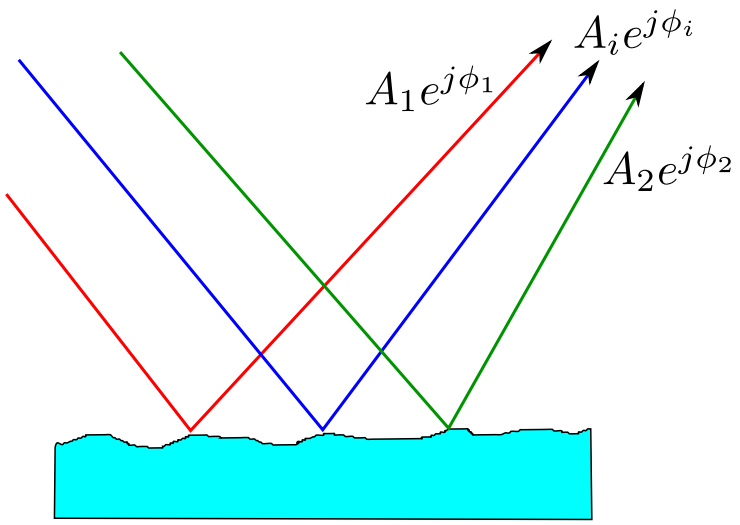

Figure 2.1: *Scattering model explaining fully developed speckle.*

The phases ϕ_i are highly varying (since the wavelength is much shorter than the resolution cell size and scatterers distances) and may be considered as uniformly distributed in $(-\pi, \pi)$ as well as independent of A_i. If the number of scatterers is sufficiently high, the central limit theorem applies [14] and the resulting signal $Ae^{j\phi} = z_1 + jz_2$ can be seen as a complex signal whose real and imaginary parts (in-phase and quadrature components) are independent and identically distributed zero-mean Gaussian variables with variance $\sigma/2$. When this applies speckle is termed as *fully developed* [15].

The joint probability density function (pdf) is given by

$$p_{z_1,z_2}(z_1, z_2) = \frac{1}{\pi\sigma} e^{-\frac{z_1^2+z_2^2}{\sigma}} \tag{2.1}$$

whereas the amplitude A is distributed as a Rayleigh pdf, that is

$$p_A(A) = \frac{2A}{\sigma} e^{-\frac{A^2}{\sigma}} \tag{2.2}$$

and the power or *intensity* $I = A^2$ is distributed according to an exponential pdf, that is

$$p_I(I) = \frac{1}{\sigma} e^{-\frac{I}{\sigma}} \tag{2.3}$$

so that the mean of the intensity is equal to σ. It can be shown [16, 17] that the intensity measurement carries information about the average backscattering coefficient (for distributed targets) related to the resolution cell. Hence, for specific applications, the parameter σ is the actual information we would like to extract from a single channel SAR system. This can be considered as the radar cross section (RCS) of the observed resolution cell. The received signal pdf can be reformulated into

$$p_{I|\sigma}(I|\sigma) = \frac{1}{\sigma} e^{-\frac{I}{\sigma}} \tag{2.4}$$

or

$$I = \sigma u \tag{2.5}$$

where u is exponentially distributed, that is,

$$p_u(u) = e^{-u} \tag{2.6}$$

Eq. (2.5) is termed the *multiplicative model* of speckle.

If only one image (realization of the stochastic process) is available, the best estimate of the scene average reflectivity is just the pixel-by-pixel intensity. This will be a quite noisy estimate because of the previously described constructive/destructive combination effects. From (2.3), it follows that the variance of the intensity in each pixel is σ^2, so that brighter pixel will be affected by stronger disturbances than darker ones. A way to improve the estimation of σ is to average L independent intensity values related to the same position. This processing, named "multilooking", maintains the mean intensity σ but reduces the estimator variance to σ^2/L. Independent "looks" of a target resolution cell can be obtained either by appropriate processing in the Doppler domain (splitting the Doppler bandwidth within the imag-

ing system that compensates the quadratic phase variation created by the platform movement) or by averaging L spatial observations. In both cases, the cost to be paid for estimation accuracy improvement is spatial resolution loss by a factor L. If the hypothesis of independent intensity measurements holds (in the case of correlated data the assumption fails), the L-look averaged intensity I_L is Γ-distributed, that is

$$p_{I_L|\sigma}(I_L|\sigma) = \frac{1}{\Gamma(L)} \left(\frac{L}{\sigma}\right)^L {I_L}^{L-1} e^{-\frac{LI_L}{\sigma}} \tag{2.7}$$

whereas the relative amplitude image $A_L = \sqrt{I_L}$ has a square-root Γ distribution [17]. For visual inspection and for automatic interpretation tasks, the use of amplitude images is preferable, thanks to their reduced dynamic range with respect to intensity images, which is accompanied by an increment in SNR.

The model described above is valid under the assumption that the imaged scene is characterized by distributed scatterers. In the presence of a scatterer much stronger than the others (*point target*), the received signal pdf becomes a Rice distribution and the model above described does not apply. In this case, the received signal power is related to the single target reflection coefficient and, for the purpose of speckle removal, point targets are treated separately from distributed targets.

2.1.2 SAR imaging system model

In the above analysis, the effect of the imaging system has not been taken into consideration. Indeed, the SAR system can achieve a spatial resolution of the order of the antenna size only if proper processing, referred to as *focusing*, is applied. The energy of the transmitted frequency modulated (FM) chirp pulse is spread into the range-Doppler domain and such a processing consists of matched filtering along the range and along iso-Doppler curves and is needed to compact energy back in the spatial domain [16]. From this point of view, a SAR system can be seen as an encoding transfer function $h_e(\mathbf{r})$ followed by a compression transfer function $h_c(\mathbf{r})$ [17, 18]. If $\sigma_c(\mathbf{r})$ denotes the complex reflectivity, the observed single–look complex (SLC) signal after the imaging processor is

$$g_c(\mathbf{r}) = [C \cdot \sigma_c(\mathbf{r}) * h_e(\mathbf{r}) + n(\mathbf{r})] * h_c(\mathbf{r}) \tag{2.8}$$

where the constant C absorbs propagation information (e.g., loss and antenna gains) and the term $n(\mathbf{r})$ accounts for thermal noise at the receiver. For

sufficiently high signal-to-noise ratios, the noise term can be neglected and the received complex signal becomes

$$g_c(\mathbf{r}) = C \cdot \sigma_c(\mathbf{r}) * h_e(\mathbf{r}) * h_c(\mathbf{r}) = C \cdot \sigma_c(\mathbf{r}) * h(\mathbf{r}) \tag{2.9}$$

For well-designed SAR, the impulse response $h(\mathbf{r})$ is pulse-like and represents the point spread function (PSF) of the system that, in a first approximation, can be assumed as independent of the position. Again, the intensity $|g_c(\mathbf{r})|^2$ is proportional to the average backscattering coefficient of the cell and is the information we would like to achieve from the observation. An accurate description of the model in (2.9) and of the statistical properties of the acquired SAR image is given in [18].

2.1.3 Reflectivity models

The speckle formation model yields a pixel-wise description of the observed signal. For many applications, including despeckling, more refined models are needed. Such models describe the observed received signal at a coarser scale than the single pixel one and try to intercept information about the underlying texture of the imaged scene and its correlation. It is then crucial to consider also the average intensity, i.e., RCS σ, which is considered the information to be retrieved, as a random process. Unfortunately, the RCS is not directly observable and its properties must be inferred from the intensity values over an area in which the texture is homogeneous. In this sense, RCS modeling can be seen as an inverse problem whose solution is made difficult by the fact that homogeneity can be stated only if a ground truth is available, but often this is not the case. Furthermore, since the problem can be formulated only in a statistical sense, the dimension of the homogeneous area becomes crucial: it should be as large as possible in order to reliably apply statistical hypothesis testing methods, but this contrasts with the natural scenes structure that is often characterized by the presence of limited size homogeneous areas (such as fields, woods, orchards, forests, trees, man-made areas) and mixing the information of different textures makes the hypothesis tests to fail.

The starting point for solving this inverse problem is the statistics of the observed intensity over a homogeneous area. The pdf of the intensity signal can be written as

$$p(I) = \int p(I|\sigma)p(\sigma)d\sigma \tag{2.10}$$

where $p(I|\sigma)$ is the single pixel speckle model, given by (2.4) and (2.7) for the 1-look and L-look cases, respectively. Eq. (2.10) is referred to as the *product*

model of the observed intensity [11]. One of the assumptions that must be made to state the validity of the model (2.10) is that the RCS fluctuation scale is larger than that of speckle.

Even though several pdfs have been proposed for the intensity I (e.g., Weibull, log–normal), one of the most used pdf is the K distribution. The K distribution is a parametric pdf that, with a suitable choice of its parameters, well fits observed intensity histograms. It has also the advantage that a closed form of the RCS pdf, i.e., $p(\sigma)$, exists such that the product model in (2.10) yields a K distribution. In fact, if the RCS pdf is a Γ distribution, that is

$$p(\sigma) = \left(\frac{\nu}{\bar{\sigma}}\right)^{\nu} \frac{\sigma^{\nu-1}}{\Gamma(\nu)} e^{-\frac{\nu\sigma}{\bar{\sigma}}} \tag{2.11}$$

where ν is an *order* parameter and $\bar{\sigma}$ is the mean, then the pdf of the observed intensity signal is given by

$$p(I) = \frac{2}{\Gamma(L)\Gamma(\nu)} \left(\frac{L\nu}{\bar{I}}\right)^{\frac{L+\nu}{2}} I^{\frac{L+\nu-2}{2}} K_{\nu-L}\left(2\sqrt{\frac{\nu L I}{\bar{I}}}\right) \tag{2.12}$$

where $K_n(\cdot)$ is the modified Bessel function of order n and $\bar{I}$ is the mean of intensity. Fitting the parameters of the pdf to the observed signal allows information on the RCS to be retrieved.

The model in (2.12) yields a pixel-wise statistical description of the observed intensity values. A complete description of the scene, however, needs the inclusion of the autocorrelation function into the model. If such a function is estimated from the observed data, then the exact autocorrelation function of the RCS is quite difficult to achieve and usually it does not exist in a closed form [17].

2.2 Modelling of noisy SAR signal

From the previous discussion, it emerges that modeling the received SAR signal should take into account several physical, statistical and engineering aspects of the overall system. Such a complexity makes the process of extracting average backscatter information from the observed signal a non-trivial task. From a signal processing perspective, a first step towards finding efficient solutions is stating the acquisition model in the simplest form as possible. In [11], several multiplicative models of speckle are described and classified according to the autocorrelations of the imaged scene and of the noise term.

Perhaps, the most used model in the literature on despeckling is the following:

$$g = fu \tag{2.13}$$

where f is a possibly autocorrelated random process and represents the noise–free reflectivity; u is a possibly autocorrelated stationary random process, independent of f, and represents the speckle fading term; g is the observed noisy image. All the quantities in (2.13) may refer to either intensity or amplitude as well as to single-look or multilook images, whose pdfs have been described previously.

The variable u may be assumed as spatially correlated [19]. Recently, it has been shown [20] that a preprocessing step that makes speckle uncorrelated, that is "whitens" the complex signal, allows despeckling algorithms designed for uncorrelated speckle to be successfully applied also when speckle is (auto)correlated. Therefore, in the following we shall analyze only algorithms working under the hypothesis of uncorrelated speckle.

The nonlinear nature of the relationship between observed and noise-free signals makes the filtering procedure a non-trivial task. For this reason, some manipulations have been introduced to make the observation model simpler. Several authors adopt the following model, derived from (2.13):

$$g = f + (u-1)f = f + v, \tag{2.14}$$

where $v = (u-1)f$ accounts for speckle disturbance in an equivalent additive model, in which v, depending on f, is a *signal-dependent* noise process.

A second way that allows the multiplicative noise to be transformed into an additive one is using a *homomorphic* transformation [21]. It consists of taking the logarithm of the observed data, so that we have

$$\begin{aligned} \log g &= \log f + \log u \\ g' &= f' + u' \end{aligned} \tag{2.15}$$

where g', f' and u' denote the logarithm of the quantities in (2.13). Unlike the case in (2.14), here the noise component u' is a *signal-independent* additive noise. However, this operation may introduce a bias into the denoised image, since an unbiased estimation in the log-domain is mapped onto a biased estimation in the spatial domain [22]; in math form, if u exhibits $E[u] = 1$, $E[u'] = E[\log(u)] \neq \log(E[u]) = \log(1) = 0$.

The relations in (2.14) or in (2.15) express two formulations of the problem in the spatial domain; a despeckling method which estimates f (f') by directly processing g (g') is said to be a *space domain* filter.

Over the last two decades, approaches to image denoising that perform

estimation in a *transformed domain* have been proposed. Transforms derived from multiresolution signal analysis [23, 24], such as the discrete wavelet transform (DWT), are the most popular in this context. Despeckling method adopting a multiresolution framework is usually referred to *multiresolution* filter or *scale-space* filter. Despeckling in a transformed domain is carried out by taking the direct transform of the observed signal (g or g' in such case), by estimating the speckle-free coefficients and by reconstructing the filtered image through the inverse transform applied to the despeckled coefficients. A more in-depth analysis is given in 2 3.

Figure 2.2 summarizes the despeckling process on various versions of the additive models. The block "Estimator" attempts to achieve a speckle-free representation of the signal in a specific domain; for example, in the transform domain, as in Figure 2.2-(c), or in the homomorphic-transform domain, as in Figure 2.2-(d), in which the noise-free informative signal is contaminated with additive signal-dependent or signal-independent noise, respectively.

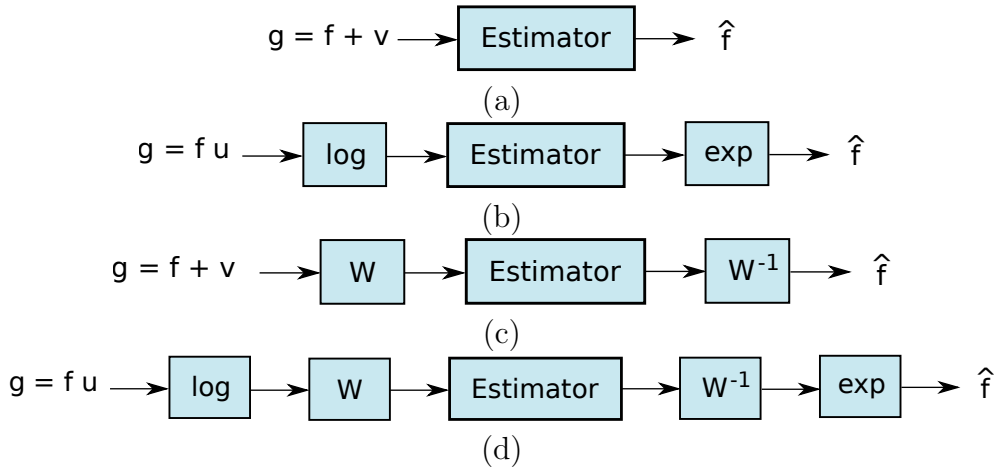

Figure 2.2: *Additive models commonly used in despeckling algorithms: (a) signal-dependent in spatial domain; (b) signal-independent in spatial domain; (c) signal-dependent in transform domain; (d) signal-independent in transform domain.*

Chapter 3

Bayesian methods in the wavelet domain

The aim of this chapter is to present the framework of despeckling based on the Bayesian estimation in the undecimated wavelet transform (UDWT) domain. The fundamental of Bayesian estimation and the wavelet transform are firstly recalled, and emphasis to the problem of probability density function (pdf) is given. In the second part, a review of some methods proposed in the literature is discussed. Finally, a fast MAP despeckling filter which reach state-of-art performances is presented.

3.1 Preliminary concepts

3.1.1 Bayesian estimation

From the discussion in Section 2.2 about the most widely used signal models for despeckling, it can be seen that the multiplicative model is often manipulated in order to obtain an additive one. The basics of Bayesian estimation are now reviewed for the simplest case, shown in Figure 2.2-(a), even though analogous derivations hold for all the other cases in Figure 2.2. Since the following analysis can be generalised to quantities which belong to any domain, the symbols θ, r and x will be used. The relationship between such quantities is given by the model of additive signal-dependent noise:

$$x = \theta + r \tag{3.1}$$

A Bayesian estimator [25] tries to achieve an estimate $\hat{\theta}$ of θ - which is assumed to be a random process - by having some prior information about the signal to be estimated, summarized in $p_\Theta(\theta)$, the a-priori pdf of θ. Given

t$p_\Theta(\theta)$ and the pdf of noise process $p_R(r)$, the *a posteriori* probability density function of the noise-free reflectivity conditional to the observed signal, that is $p_{\Theta|X}(\theta|x)$, can be achieved. Specifically, from the Bayes' rule it follows

$$\begin{aligned} p_{\Theta|X}(\theta|x) &= \frac{p_{X|\Theta}(x|\theta)p_\Theta(\theta)}{p_X(x)} \\ &= \frac{p_{R|\Theta}(x-\theta|\theta)p_\Theta(\theta)}{\int p_{R|\Theta}(x-\theta|\theta)p_\Theta(\theta)\ d\theta}. \end{aligned} \tag{3.2}$$

Different Bayesian estimators can be defined according to the choice of the Bayesian "risk", i.e., the function of the estimation error $\varepsilon = \theta - \hat{\theta}$ to be minimized.

The maximum a-posteriori probability (MAP) estimator minimizes the quantity $E[C(\varepsilon)]$, where $C(\varepsilon) = 1$ for $|\varepsilon| > \delta$ and $C(\varepsilon) = 0$ elsewhere. It is well-known [25] that the solution , when δ is small, is given by

$$\hat{\theta}^{\mathrm{MAP}} = \arg\max_\theta p_{\Theta|X}[\theta|x]. \tag{3.3}$$

By exploiting the Bayes rule and the additive model, it yields

$$\begin{aligned} \hat{\theta}^{\mathrm{MAP}} &= \arg\max_\theta\ p_{X|\Theta}(x|\theta)p_\Theta(\theta) \\ &= \arg\max_\theta\ p_R(x-\theta)p_\Theta(\theta) \end{aligned} \tag{3.4}$$

or, equivalently,

$$\hat{\theta}^{\mathrm{MAP}} = \arg\max_\theta\ [\log p_R(x-\theta) + \log p_\Theta(\theta)]. \tag{3.5}$$

The minimum mean square error (MMSE) estimator minimizes the quantity $E[\varepsilon^2] = E[(\theta - \hat{\theta})^2]$. The solution is given by

$$\hat{\theta}^{\mathrm{MMSE}} = E_{\Theta|X}[\theta|x] \tag{3.6}$$

which is the expectation of the noise-free signal conditional to the noisy

observation. Again, by exploiting the Bayes rule and using (3.1), it follows

$$\begin{aligned}\hat{\theta}^{\mathrm{MMSE}} &= \int \theta p_{\Theta|X}(\theta|x)d\theta \\ &= \int \theta \frac{p_{X|\Theta}(x|\theta)p_{\Theta}(\theta)}{p_X(x)}d\theta \\ &= \frac{\int \theta p_R(x-\theta)p_{\Theta}(\theta)d\theta}{\int p_R(x-\theta)p_{\Theta}(\theta)d\theta}\end{aligned} \tag{3.7}$$

The estimate in (3.7) would require the knowledge of the nonstationary joint pdfs of any orders.

A simpler solution requiring only second order moments is the linear MMSE (LMMSE) estimator, in which the MMSE solution is sought by constraining the estimator to be a linear combination of the observed variables. The LMMSE estimator is given by

$$\hat{\theta}^{\mathrm{LMMSE}} = E[\theta] + C_{\theta x}C_{xx}^{-1}(x - E[x]), \tag{3.8}$$

in which $C_{\theta x}$ is the covariance matrix between θ and x and C_{xx} is the autocovariance matrix of x. Prior knowledge is now embedded in the second order statistics of the noise-free and noisy signals, which can be derived by exploiting the additive model.

Finally, the absolute error function $C(\varepsilon) = |\varepsilon|$ yields the minimum mean absolute error (MMAE) estimator, corresponding to the median of the posterior pdf $p_{\Theta|X}(\theta|x)$, that is

$$\begin{aligned}\frac{1}{2} &= \int_{-\infty}^{\hat{\theta}^{\mathrm{MMAE}}} p_{\Theta|X}(\theta|x)\,d\theta \\ &= \frac{\int_{-\infty}^{\hat{\theta}^{\mathrm{MMAE}}} p_{X|\Theta}(x|\theta)p_{\Theta}(\theta)\,d\theta}{\int_{-\infty}^{+\infty} p_{X|\Theta}(x|\theta)p_{\Theta}(\theta)\,d\theta} \\ &= \frac{\int_{-\infty}^{\hat{\theta}^{\mathrm{MMAE}}} p_R(x-\theta|\theta)p_{\Theta}(\theta)\,d\theta}{\int_{-\infty}^{+\infty} p_R(x-\theta|\theta)p_{\Theta}(\theta)\,d\theta}\,.\end{aligned} \tag{3.9}$$

Eqs. (3.7), (3.8), (3.4) and (3.9) reveal that all solutions, besides to the a-priori information on θ, require also knowledge of the pdf of the noise component r.

3.1.2 Wavelet transforms

A Bayesian estimation carried out in the spatial domain leads to a solution that adaptively depends on local statistics, i.e., is a space-adaptive estimator. A Bayesian estimation carried out in the multiresolution, or *scale-space*, domain may have the extra value of leading to a scale-space adaptive estimator, that is, an estimator adaptive not only in space but also in scale. Such an extra value is not automatic and requires careful pdf modeling in the transformed domain, otherwise the spatial adaptivity may get lost in favor of the scale adaptivity.

The wavelet analysis provides a multiresolution representation of continuous and discrete-time signals and images [24]. For discrete-time signals, the classical maximally decimated wavelet decomposition is implemented by filtering the input signal with a lowpass filter $H_0(z)$ and a highpass filter $H_1(z)$ and downsampling each output by a factor two. The synthesis of the signal is obtained with a scheme symmetrical to that of the analysis stage, i.e., by upsampling the coefficients of the decomposition and by lowpass and highpass filtering. Analysis and synthesis filters are designed in order to obtain the perfect reconstruction of the signal and by using different constraints (e.g., orthogonal or biorthogonal decomposition, linear phase filters). Applying the same decomposition to the lowpass channel output yields a two-level wavelet transform: such a scheme can be iterated in a dyadic fashion to generate a multilevel decomposition. The analysis and synthesis stages of a two-level decomposition are depicted in Figure 3.1-(a).

In several image processing applications, e.g., compression, the DWT is particularly appealing since it compacts energy in few coefficients. However, for most of the tasks concerning images, the use of an undecimated discrete wavelet transform (UDWT) is more appropriate thanks to the shift-invariance property. UDWT is also referred to as *stationary* WT (SWT) [26, 27], as opposite to Mallat's octave (dyadic) wavelet decomposition DWT [24], which is maximally, or *critically*, decimated. The rationale for working in the UDWT domain is that in DWT, when coefficients are changed, e.g., thresholded or shrunk, the *constructive* aliasing terms between two adjacent subbands are no longer canceled during the synthesis stage, thereby resulting in the onset of structured artifacts [28].

As to the construction of the UDWT, it can be shown that omitting the downsamplers from the analysis stage and the upsamplers from the synthesis stage, then the perfect reconstruction property can still be achieved. The relative scheme for a two-level decomposition is depicted in Figure 3.1-(b). In the block diagram, by applying the *noble identities* [29], the downsamplers (upsamplers) have been shifted towards the output (input) of the analysis

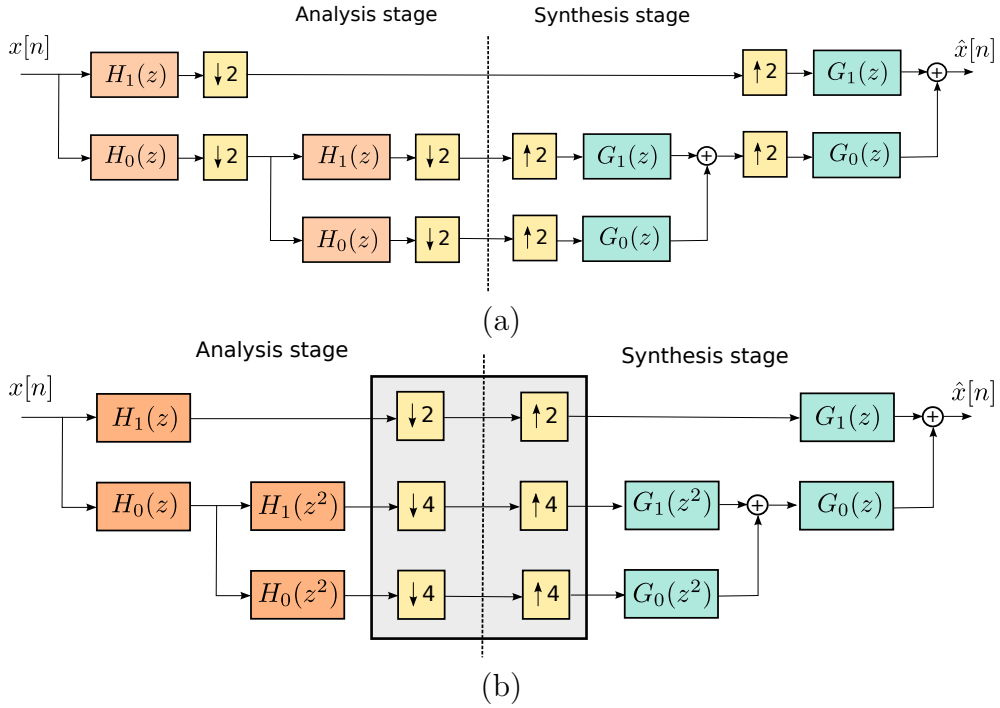

Figure 3.1: *Two-level non redundant wavelet decomposition / reconstruction (a) and the equivalent scheme obtained applying the noble identities (b). The undecimated wavelet transform is obtained by eliminating the downsamplers and upsamplers contained in the shaded box.*

(synthesis) stage. Eliminating these elements yields the UDWT. As a consequence, the coefficients in the transform domain can be obtained by filtering the original signal by means of the following *equivalent* transfer functions:

$$\begin{aligned} H^j_{eq,l}(z) &= \prod_{m=0}^{j-1} H_0(z^{2^m}), \\ H^j_{eq,h}(z) &= \left[\prod_{m=0}^{j-2} H_0(z^{2^m})\right] \cdot H_1(z^{2^{j-1}}) \end{aligned} \tag{3.10}$$

where the subscripts l and h refer to the *approximation* (lowpass) and *detail* or *wavelet* (bandpass and highpass) signals, whereas j denotes the level of the decomposition. An example of the equivalent filters frequency responses, relative to a four-level decomposition, is shown in Figure 3.2.

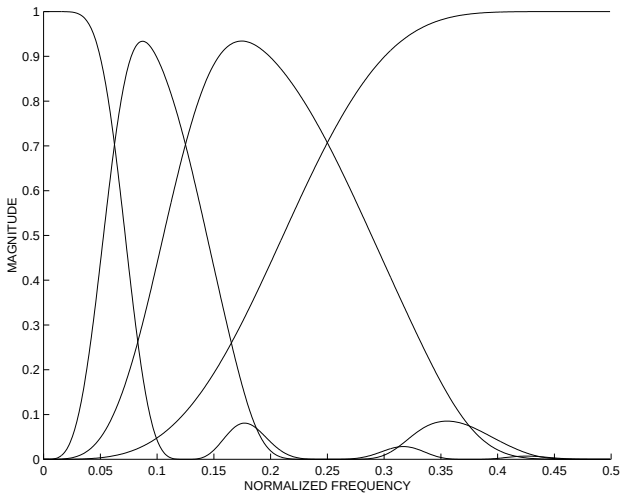

Figure 3.2: *Equivalent filters frequency responses obtained from 8-tap Daubechies orthogonal wavelets [23].*

Let $A^j_x(n)$ and $W^j_x(n)$ denote the approximation and wavelet coefficients, respectively, of the signal x at the jth level of the decomposition, whereas n is the spatial index. Since the wavelet transform is linear, from equation (2.14), it follows

$$A^j_g(n) = A^j_f(n) + A^j_v(n) \tag{3.11}$$

$$W^j_g(n) = W^j_f(n) + W^j_v(n) \tag{3.12}$$

Usually, only the wavelet coefficients (3.12) are processed for despeckling; the baseband approximation is left unchanged.

The wavelet transform is usually implemented for images by using separable filtering along the columns and the rows of the image. The effect of this processing is the extraction, in each subband, of a rectangular region of the frequency plane which corresponds, in the spatial domain, to the extraction of horizontal and vertical details with different degrees of resolution. The frequency plane splitting relative to a single level decomposition is given in Figure 3.3-(a). However, extracting directional information has been demonstrated to be useful in several image processing tasks.

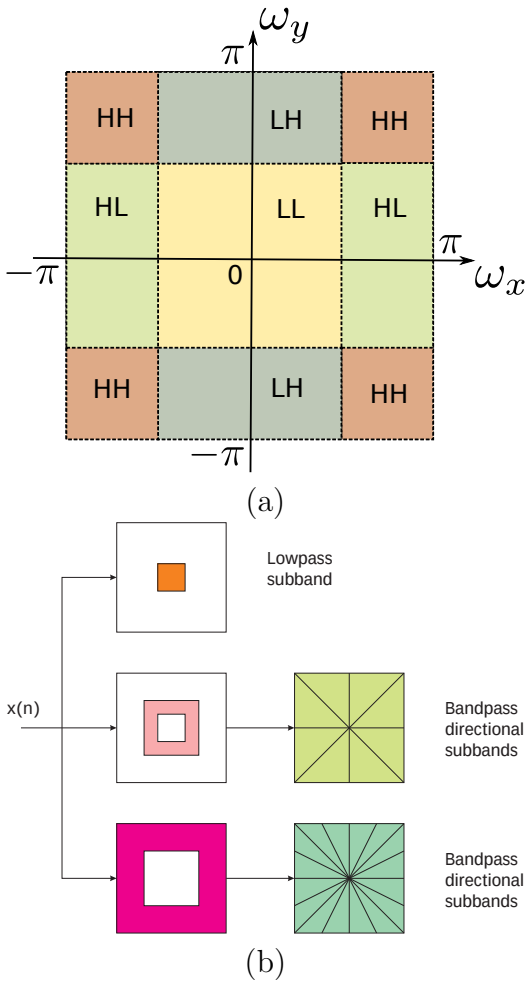

Figure 3.3: *Frequency splitting from a single-level separable DWT (a), obtained by lowpass (L) and highpass (H) filtering along the rows and the columns (LL, HL, LH, and HH denote all possible combination); in (b), the splitting obtained from the nonsubsampled Laplacian pyramid decomposition (on the left) and the nonsubsampled directional filter banks (on the right) composing the contourlet transform.*

Recently, multiresolution transforms embedding directional information, such as contourlets [30], curvelets [31, 32], and many others, have been successfully applied to denoising in general and despeckling in particular. The nonsubsampled contourlet transform is a combination of a nonsubsampled Laplacian pyramid (NLP) decomposition and of nonsubsampled directional filter banks (NDFB). The relative frequency splitting is depicted in Figure 3.3-(b). As in the case of the UDWT, also the coefficients of the nonsubsampled contourlet transform can be achieved by means of linear time-invariant (LTI) systems directly applied to the input, which allows statistical parameters to be easily computed. Using directional information is effective in terms of despeckling performance [33], even though a higher computational cost must be paid due to the need of a nonseparable implementation.

By assuming that the transform is linear, the additive models in (2.14) and (2.15) can be easily generalized to a generic transformed domain. Specifically, for the formulation given in (2.14), if W_x denotes the transform operator applied to the signal x, it follows

$$W_g = W_f + W_v, \tag{3.13}$$

In an analogous way, by applying both the homomorphic filtering concept and the linear transform, the observation model in (2.15) becomes

$$W_{g'} = W_{f'} + W_{u'}. \tag{3.14}$$

The Bayesian estimator explicitly derived for the additive model in (2.14), can also be applied to the additive models defined in (2.15), (3.13), and (3.14) by simply changing the type of variables and prior knowledge, that is: 1) the prior pdf of the signal of interest (related to the reflectivity) and represented by f, f', W_f and $W_{f'}$ in equations (2.14), (2.15), (3.13), and (3.14), in that order; 2) the pdf of the additive noise component, represented by v, u', W_v and $W_{u'}$, in the same equations.

In the following dissertation will uniquely focus in the UDWT domain, hence it will be assumed the symbols appearing in (3.13) have the same meaning of the corresponding ones in (3.12); for sake of simplified notation, whenever the reasoning refer to a generic subband, the subband index j will be dropped.

3.1.3 Pdf modeling

Bayesian estimation relies on an accurate probabilistic modeling of the signals under concern. However, the choice of pdfs suitable for modeling the

data of interest is not a simple task. In Section 2.2, some of the most used pdfs for the speckle and reflectivity processes have been described. While the former derive from the image formation mechanism and may be considered as valid in most of the images where the fully developed speckle model holds, the latter highly depend on the imaged scene. It should be noted again that different types of landscapes and land covers induce different distributions on the reflectivity signal. Models of the underlying land cover may help to derive a pdf of the imaged signal, but this knowledge may not be available for despeckling or may be insufficient. As to the modeling of signals in the homomorphic domain, an exact derivation of the log-intensity and of the log-amplitude of the fading variable is available [22], whereas the characterization of the backscattering coefficient still remains crucial.

The modeling of the involved variables may be simpler and more robust if one works in a multiresolution, or *scale-space*, domain, instead than in the spatial domain. In fact, it is well-known that the pdf of wavelet coefficients can be approximated by several unimodal distributions - as noticed by Mallat in his seminal paper [24], where a generalized Gaussian was used - that can be described by a small number of parameters. They can be adaptively estimated from the coefficients of the observed image, independently of the distribution of the image that is transformed.

Validating a hypothetical pdf model is, in general, quite hard. In some works, wavelet coefficients pdfs are validated "globally" from the observation of the histogram of the amplitude of the coefficients in a whole subband. However, since the signal is nonstationary, spatially adaptive methods should be used instead. A single observation, or realization, of the scene is usually available; thus, one may only conjecture that wavelet coefficients "locally" follow a given distribution (only few samples are available to perform the validation of the local model) whose parameters locally vary. A way to check the validity of the pdf model is experimentally observing the performances of despeckling filters on either true SAR or synthetically speckled images. As a general rule of thumb, the higher the number of parameters, or degrees of freedom, of the pdf, the better its ability to model the true wavelet coefficients pdf within a whole subband, but the lower their estimation accuracy from the few samples available in a local window within a subband and the higher the complexity of the resulting estimator. Therefore, the use of reasonably simple distributions may be expected to yield better results than more complex ones, that is, *overfitting* is not rewarding.

Another fact that should be considered when a pdf model is chosen is the computational cost. Some combinations of estimation criterion and pdf model yield a Bayesian estimator that can be achieved only numerically [34]. This fact may prevent from using the filter when huge amounts of data need

to be processed. In this case, a closed form solution may be preferred, even though a possible loss of performances may be experienced.

In order to find the explicit expressions of the estimators defined in Section 3.1.1, a model for the pdfs of the wavelet coefficients relative to the original reflectivity and to the additive signal–dependent noise is needed. In the following, different pdf models are proposed. The different models will be denoted by two acronyms (or labels) referring to the statistical distribution of the coefficients of the signal W_f and of the noise W_v. The proposed pdfs represent a trade-off between simplicity (few parameters to be estimated from the observed data) and modelling capability.

G–G model A classical pdf modelling used for this purpose is the zero-mean Gaussian (G) distribution [35], which depends only on the variance σ^2 and is symmetric around zero,

$$p_X(x) = \frac{1}{\sqrt{2\pi}\sigma} \exp\left(-\frac{x^2}{2\sigma^2}\right). \tag{3.15}$$

This is a quite simple and particular case, because it is know that the posterior pdf of a G-G model is a Gaussian distribution. Hence, the three considered Bayesian estimators yield the same expression.

GG–GG model Since the birth of the wavelet recursive algorithm by Mallat [24], a generalized Gaussian (GG) pdf has been used to model image wavelet coefficients and several other authors use the GG distribution for many image processing tasks involving wavelets. A zero-mean GG pdf depends only on two parameters and is characterized by being symmetric around the mean. Its expression is given by

$$p_X(x) = \left[\frac{\nu \cdot \eta(\nu,\sigma)}{2 \cdot \Gamma(1/\nu)}\right] \exp\left\{[\eta(\nu,\sigma) \cdot |x|]^{\nu}]\right\}, \tag{3.16}$$

where Γ is the Gamma function, σ is the standard deviation of the distribution, ν is a *shape factor*, and $\eta(\nu,\sigma)$ is given by

$$\eta(\nu,\sigma) = \frac{1}{\sigma}\left[\frac{\Gamma(3/\nu)}{\Gamma(1/\nu)}\right]^{1/2}. \tag{3.17}$$

The GG distribution is still reasonably simple, since the use of only two parameters allows different levels of "peakedness" to be achieved. As particular cases, the GG pdf includes both the Laplacian and the Gaussian pdfs, for

$\nu = 1$ and $\nu = 2$, respectively. A plot of GG pdf curves for different values of ν is shown in Figure 3.4

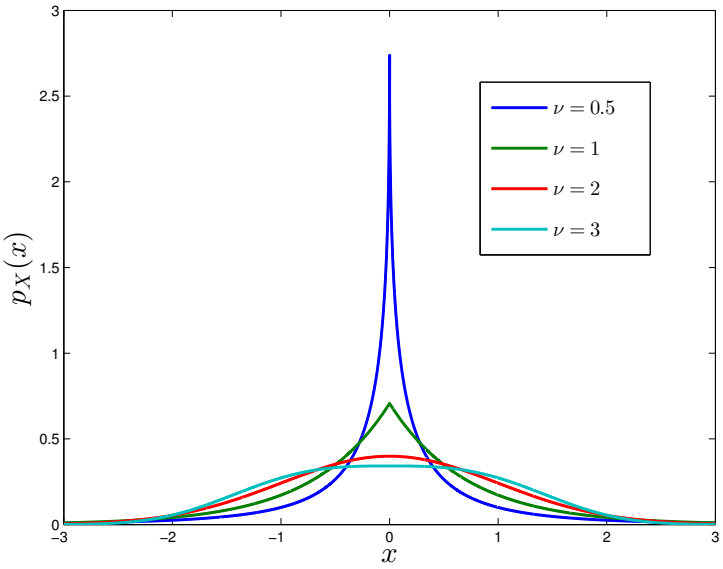

Figure 3.4: *Zero-mean GG pdfs obtained with unity variance and different νs.*

In [36], a method for the estimation of the parameters relative to the GG model, i.e., the standard deviation σ and the shape factor ν of the distributions relative to W_f W_v, is given. The estimation of the parameters is based on the computation of some moments of the observable variables g and W_g.

L–G model Some experimental observations of the shape parameters suggest us that the GG assumption for the distributions of the wavelet coefficients can be simplified. As to the pdfs of the wavelet coefficients of the speckle-free signal, i.e., p_{W_F}, an example of the histogram of the estimated shape parameters, obtained from the test image *Lena* degraded with 4-look synthetic speckle, is shown in Figure 3.5-(a): as can be seen, it may be assumed that they roughly approach the value 1. An analogous example, relative to the pdfs of the wavelet coefficients of the signal-dependent noise, i.e., $p_{W_G|W_F} = p_{W_V}(W_g - W_f)$, is shown in Figure 3.5-(b): in this case, it may be assumed the shape parameters approach the value 2. A similar behaviour has been also encountered for different subbands and different decomposition levels. Hence, the simplest combination of Laplacian and Gaussian pdfs gives the L–G model. Specifically, it assumes that the wavelet coefficients of the noise–free reflectivity follow a zero–mean Laplacian distribution, whose pdf

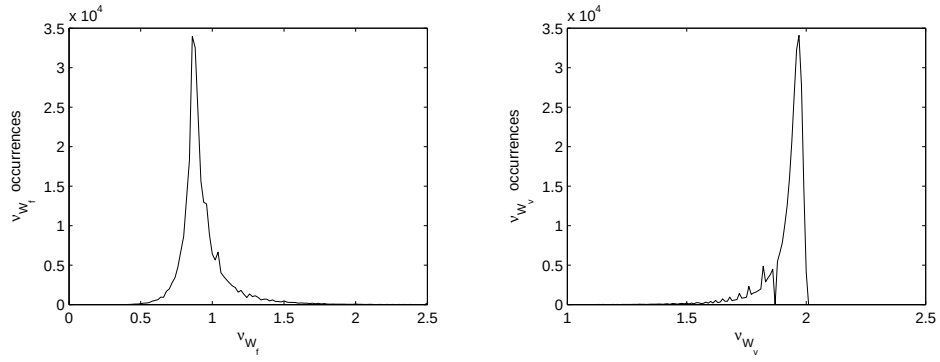

(a) (b)

Figure 3.5: *Examples of the histogram of the estimated shape parameters: (a) wavelet coefficients of the speckle-free signal; (b) wavelet coefficients of the signal-dependent noise.*

is given by

$$p_X(x) = \frac{1}{\sqrt{2}\sigma} \exp\left(-\frac{\sqrt{2}|x|}{\sigma}\right). \tag{3.18}$$

As it can be seen, it depends only on a single parameter, the variance σ^2. In the L–G model, the coefficients of the signal–dependent noise are supposed to be distributed as a Gaussian.

MIX–G model An alternative model based on Gaussian and Laplacian pdfs is the MIX–G model, in which the wavelet coefficients of the noise–free reflectivity are supposed follow a mixture of zero–mean Laplacian and Gaussian kernels, having both the same variance σ^2. Such a pdf is expressed by:

$$p_X(x) = \alpha \frac{1}{\sqrt{2}\sigma} \exp\left(-\frac{\sqrt{2}|x|}{\sigma}\right) + (1-\alpha)\frac{1}{\sqrt{2\pi}\sigma} \exp\left(-\frac{x^2}{2\sigma^2}\right), \tag{3.19}$$

where α is the mixture coefficient ($0 \leq \alpha \leq 1$). As it can be seen, this distribution is characterized by two parameters. Concerning the estimation of the mixture coefficient α appearing in (3.19), it can be easily shown that this can be computed as

$$\alpha = \frac{E[W_f^4]}{3\sigma_{W_f}^4} - 1. \tag{3.20}$$

Both $E[W_f^4]$ and $\sigma_{W_f}^2$ can be obtained by using the method in [36], where the statistical moments are replaced by the empirical averages. Also in this

model, the coefficients of the signal–dependent noise are supposed to follow a Gaussian distribution.

3.2 Despeckling filters in the UDWT domain

In this section, some Bayesian despeckling filters in the undecimated wavelet domain that use a multiresolution analysis are proposed and discussed. The methods refer to the additive model in (3.13), that is, they do not exploit the homomorphic transform, which may introduce bias in the estimation of the despeckled image. A performance gain in the removal of speckle can be achieved by considering strategies that deal with the SAR image heterogeneity, as it is explained in the last part of the section.

Figure 3.6 outlines the flowchart of a generic Bayesian despeckling filter in the UDWT domain. As it appears, the majority of processing is carried

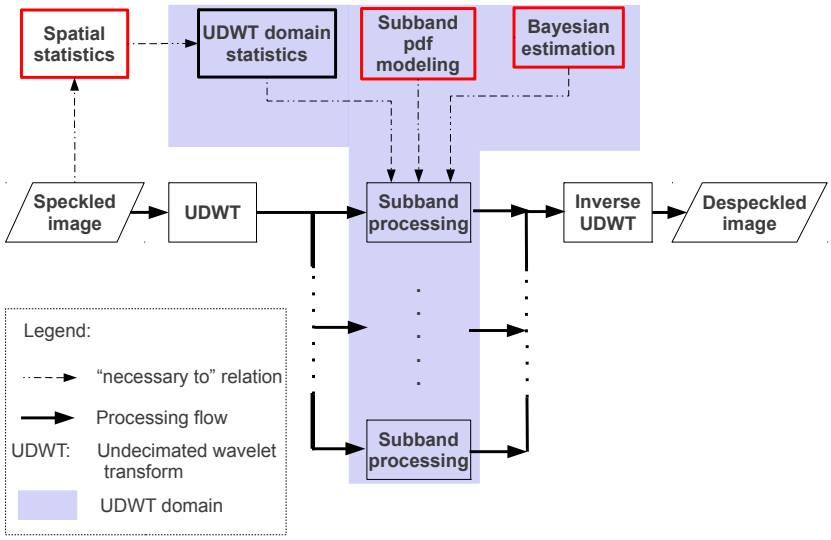

Figure 3.6: *Flowchart of Bayesian filtering in the undecimated wavelet domain.*

out in the transform domain. Statistics in the transform domain are directly calculated from the spatial statistics of the image by exploiting the equivalent filters (3.2), as firstly proposed by Foucher *et al.* [37]. By substituting the pdfs of a specific model into (3.2) and selecting the Bayesian functional to be minimized, the mathematical expression of a Bayesian estimator can be obtained. The results obtained solving (3.4), (3.7), and (3.9) are presented

model–by–model below, explicating that the estimation is performed in the UDWT domain. Thus, in the following, the symbols θ, r and x are replaced by W_f, W_v and W_g, respectively, such that the relationships (3.1) and (3.13) are equivalent. A common assumption for all the proposed solutions is that W_f are W_v statistically independent.

Some of the results presented in this section have been derived elsewhere in the literature. Several estimators, instead, are an original contribution of the presented study. A complete mapping of estimators for several Bayesian criteria and for several different pdfs will allow to derive insights about the influence of the choice of either the estimation type or the pdf modelling on the overall performances.

For sake of simplicity, the following expressions are defined:

$$\rho \stackrel{\text{def}}{=} \sqrt{2}\frac{\sigma_{W_v}^2}{\sigma_{W_f}}. \tag{3.21}$$

$$\varphi \stackrel{\text{def}}{=} \frac{\sqrt{2}W_g}{\sigma_{W_f}}, \tag{3.22}$$

$$\psi \stackrel{\text{def}}{=} \frac{\sigma_{W_v}}{\sigma_{W_f}}, \tag{3.23}$$

$$\operatorname{erfc}(x) \stackrel{\text{def}}{=} \frac{2}{\sqrt{\pi}} \int_x^{+\infty} e^{-t^2}\, dt, \tag{3.24}$$

$$\mathrm{A} \stackrel{\text{def}}{=} \exp(-\varphi) \operatorname{erfc}\left(\psi - \frac{\varphi}{2\psi}\right), \tag{3.25}$$

$$\mathrm{B} \stackrel{\text{def}}{=} \exp(\varphi) \operatorname{erfc}\left(\psi + \frac{\varphi}{2\psi}\right), \tag{3.26}$$

$$\mathrm{C} \stackrel{\text{def}}{=} \frac{1}{\sqrt{2\pi\left(\sigma_{W_f}^2 + \sigma_{W_v}^2\right)}} \exp\left[-\frac{{W_g}^2}{2\left(\sigma_{W_f}^2 + \sigma_{W_v}^2\right)}\right], \tag{3.27}$$

$$\mathrm{D} \stackrel{\text{def}}{=} \frac{W_g}{1+\psi^2}, \tag{3.28}$$

$$\mathrm{F}(x) \stackrel{\text{def}}{=} \begin{cases} e^{\varphi}\operatorname{erfc}\left(\psi + \frac{W_g - x}{\sqrt{2}\sigma_{W_v}}\right), & \text{if } x \leq 0 \\ \mathrm{A} + \mathrm{B} - e^{-\varphi}\operatorname{erfc}\left(\psi - \frac{W_g - x}{\sqrt{2}\sigma_{W_v}}\right), & \text{if } x > 0\,. \end{cases} \tag{3.29}$$

3.2.1 G–G model

Due to the particular features of the Gaussian distribution, the expression of the three estimators coincide in the LMMSE estimator (3.8) [35]:

$$\hat{W}_f^{\mathrm{LMMSE}} = W_g \cdot \frac{\sigma_{W_f}^2}{\sigma_{W_f}^2 + \sigma_{W_v}^2}, \tag{3.30}$$

where $\sigma_{W_f}^2$ and $\sigma_{W_v}^2$ are the variance of the noise-free and noise wavelet coefficients, respectively. Hence (3.30) has a simple and closed analytical form.

3.2.2 GG–GG model

No estimator of this model is known in a closed analytical form. Mode, mean and median of the posterior pdf have to be found numerically.

MAP estimator

The solution [36] is given by

$$\begin{aligned}\hat{W}_f^{\mathrm{MAP}} &= \arg\max_{W_f} \left[\ln \frac{\eta_{W_f} \nu_{W_f}}{2\Gamma(1/\nu_{W_f})} - \left(\eta_{W_f}|W_f|\right)^{\nu_{W_f}} \right. \\ &\quad \left. + \ln \frac{\eta_{W_v} \nu_{W_v}}{2\Gamma(1/\nu_{W_v})} - \left(\eta_{W_v}|W_g - W_f|\right)^{\nu_{W_v}} \right] \\ &= \arg\min_{W_f} \left[\left(\eta_{W_f}|W_f|\right)^{\nu_{W_f}} + \left(\eta_{W_v}|W_g - W_f|\right)^{\nu_{W_v}} \right] \end{aligned} \tag{3.31}$$

In [36] an optimized solution is proposed to solve (3.31) numerically.

Despite the expression in (3.31) may appear implicit, MAP estimator for the GG–GG model can be easily analysed as function of the parameters σ_{W_f}, σ_{W_v}, ν_{W_v} and ν_{W_f}. In Figure 3.7, a set of curves plotting $\hat{W}_f^{\mathrm{MAP}}$ v. W_g is given for particular values of such parameters: in Figure 3.7-(a), the curves refer to $\sigma_{W_f} = 2$, $\sigma_{W_v} = 1$, $\nu_{W_v} = 2$ and to ν_{W_f} varying from 0.4 to 2 with step 0.2; in Figure 3.7-(b), the parameter ν_{W_v} has been changed to 1.2 (the other parameters were not modified). Such curves define a remapping of the observed coefficients onto noise-free ones in a similar as done by hard and soft-thresholding schemes proposed commonly used for denoising signals affected by additive signal-independent noise [38, 39]. It is important, however, to point out that for despeckling the wavelet coefficients are modified according to the multiplicative model of speckle and thus adaptively vary according to the locally estimated parameters.

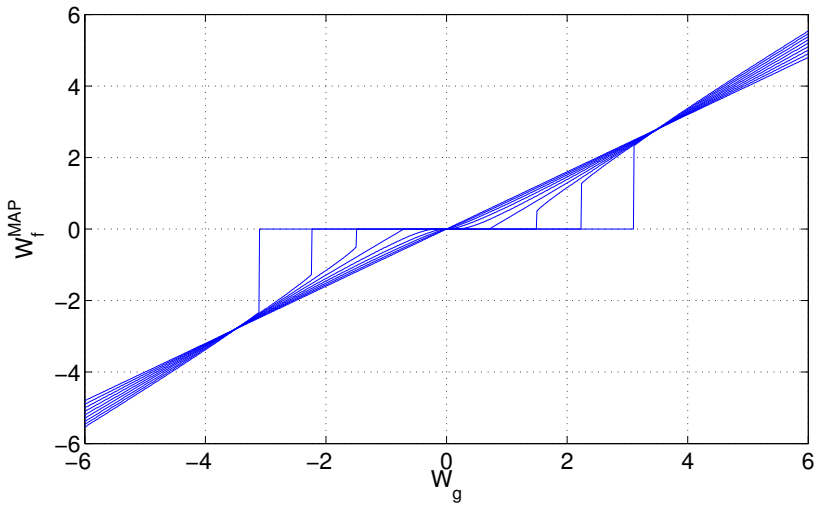

(a)

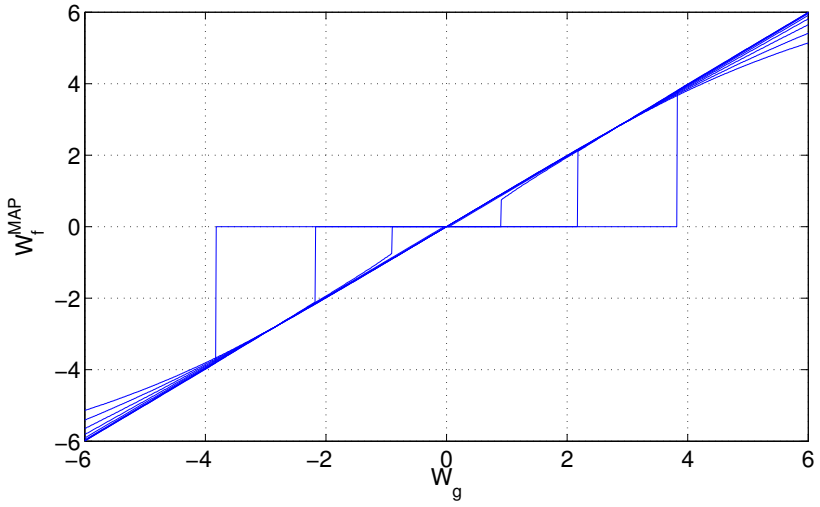

(b)

Figure 3.7: *Mapping of the $\hat{W}_f^{MAP}$ estimates vs. the observed W_g: in (a) $\sigma_{W_f} = 2$, $\sigma_{W_v} = 1$, $\nu_{W_v} = 2$ and ν_{W_f} varies from 0.4 to 2 with step 0.2; in (b) $\nu_{W_v} = 1.2$ (the other parameters are unchanged).*

MMSE estimator

The solution is given by

$$\hat{W}_f^{\mathrm{MMSE}} = \frac{\int_{-\infty}^{+\infty} W_f \frac{\eta_{W_f}\nu_{W_f}}{2\Gamma\left(1/\nu_{W_f}\right)} \exp\left\{\left[-\left(\eta_{W_f}|W_f|\right)^{\nu_{W_f}}\right]\right\}}{\int_{-\infty}^{+\infty} \frac{\eta_{W_f}\nu_{W_f}}{2\Gamma\left(1/\nu_{W_f}\right)} \exp\left\{\left[-\left(\eta_{W_f}|W_f|\right)^{\nu_{W_f}}\right]\right\}} \cdot \frac{\frac{\eta_{W_v}\nu_{W_v}}{2\Gamma(1/\nu_{W_v})} \exp\left\{[-(\eta_{W_v}|W_g - W_f|)^{\nu_{W_v}}]\right\}\, dW_f}{\frac{\eta_{W_v}\nu_{W_v}}{2\Gamma(1/\nu_{W_v})} \exp\left\{[-(\eta_{W_v}|W_g - W_f|)^{\nu_{W_v}}]\right\}\, dW_f} \,. \quad (3.32)$$

The integrals in (3.32) need to be computed by using numerical methods.

MMAE estimator

The solution can be found by solving

$$\phi_1(\hat{W}_f^{\mathrm{MMAE}}) = 0 \,,$$

where $\phi_1(x)$ is given by

$$\phi_1(x) \stackrel{\mathrm{def}}{=} \frac{\int_{-\infty}^{x} \frac{\eta_{W_f}\nu_{W_f}}{2\Gamma\left(1/\nu_{W_f}\right)} \exp\left\{\left[-\left(\eta_{W_f}|W_f|\right)^{\nu_{W_f}}\right]\right\}}{\int_{-\infty}^{+\infty} \frac{\eta_{W_f}\nu_{W_f}}{2\Gamma\left(1/\nu_{W_f}\right)} \exp\left\{\left[-\left(\eta_{W_f}|W_f|\right)^{\nu_{W_f}}\right]\right\}} \cdot \frac{\frac{\eta_{W_v}\nu_{W_v}}{2\Gamma(1/\nu_{W_v})} \exp\left\{[-(\eta_{W_v}|W_g - W_f|)^{\nu_{W_v}}]\right\}\, dW_f}{\frac{\eta_{W_v}\nu_{W_v}}{2\Gamma(1/\nu_{W_v})} \exp\left\{[-(\eta_{W_v}|W_g - W_f|)^{\nu_{W_v}}]\right\}\, dW_f} - \frac{1}{2} \,. \quad (3.33)$$

The integrals in (3.33) are computed numerically. The solution of the MMAE estimator can be determined by using numerical methods for finding the zeros of a function.

3.2.3 L–G model

The MAP and the MMSE estimators can be obtained in closed analytical forms [40].

MAP estimator

The solution is given by

$$\hat{W}_f^{\mathrm{MAP}} = \begin{cases} W_g - \rho, & \text{if } W_g > \rho \\ W_g + \rho, & \text{if } W_g < -\rho \\ 0 & \text{otherwise .} \end{cases} \tag{3.34}$$

Hence, MAP estimator is given by a simple soft–thresholding.

MMSE estimator

The solution is given by

$$\hat{W}_f^{\mathrm{MMSE}} = \frac{(W_g - \rho)\,\mathrm{A} + (W_g + \rho)\,\mathrm{B}}{\mathrm{A} + \mathrm{B}} \,. \tag{3.35}$$

Although (3.35) is expressed in a closed analytical form, the product between the exponential function and the complementary error function erfc may cause numerical instability and must be handled with care.

MMAE estimator

The solution can be found by solving

$$\phi_2(\hat{W}_f^{\mathrm{MMAE}}) = 0 \,, \tag{3.36}$$

where $\phi_2(x)$ is given by

$$\phi_2(x) \stackrel{\mathrm{def}}{=} \begin{cases} \dfrac{\exp(\varphi)\cdot\mathrm{erfc}\left(\psi + \frac{W_g - x}{\sqrt{2}\sigma_{W_v}}\right)}{\mathrm{A+B}} - \frac{1}{2}, & \text{if } x \leq 0 \\ -\dfrac{\exp(-\varphi)\cdot\mathrm{erfc}\left(\psi - \frac{W_g - x}{\sqrt{2}\sigma_{W_v}}\right)}{\mathrm{A+B}} + \frac{1}{2}, & \text{if } x > 0 \,. \end{cases} \tag{3.37}$$

The mathematical details of the derivation can be found in Section 3.5.1. The solution of the MMAE estimator can be determined with numeric routines for solving non-linear equations.

3.2.4 MIX–G model

By using the model in (3.19) for the reflectivity, only the MMSE estimator can be obtained in a closed analytical form; the MMAE requires finding the

zeros of a non-linear function, whereas the MAP is related to a maximum search.

MAP estimator

The solution is given by

$$\hat{W}_f^{\mathrm{MAP}} = \arg\max_{W_f} \left\{ \left[\alpha \frac{1}{\sqrt{2}\sigma_{W_f}} \exp\left(-\frac{\sqrt{2}|W_f|}{\sigma_{W_f}} \right) + (1-\alpha) \frac{1}{\sqrt{2\pi}\sigma_{W_f}} \exp\left(-\frac{{W_f}^2}{2{\sigma_{W_f}}^2} \right) \right] \cdot \frac{1}{\sqrt{2\pi}\sigma_{W_v}} \exp\left[-\frac{(W_g - W_f)^2}{2{\sigma_{W_v}}^2} \right] \right\} . \tag{3.38}$$

MMSE estimator

The solution is given by

$$\hat{W}_f = \frac{\alpha \exp(\psi^2) \left[(W_g - \rho)\,\mathrm{A} + (W_g + \rho)\,\mathrm{B} \right] + (1-\alpha)\, 2\sqrt{2}\sigma_{W_f} \cdot \mathrm{C}\,\mathrm{D}}{\alpha \exp(\psi^2)\,(\mathrm{A}+\mathrm{B}) + (1-\alpha)\, 2\sqrt{2}\sigma_{W_f}\mathrm{C}} . \tag{3.39}$$

The mathematical details are given in Section 3.5.2. Equation (3.39) is expressed in closed analytical form, but the product between the exponential function and the error function may be affected by numerical instability.

MMAE estimator

The solution is found by solving

$$\phi_3(\hat{W}_f^{\mathrm{MMAE}}) = 0 , \tag{3.40}$$

where $\phi_3(x)$ is defined by

$$\phi_3(x) \stackrel{\mathrm{def}}{=} \frac{\alpha \exp(\psi^2)\mathrm{F}(x) + (1-\alpha)\sqrt{2}\sigma_{W_f}\mathrm{C}\,\mathrm{erfc}\left[(\mathrm{D}-x)\left(\frac{\sqrt{1+\psi^2}}{\sqrt{2}\psi} \right) \right]}{\alpha \exp(\psi^2)\,(\mathrm{A}+\mathrm{B}) + (1-\alpha)\, 2\sqrt{2}\sigma_{W_f}\mathrm{C}} - \frac{1}{2} . \tag{3.41}$$

The mathematical details are given in Section 3.5.3. The solution of the MMAE estimator can be determined with any common method for finding

	GG–GG	L–G	MIX–G	G–G
MMSE	MMSE GG	MMSE LG	MMSE MIX	
MMAE	MMAE GG	MMAE LG	MMAE MIX	LMMSE
MAP	MAP GG	MAP LG	MAP MIX	

Table 3.1: *Acronyms of despeckling filters proposed in Section 3.2, for each estimation method (along columns) and statistical model (along rows).*

the zeros of a function. Moreover, the product between the exponential function and the error function may be affected by numerical instability.

Filters' acronyms

In the following of this thesis, the filters presented in Section 3.2 will be also referred by means of acronyms for sake of simplicity. They are reported in Table 3.1 for each combination of a statistical model with an estimation method.

3.2.5 Experimental results and comparison

Simulated Speckled Data

To assess the performances of the different despeckling filters tests on synthetically speckled images are presented. The test images data set includes four 512×512 8-bit grayscale images: *Lena*, *Barbara*, *Stockton*, *Aerial* (the last two images are aerial photos). The images have been taken from standard image databases and have been chosen for their different texture content: *Lena* and *Stockton* can be considered as containing smooth details, whereas *Barbara* and *Aerial* contain sharper details. The reader should consider that such original optical images play the role of the square root of noise–free reflectivities ($\sqrt{f}$); thus, in order to simulate the noisy acquisitions, they have been squared to obtain the noise-free SAR reflectivity, or, simply, noise-free image (f). Then they have been multiplied by a synthetic L-look speckle term to generate the noisy image or reflectivity (g). Results for $L = 1$ and $L = 4$ are presented. Bi-orthogonal 9/7 wavelet filters and four levels of decomposition have been used in all cases. Tables 3.2-3.5 report the values of peak-to-noise-ratio (PSNR) calculated between noise-free and filtered images obtained by using all the despeckling filters described in Section 3.2 (best and worst performances for each value of L are denoted

with bold and italic fonts, respectively). PSNR is defined as

$$\text{PSNR} = \frac{255^2}{MSE},$$

where MSE is the mean square error between the original optical image ($\sqrt{f}$) and the square root of the filtered reflectivity ($\sqrt{\hat{f}}$). The tables are organized in order to facilitate the reading of the results by using as a key either the estimation criterion or the pdf model.

As a first consideration, we observe that the texture content of the images has a strong influence on the performances of the filters. For sharp images (*Barbara* and *Aerial*), the results obtained with the different filters are quite uniform. For example, with a 1-look degradation, the difference Δ between the best and the worst performing filter is only $\Delta = 0.41$ dB for *Barbara* and $\Delta = 0.52$ dB for *Aerial*. For smooth images (*Lena* and *Stockton*), the use of different filters has a greater influence on the results, being, for 1-look degradation, $\Delta = 1.8$ dB and $\Delta = 1.5$ dB for *Lena* and *Stockton*, respectively.

Furthermore, from the observation of Tables 3.2-3.5, we can understand that sharper images are more difficult to be filtered. In fact, considering the filtering gain, i.e., the difference between the raw PSNR (computed between the original and the noisy image) and the PSNR after filtering, we see that smooth images (*Lena* and *Stockton*) exhibit a larger filtering gain than sharp images (*Barbara* and *Aerial*).

From the observation of Table 3.2, relative to the image *Lena*, we observe that MAP estimation outperforms the other estimation criteria independently from the used pdf modelling, being the GG-GG model the best performing one. If, instead, we analyse the results of the different pdf models given an estimation criterion, we observe that the GG-GG model outperforms the others (in 8 cases over 9), even though the differences with the L-G model are quite small.

From the results in Table 3.4, relative to the image *Stockton*, we observe a behaviour similar as that of the image *Lena*. In fact, MAP is the best estimation criterion (in almost all cases), whereas the GG–GG model outperforms the other pdf models. We also observe that the L-G model yields results close to the GG-GG model especially when the MAP estimation is used.

If we analyse the results relative to the sharp images (*Barbara* and *Aerial*), presented in Tables 3.3 and 3.5, being the differences among the filters quite limited, it is more difficult to extrapolate a clear trend about the influence of modelling and estimators. In these highly detailed images, we observe also that the MMAE criterion very often obtains a performance close to that of

the best estimation criterion.

Computing times have been calculated and are shown in Table 3.6. The GG–GG model exhibits affordable processing times only for the MAP case, which incidentally is the most performing. The L–G model represents the best trade off between computational cost and filtering performances. The MMAE estimator is not affordable, except for the trivial G–G case.

	Number of looks					
	1 (raw = 12.08)			4 (raw = 17.77)		
	MMSE	MMAE	MAP	MMSE	MMAE	MAP
GG–GG	25.28	25.25	**26.39**	28.99	29.05	**29.71**
L–G	25.02	25.38	26.21	28.76	29.01	29.41
MIX–G	24.80	25.00	25.57	28.68	28.86	29.26
G–G (LMMSE)		*24.59*			*28.57*	

Table 3.2: *PSNR (dB) obtained on Lena corrupted by various noise patterns.*

	Number of looks					
	1 (raw = 12.33)			4 (raw = 18.01)		
	MMSE	MMAE	MAP	MMSE	MMAE	MAP
GG–GG	22.57	*22.46*	**22.87**	26.25	26.19	**26.29**
L–G	22.77	22.85	22.85	26.09	26.12	*25.85*
MIX–G	22.67	22.72	22.72	26.14	26.17	26.07
G–G (LMMSE)		22.59			26.18	

Table 3.3: *PSNR (dB) obtained on Barbara corrupted by various noise patterns.*

	Number of looks					
	1 (raw = 11.74)			4 (raw = 17.42)		
	MMSE	MMAE	MAP	MMSE	MMAE	MAP
GG–GG	25.27	25.34	25.72	27.55	27.60	**27.70**
L–G	24.61	25.00	**25.75**	27.29	27.48	27.69
MIX–G	24.42	24.64	25.18	27.24	27.38	27.63
G–G (LMMSE)		*24.25*			*27.16*	

Table 3.4: *PSNR (dB) obtained on* Stockton *corrupted by various noise patterns*

(a) (b)

(c) (d)

Figure 3.8: *Original test images: (a) Lena; (b) Barbara; (c) Stockton; (d) Aerial.*

Figure 3.9: *Results obtained with the test images Lena (a)-(c) and Aerial (d)-(f) degraded with 4-look speckle: noisy images (top); the best (middle) and the worst results (bottom) achieved according to Tables 3.2 and 3.5.*

	Number of looks					
	1 (raw = 9.23)			4 (raw = 14.92)		
	MMSE	MMAE	MAP	MMSE	MMAE	MAP
GG–GG	20.77	**20.82**	20.67	23.54	23.51	23.42
L–G	20.45	20.67	20.71	23.47	23.55	*23.32*
MIX–G	20.39	20.51	20.72	23.50	23.56	**23.57**
G–G (LMMSE)		*20.30*			23.48	

Table 3.5: *PSNR (dB) obtained on* Aerial *corrupted by various noise patterns.*

	GG–GG	L–G	MIX–G	G–G
MMSE	10^5	10^1	10^1	10^1
MMAE	10^5	10^1	$10^3 \div 10^4$	10^1
MAP	10^2	10^1	$10^3 \div 10^4$	10^1

Table 3.6: *Execution times (order of magnitude in seconds) of the different despeckling filters.*

COSMO-SkyMed Data

A true X-band SAR image produced by the COSMO-SkyMed satellite constellation of the Italian Space Agency has been processed for despeckling. The image has been acquired and processed in HImage Stripmap mode and is stored in a single look complex format. The detected intensity image, having having theoretical SNR equal to 0 dB, spatial resolution of approximately three meters and containing both natural and man-made structures, is believed to provide a challenging subject for despeckling.

Fig. 3.10 shows the original SAR image, in which five homogeneous areas, identified with capital letters, have been used for the estimation of the equivalent number of look (ENL) after filtering, a quantitative measure of the filtering gain commonly used when a reference image is not available [11][17]. ENL is defined as

$$\mathrm{ENL} = \frac{\mu_{\hat{f}}^2}{\sigma_{\hat{f}}^2},$$

being $\mu_{\hat{f}}$ and $\sigma_{\hat{f}}^2$ are the mean and the variance of the filtered reflectivity, respectively, calculated on the considered portion. A visual comparison of the filtered images is presented in Fig. 3.11. The despeckling filters selected for this comparison are those characterised by the MAP estimation criterion (for all the pdf models) or by the L–G pdf model (for all the estimation

criteria). The result obtained with the LMMSE filter is also shown. The ENL computed after filtering in the five homogeneous areas are reported in Table 3.7.

From Fig. 3.11 and from table 3.7 it can be observed that MAP filters based on GG–GG and on L–G models are comparable in performances, even though the one based on GG–GG modelling seems to be slightly more accurate on textures. However, the L–G MAP filtering allows a significant computational saving to be achieved. Conversely, the LMMSE estimator is somewhat poorer, especially in homogeneous areas, but also on textures.

It is important to highlight that true SAR images differ from simulated speckled images because the fully developed multiplicative speckle model does not hold on highly heterogeneous areas and strong scatterers. Hence, a preprocessing step of point targets, and thicker strong scatterers in general, images has been applied for filtering the COSMO–SkyMed. As proposed in [41], targets are firstly detected as upper percentiles of the noisy image histogram, clipped to the threshold value and their original values are stored. Then, wavelet analysis is performed. After synthesis of the despeckled image, point targets are reinserted in their original places.

Actually, adjustments of Bayesian estimators to SAR scene heterogeneity are contained in [35][41] and allow a superior despeckling performance to be achieved on highly heterogeneous textures and target. This topic will be discussed in Section 3.3.

	A	B	C	D	E
raw	0.89	0.94	0.96	1.00	1.00
MAP GG–GG	14.37	13.93	23.29	24.00	18.24
MAP MIX–G	12.78	12.60	19.21	18.96	15.03
MAP L–G	14.77	15.05	22.72	23.36	18.66
MMAE L–G	10.34	10.22	16.27	14.48	12.39
MMSE L–G	9.48	9.37	13.23	13.04	11.14
LMMSE	8.59	8.56	11.62	11.90	10.19

Table 3.7: *ENL obtained on different areas of the COSMO-SkyMed test image.*

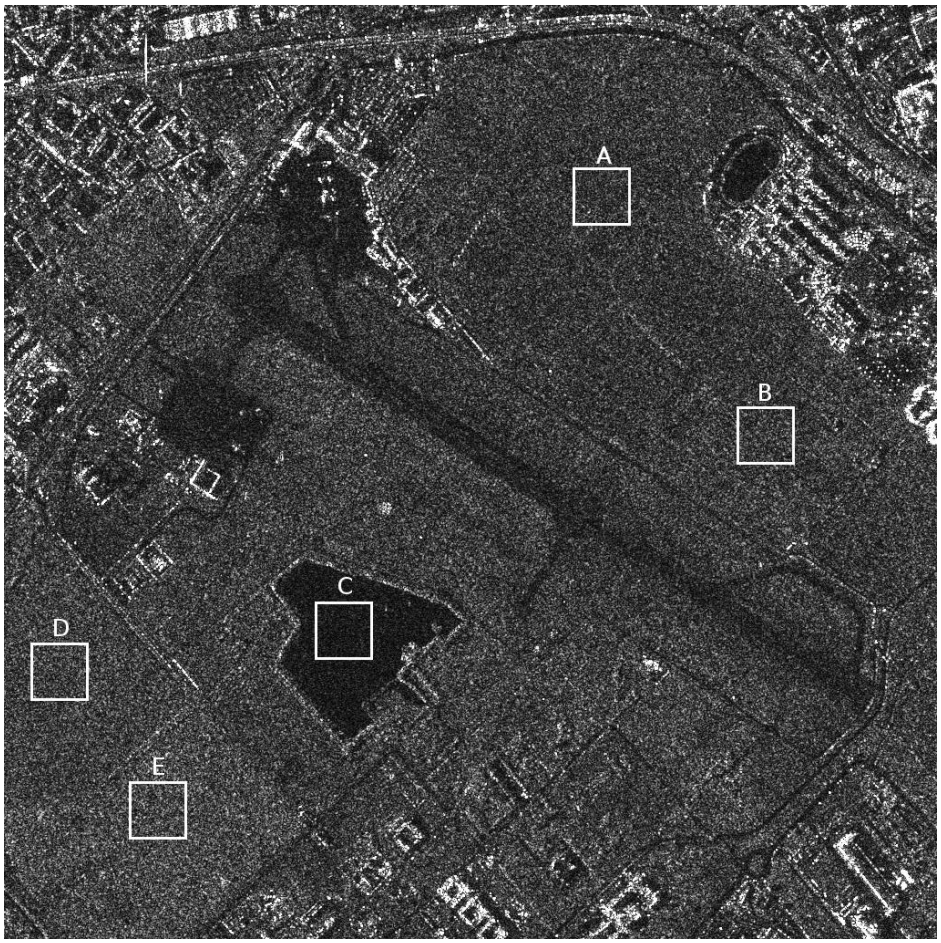

Figure 3.10: *Original COSMO-SkyMed image (*1024×1024*, 3m resolution): five homogeneous areas are denoted with capital letters and used for ENL estimation.*

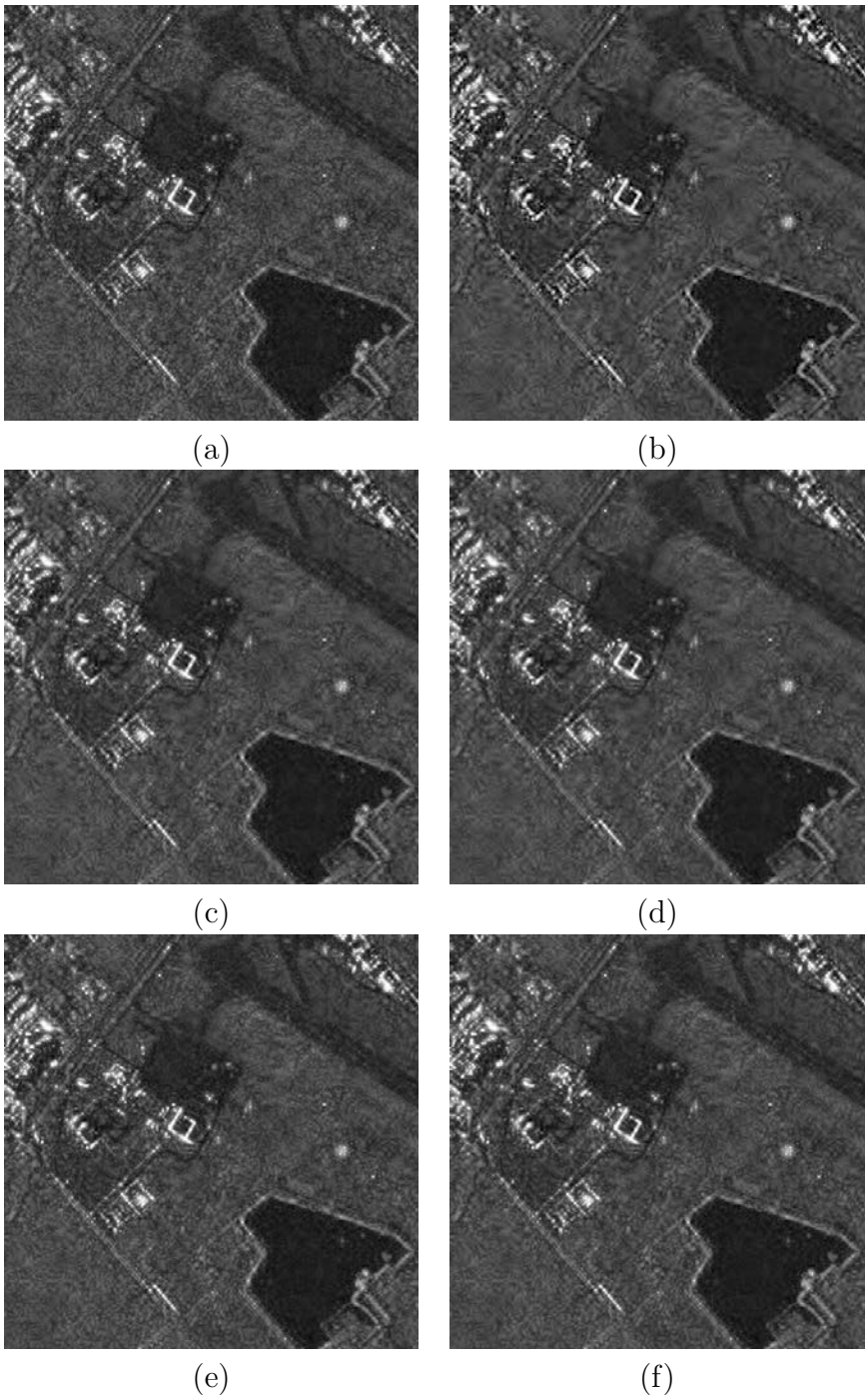

Figure 3.11: *Results obtained despeckling the test single look COSMO-SkyMed image (a detail is visualised) with different filters: (a) LMMSE; (b) GG–GG model & MAP; (c) MIX–G model & MAP; (d) L–G model & MAP; (e) L–G model & MMSE; (f) L–G model & MMAE.*

3.3 Segmentation and classification in UDWT domain

3.3.1 Adjustments for SAR image heterogeneity

In several despeckling methods, different filtering strategies are used according to the texture content of the scene. In [42, 43], the coefficient of variation is used to discriminate among homogeneous, textured and highly heterogeneous (or point target) areas. Pixel belonging to the first two classes are filtered by using simple averaging and Γ-MAP, or another local-statistics filter, whereas no filtering is attempted on point targets. A strongly scattering target, however, is concentrated in space, but after wavelet analysis its response will be somewhat spread because of the finite support of the wavelet function. Thus, also UDWT coefficients around a point target one pixel wide will depend on the target response, unlike what happens in space. In the past, this was perhaps the main objection towards a systematic use of the wavelet transform to analyze SAR images.

Starting from [41], the proposal of a preprocessing step for point targets, as described in Section 3.2.5, has allowed to contain the effect of strong scatterers when despeckling is performed in the transformed domain. Nevertheless, the main contribution of that paper is the introduction of *segmentation* in the UDWT domain. Specifically, UDWT subbands are segmented into texture classes according to an energy index computed in the UDWT domain. For each subband, several classes of texture, from textureless (or homogeneous) to increasing textured levels, can be recognized. Homogeneous class is usually the most populated and the statistical parameters are calculated on a local basis for each wavelet coefficient belonging to it. On the other side, the wavelet coefficients of each specific textured segment are supposed to follow a unique shape factor of the GG function. Thus, the calculation of the ν is more accurate than in [36], thanks to the more consistent sample size. Such a segmentation processing allowed the authors to propose an improved version of the MAP GG filter, which, in the remaining of this thesis, it will be referred to as the GG MAP-S filter. In Figure 3.12-(b) and 3.12-(c), the results of LMMSE and GG MAP-S filtering on the image in Figure 3.12-(a) are respectively shown. Furthermore, Figure 3.12-(d) reports the result obtained by means of LG MAP-S filter, which will be introduced in Section 3.3.2.

A segmentation based approach seems also a natural solution to changes in the speckle model occurring as the spatial resolution of single-look products increases. This happens for very high resolution (VHR) new generation SAR

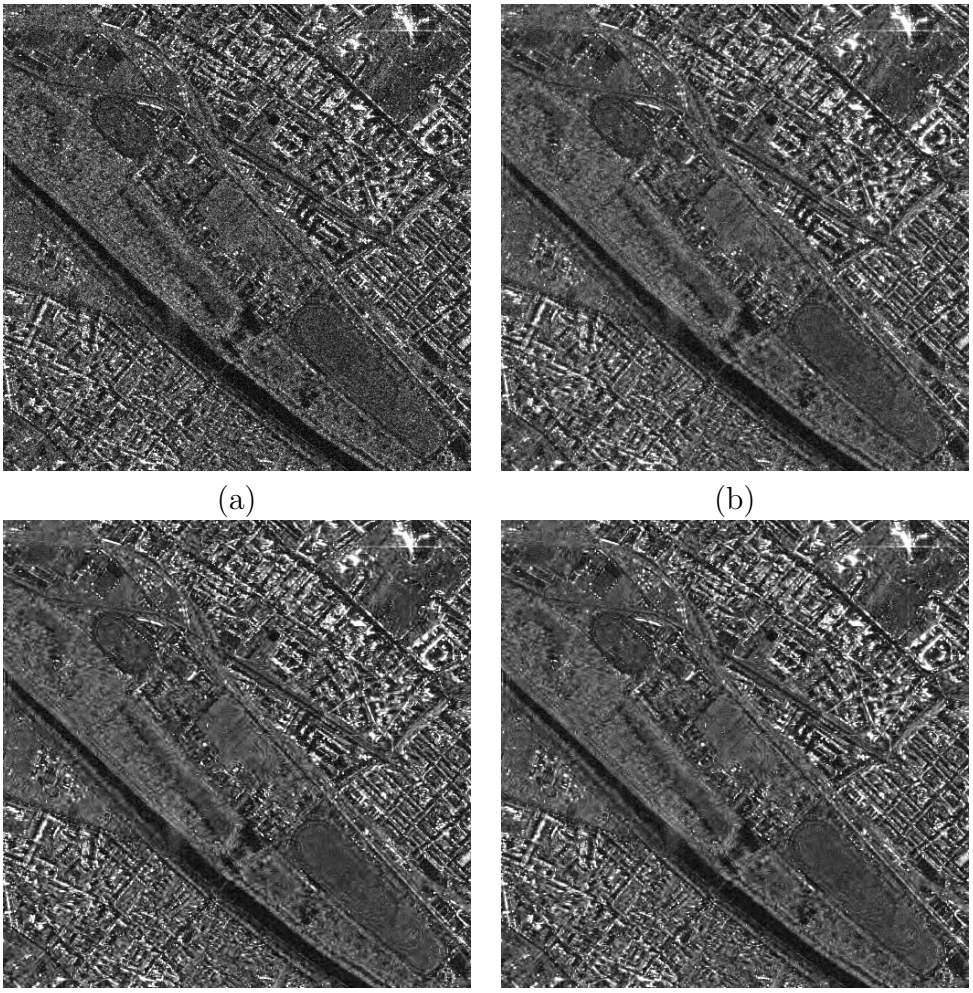

Figure 3.12: *Examples of the application of Bayesian estimators in the UDWT domain: (a) original COSMO-SkyMed 4-look StripMap image; filtered versions obtained with (b) LMMSE; (c) MAP GG with segmentation (GG MAP–S) (d) MAP-LG with classification (LG MAP–S).*

systems, especially with Spotlight products. As the size of the elementary resolution cell decreases, the assumption of *distributed scatterers* is less and less verified. In substance, what is homogeneous at 10 m scale may no longer be so at 1 m. So, VHR SAR images are expected to be more textured and contain more persistent scatterers, and less homogeneous regions, than earlier products. A viable solution with segmented processing in UDWT domain is introducing corrective factors for undersmoothing in textured segments, depending on the class of texture energy measured in the UDWT domain, analogously to what proposed in [35].

3.3.2 MAP LG despeckling based on classification of wavelet coefficients

In [41], it was demonstrated that the performance of the MAP GG filter can be noticeably improved using a segmented approach, where each wavelet subband is divided into different classes of heterogeneity according to the texture energy of the wavelet coefficients of noise–free reflectivity. The key point is to assume that the wavelet coefficients within a particular class follow the same GG distribution, so that the parameters of the GG–GG model can be accurately estimated within each class.

As in the case of the GG-based MAP solution, also for the L–G based method an improvement in performances can be achieved by using a *classification* of wavelet coefficients according to their texture content. The main idea is that segmentation can be used, at a very little additional cost, to select classes of wavelet coefficients to which apply different fast filters, or even no filtering at all. The computational cost can be reduced of one order of magnitude or more with respect to the solution obtained numerically with the GG–GG model assumption, without significantly affecting the performance in terms of speckle reduction.

Here, the key observation is that the L–G model may be well suited only for a particular class of heterogeneity, whereas for other classes it may be better to use alternative models. According to the class each wavelet coefficient belongs to, we propose to apply the following three processing strategies.

- Wavelet coefficients belonging to the lower energy class are processed by means of the MAP LG filter reported in (3.34). This class represents the set of coefficients of weakly textured areas, or homogeneous areas, which are better modelled by the assumption of Laplacian distribution.

- Wavelet coefficients belonging to the middle energy class are processed by means of the LMMSE filter reported in (3.8). The LMMSE filter is

a general–purpose first–order approximation filter and it represents the optimal MAP filter when both the coefficients of noise–free reflectivity and the coefficients of speckle noise follow a normal distribution. We assume that this hypothesis is sufficiently valid for coefficients belonging to heterogeneous areas.

- Wavelet coefficients belonging to the last class are supposed to represent strongly heterogeneous areas or point targets. Because these areas do not follow any longer the fully–developed speckle model, the wavelet coefficients of the last class are left unchanged.

In the following of this thesis, the above filtering strategy will be referred to as LG MAP-S filter.

3.3.3 Experimental results and comparison

In order to ascertain the performance loss/gain of the LG versus the GG assumption, a first set of quantitative results obtained by using a 8 bit 512×512 test image (*Lena*), degraded by synthetically generated speckle noise according to the model in (2.13), are shown. Then, some results derived from true SAR images are also presented. In the case of synthetically generated speckle degradation, the quality of the filtered image can be measured by means of PSNR. A more general method to assess the effectiveness of the different filters, which can be used also when the noise-free reference image is not available, is based on the statistics of the ratio image, defined as

$$\hat{u} = g/\hat{f},$$

where $\hat{f}$ represents the estimated noise–free reflectivity. When a fully developed speckle model can be assumed, the above image represents the filtered out speckle noise. Hence, for a good despeckling filter $\hat{u}$ should satisfy $E[\hat{u}] = 1$ and $Var[\hat{u}] = 1/L$, where L is the number of look [11]. The mean and the variance of the ratio image are estimated by using a scatter plot method similar to that proposed in [44]. The method consists of the following steps. First, a scatter plot is obtained by plotting the occurrences of each pair of local mean and standard deviation, calculated on a moving local window over the image $\hat{u}$. Hence, the bivariate pdf is estimated from the scatter plot, and the mean and standard deviation of $\hat{u}$ are estimated as the coordinates of the maximum of the bivariate pdf. The rationale of this method is based on the assumption that each local window would give a contribution centered on such a maximum if the size of the window is sufficiently large. Thanks to using statistics computed on local windows, the above method is

accurate also in the case of real SAR images, for which the assumption of fully–developed speckle is not valid everywhere and global statistics would be biased due to the presence of outliers.

The despeckling filters that are compared in the following are: 1) the LMMSE filter [35]; the GG MAP-S filter [41]; the MAP LG filter proposed in Section 3.2.3; the LG MAP-S filter proposed in section 3.3.2. All filters use a 9/7 biorthogonal wavelet with four multiresolution levels.

In Table 3.8, the performance of the despeckling filters are compared in terms of PSNR. The order of magnitude of the computational times, expressed in seconds and related to our Matlab implementation, are shown in Table 3.9. As can be seen, the complexity of the LG filters is the same as the LMMSE one. However, especially for multilook images, the performance of the LG MAP-S filter is very close to that of the GG-MAP-S filter, showing that a valuable computational gain is achieved at the price of almost unaltered performances in terms of PSNR. These results are confirmed by the observation of Table 3.10, where the mean and the variance of $\hat{u}$, estimated by using the scatter plot method on the test image *Lena* for the different algorithms, are shown.

Table 3.8: *PSNR obtained by using Lena degraded by synthetically generated speckle.*

	1-look	2-look	4-look	16-look
LMMSE	24.59	26.62	28.57	32.61
GG MAP-S	26.40	28.04	29.77	33.24
MAP LG	26.21	27.77	29.41	32.95
LG MAP-S	26.21	27.82	29.55	33.27

Table 3.9: *Order of magnitude of the computational times (in seconds) of the analyzed algorithms for* 512×512 *images. Tests have been performed on a 2.40 GHz CPU with 4GB RAM.*

	computational cost (s)
LMMSE	10^1
GG MAP-S	10^2
MAP LG	10^1
LG-MAP-S	10^1

As to the results on true SAR data, they have been assessed by using a 8 bit 512×512 4-look X-HH image representing an airport in Ontario, and a 16

Table 3.10: *Mean and variance of extracted noise $\hat{u}$, measured on synthetically corrupted Lena through scatter-plot method.*

	1-look		2-look		4-look		16-look	
	$\mu_{\hat{u}}$	$\sigma^2_{\hat{u}}$	$\mu_{\hat{u}}$	$\sigma^2_{\hat{u}}$	$\mu_{\hat{u}}$	$\sigma^2_{\hat{u}}$	$\mu_{\hat{u}}$	$\sigma^2_{\hat{u}}$
LMMSE	0.928	0.698	0.957	0.360	0.975	0.186	0.992	0.047
GG MAP-S	0.985	0.936	0.988	0.476	0.992	0.239	0.997	0.060
MAP LG	0.979	0.897	0.985	0.455	0.989	0.230	0.994	0.058
LG MAP-S	0.979	0.897	0.985	0.455	0.989	0.230	0.995	0.057

bit 1024×1024 COSMO-SkyMed 1-look X-HH image representing an area in Veneto, Italy. The original *Airport* and *Veneto* images are shown in Figure 3.13. Two portions of the above images, together with the despeckled versions obtained with the LMMSE, GG MAP-S, MAP LG, and LG MAP-S filters, are shown in Figure 3.14 and in Figure 3.15, respectively. In Table 3.11, the mean and the variance of $\hat{u}$, estimated on the *Airport* and *Veneto* images using the scatter plot method, are shown. From Table 3.11, we observe that the LG methods have similar performances as the GG MAP-S method and outperform the LMMSE one. It can be also observed that the performances of the LG MAP and of the LG MAP-S are almost identical, highlighting that they behave in the same way in homogeneous areas. However, comparing Figures 3.14-(c) and 3.14-(d) (and, similarly,Figures 3.15-(c) and 3.15-(d)), we observe that the LG MAP-S yields a better preservation of texture details. As to the *Veneto* image, we notice that $\sigma^2_{\hat{u}}$ is underestimated with respect to the nominal value 1. This is probably due to the fact that *Veneto* images present correlated speckle.

Table 3.11: *Mean and variance of extracted noise $\hat{u}$, measured on nominal 4-look SAR image Airport and nominal 1-look SAR image COSMO-SkyMed through scatter-plot method.*

	Airport		COSMO-SkyMed	
	$\mu_{\hat{u}}$	$\sigma^2_{\hat{u}}$	$\mu_{\hat{u}}$	$\sigma^2_{\hat{u}}$
LMMSE	0.9298	0.1584	0.8592	0.4044
GG-MAP-S	0.9722	0.2878	0.9237	0.5916
LG-MAP	0.9606	0.2540	0.8916	0.5463
LG-MAP-S	0.9583	0.2515	0.8905	0.5348

The effectiveness of despeckling filters on textured areas can be better

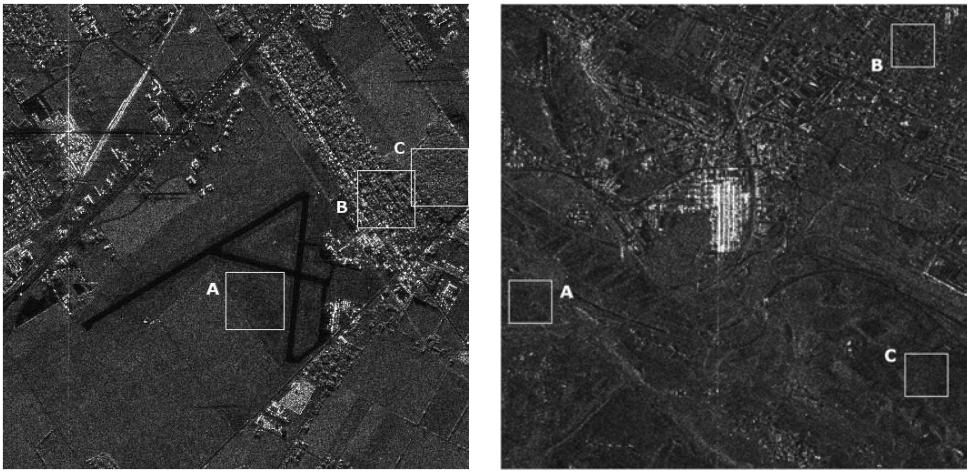

Figure 3.13: *SAR images* Airport *(left) and* Veneto *(right). The scene coefficient of variation C_f has been estimated in the highlighted areas.*

evaluated by using the *scene coefficient of variation* [11], defined as

$$C_f = \sqrt{(C_g^2 - \sigma_u^2)/(1 + \sigma_u^2)} \tag{3.42}$$

where $C_g = \sigma_g/\mu_g$ is the coefficient of variation of the original image, σ_g and μ_g are, respectively, the estimated standard deviation and the estimated mean of the observed signal, and σ_u is the estimated standard deviation of the speckle noise. Under the fully developed speckle model, an image processed by a good despeckling filter should yield a coefficient of variation $C_{\hat{f}} = \sigma_{\hat{f}}/\mu_{\hat{f}}$ as close as possible to the corresponding C_f. The scene coefficient of variation has been evaluated on three 64×64 areas of *Airport* and three 96×96 areas of *Veneto*, characterized by different features of the underlying scene, as shown in Figure 3.13, and compared to the $C_{\hat{f}}$ obtained with the different filters. The results are presented in Table 3.12. The LG-MAP-S filter shows a behaviour very close to the GG-MAP-S in each analyzed area. Interestingly, all filters tend to overestimate the C_f for the *Veneto* image. This is in accordance with the estimated $\sigma_{\hat{u}}^2$, and can be explained by the presence of spatially correlated speckle.

3.4 Conclusions

In this chapter, Bayesian estimators and different models for the pdf of wavelet coefficients have been used to implement several non-homomorphic

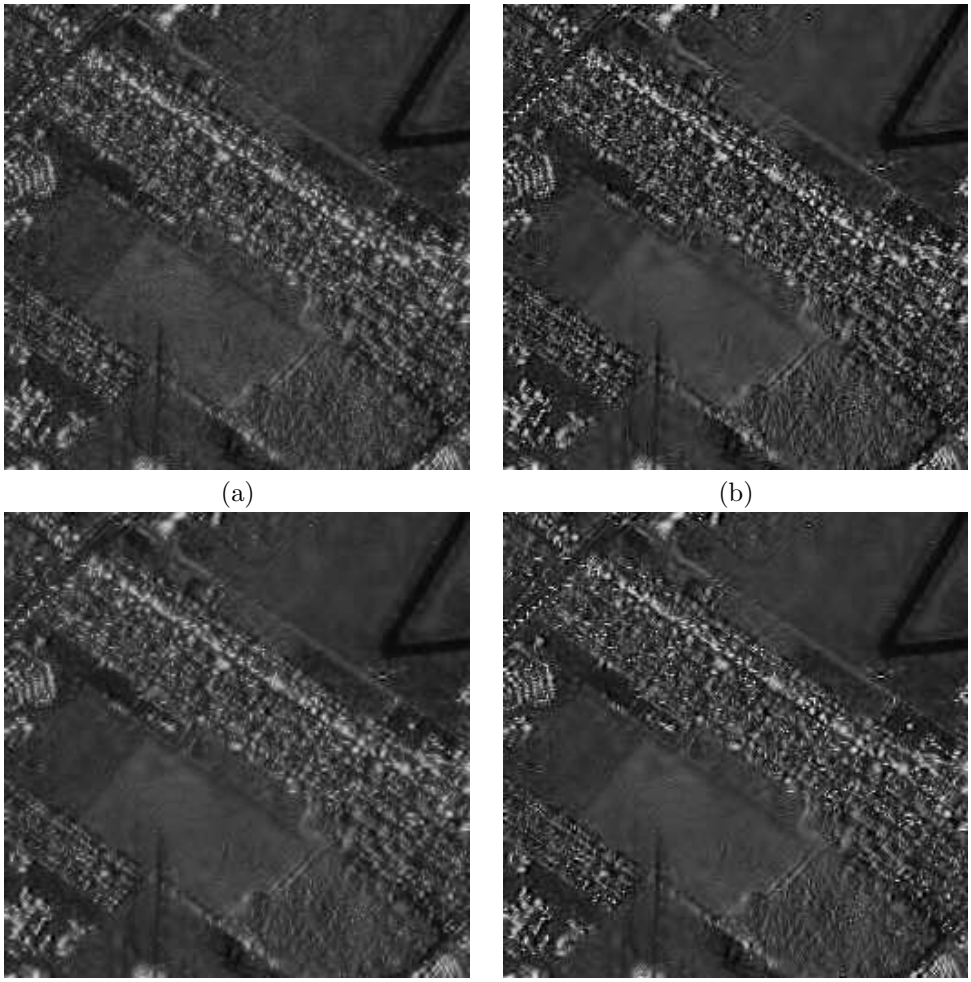

(a) (b) (c) (d)

Figure 3.14: *Results obtained by filtering 4-look Airport image (left): (a) LMMSE; (b) GG MAP-S; (c) MAP LG; (d) LG MAP-S.*

Table 3.12: *Scene coefficients of variation (C_f) obtained on three 64×64 areas of Airport and three 96×96 areas of COSMO-SkyMed.*

	Airport			COSMO-SkyMed		
	A	B	C	A	B	C
C_f	0.426	1.245	0.770	0.791	3.108	0.442
LMMSE	0.367	1.002	0.606	1.048	4.118	0.502
GG MAP-S	0.325	1.223	0.733	1.040	4.123	0.479
MAP LG	0.312	0.937	0.530	1.016	4.100	0.437
LG MAP-S	0.317	1.158	0.646	1.027	4.127	0.446

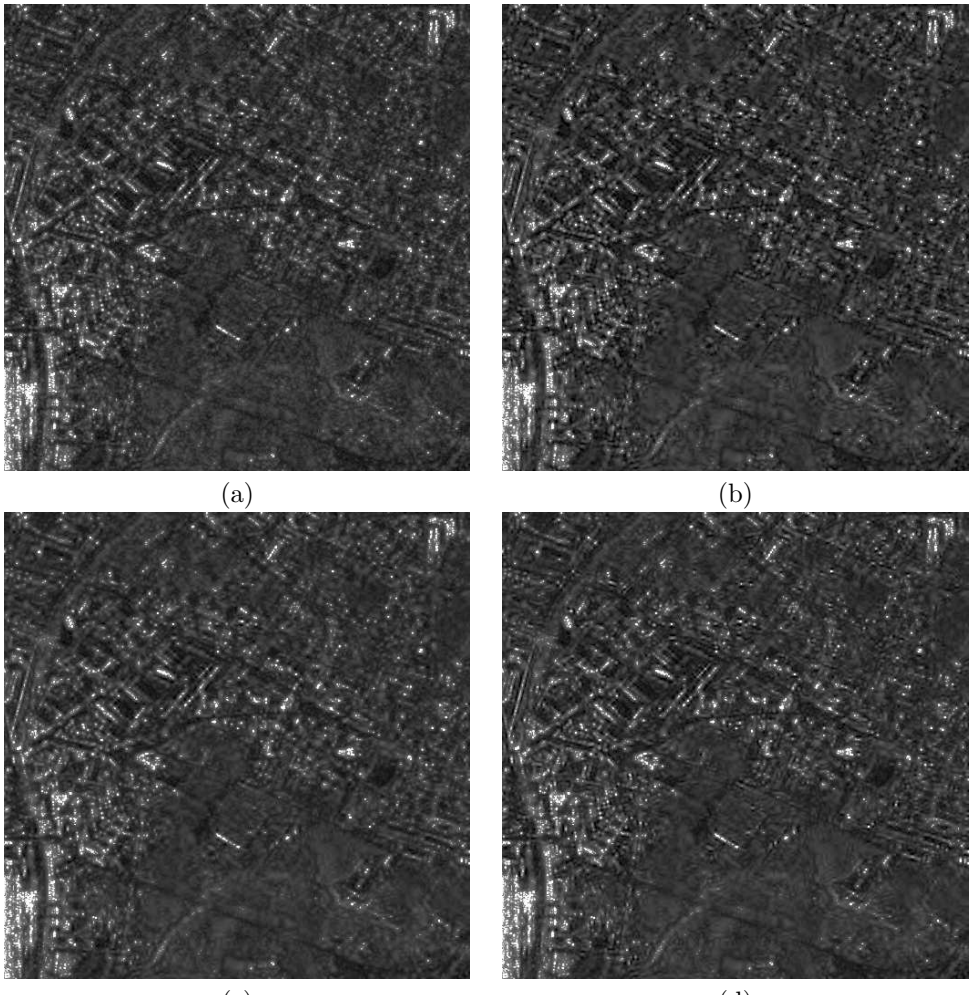

Figure 3.15: *Results obtained by filtering 4-look COSMO-SkyMed image (left): (a) LMMSE; (b) GG MAP-S; (c) MAP LG; (d) LG MAP-S.*

despeckling filters in the undecimated wavelet domain. Classical MMSE, MMAE and MAP estimator and different unimodal pdf models have been chosen. Some of the filtering solutions were already considered in the literature, whereas some others are an original contribution of this study.

The availability of the whole set of filters coming from the different combinations and the comparison of their performances have allowed us to assess the influence of either the type of estimator or the pdf model on the achieved performance. Analysing the results obtained with synthetically speckled images, we have observed that the proposed filters have a different behaviour depending on the content of the image. On images with smooth details, the best results come from the maximum a-posteriori (MAP) estimator with coefficients of reflectivity and noise both modelled as generalized Gaussian (GG) densities. However, MAP estimation with Laplacian reflectivity and Gaussian noise provides comparable results with a computational complexity more than ten times lower, thanks to the closed-form analytical solution. On images with sharp details, the performances of the proposed filters are quite similar and the characteristics of the best filter can not be easily identified.

The proposed filters have been also tested on true high-resolution single-look X-band SAR images (Cosmo–SkyMed). Filtering results achieved on the Cosmo-SkyMed SAR image seems to confirm those achieved on synthetically speckled images.

The Laplacian-Gaussian modeling is also combined with a segmentation-based approach, in which different filtering strategies are applied according to the classification of wavelet coefficients. The experimental results show that the performance of the fast algorithm, assessed on both simulated speckled images and on high-resolution SAR images, are comparable with those of the segmentation-based MAP GG solution, with a computational complexity more than ten times lower.

3.5 Appendix

In this section, for the sake of clarity, the quantities θ, r and x will replace W_f, W_v and W_g, in that order. Moreover the definitions given in equations (3.21) – (3.29) are used.

3.5.1 L–G model: derivation of MMAE estimator

In order to evaluate the MMAE estimator, the numerator and the denominator in equation (3.9) are needed.

As to the denominator, according to the L–G model

$$p_X(x) = \int_{-\infty}^{+\infty} \frac{1}{\sqrt{2}\sigma_\theta} \exp\left(-\frac{\sqrt{2}|\theta|}{\sigma_\theta}\right) \frac{1}{\sqrt{2\pi}\sigma_r} \exp\left[-\frac{(x-\theta)^2}{2{\sigma_r}^2}\right] d\theta$$
$$= \frac{1}{2\sqrt{\pi}\sigma_\theta\sigma_r} \left[\int_{-\infty}^{0} e^{-\frac{(x-\theta)^2}{2\sigma_r^2}+\frac{\sqrt{2}\theta}{\sigma_\theta}}\, d\theta + \int_{0}^{+\infty} e^{-\frac{(x-\theta)^2}{2\sigma_r^2}-\frac{\sqrt{2}\theta}{\sigma_\theta}}\, d\theta\right] . \quad (3.43)$$

The second integral can be written, after some manipulation, as

$$\int_0^\infty e^{-\frac{(x-\theta)^2}{2\sigma_r^2}-\frac{\sqrt{2}\theta}{\sigma_\theta}}\, d\theta = \int_0^\infty e^{-\frac{1}{2\sigma_r^2}\left(\theta-x+\frac{\sqrt{2}\sigma_r^2}{\sigma_\theta}\right)^2}\, d\theta \cdot e^{\left(\frac{\sigma_r}{\sigma_\theta}\right)^2-\frac{\sqrt{2}x}{\sigma_\theta}}$$
$$= \sqrt{\frac{\pi}{2}}\sigma_r \mathrm{A} \cdot e^{\psi^2}. \quad (3.44)$$

In an analogous way, it can be shown that the first integral in (3.43) can be written as

$$\int_{-\infty}^0 e^{-\frac{(x-\theta)^2}{2\sigma_r^2}+\frac{\sqrt{2}\theta}{\sigma_\theta}}\, d\theta = \int_{-\infty}^0 e^{-\frac{1}{2\sigma_r^2}\left(\theta-x-\frac{\sqrt{2}\sigma_r^2}{\sigma_\theta}\right)^2}\, d\theta \cdot e^{\left(\frac{\sigma_r}{\sigma_\theta}\right)^2+\frac{\sqrt{2}x}{\sigma_\theta}}$$
$$= \sqrt{\frac{\pi}{2}}\sigma_r \mathrm{B} \cdot e^{\psi^2}. \quad (3.45)$$

Joining the results in (3.44) and (3.45) yields

$$p_X(x) = \frac{1}{2\sqrt{2}\sigma_\theta} e^{\psi^2} (B + A) \ . \quad (3.46)$$

As to the numerator in equation (3.9)

$$\int_{-\infty}^{\hat{\theta}} p_\Theta(\theta) p_R(x-\theta)\, d\theta = \frac{1}{2\sqrt{\pi}\sigma_\theta\sigma_r} \int_{-\infty}^{\hat{\theta}} e^{-\frac{(x-\theta)^2}{2\sigma_r^2}-\frac{\sqrt{2}|\theta|}{\sigma_\theta}}\, d\theta\,. \quad (3.47)$$

Hence, if $\hat{\theta} \leq 0$, we have

$$\int_{-\infty}^{\hat{\theta}} e^{-\frac{(x-\theta)^2}{2\sigma_r^2}+\frac{\sqrt{2}\theta}{\sigma_\theta}}\, d\theta = \int_{-\infty}^{\hat{\theta}} e^{-\frac{1}{2\sigma_r^2}\left(\theta-x-\frac{\sqrt{2}\sigma_r^2}{\sigma_\theta}\right)^2}\, d\theta \cdot e^{\left(\frac{\sigma_r}{\sigma_\theta}\right)^2+\frac{\sqrt{2}x}{\sigma_\theta}}$$
$$= \sqrt{\frac{\pi}{2}}\sigma_r \mathrm{erfc}\left(\psi + \frac{x-\hat{\theta}}{\sqrt{2}\sigma_r}\right) \cdot e^{\psi^2+\varphi}\ , \quad (3.48)$$

whereas, for $\hat{\theta} > 0$, we have

$$\begin{aligned}
&\int_{-\infty}^{0} e^{-\frac{(x-\theta)^2}{2\sigma_r^2}+\frac{\sqrt{2}\theta}{\sigma_\theta}}\, d\theta + \int_{0}^{\hat{\theta}} e^{-\frac{(x-\theta)^2}{2\sigma_r^2}-\frac{\sqrt{2}\theta}{\sigma_\theta}}\, d\theta \\
=&\sqrt{\frac{\pi}{2}}\sigma_r \mathrm{B}\cdot e^{\psi^2} + \int_{0}^{\hat{\theta}} e^{-\frac{1}{2\sigma_r^2}\left(\theta-x+\frac{\sqrt{2}\sigma_r^2}{\sigma_\theta}\right)^2} d\theta \cdot e^{\left(\frac{\sigma_r}{\sigma_\theta}\right)^2-\frac{\sqrt{2}x}{\sigma_\theta}} \\
=&\sqrt{\frac{\pi}{2}}\sigma_r\,(\mathrm{A}+\mathrm{B})\cdot e^{\psi^2} - \sqrt{\frac{\pi}{2}}\sigma_r \mathrm{erfc}\left(\psi - \frac{x-\hat{\theta}}{\sqrt{2}\sigma_r}\right)\cdot e^{\psi^2-\varphi}\,. \qquad (3.49)
\end{aligned}$$

Substituting (3.48) and (3.49) into (3.47) yields

$$\begin{aligned}
&\int_{-\infty}^{\hat{\theta}} p_\Theta(\theta) p_R(x-\theta)\, d\theta \\
=&\begin{cases}
\frac{1}{2\sqrt{2}\sigma_\theta}\mathrm{erfc}\left(\psi + \frac{x-\hat{\theta}}{\sqrt{2}\sigma_r}\right)\cdot e^{\psi^2+\varphi}, & \hat{\theta}\le 0 \\
\frac{1}{2\sqrt{2}\sigma_\theta}\,(\mathrm{A}+\mathrm{B})\cdot e^{\psi^2} - \frac{1}{2\sqrt{2}\sigma_\theta}\mathrm{erfc}\left(\psi - \frac{x-\hat{\theta}}{\sqrt{2}\sigma_r}\right)\cdot e^{\psi^2-\varphi}, & \hat{\theta}>0\,,
\end{cases} \qquad (3.50)
\end{aligned}$$

and, by dividing for the expression in (3.46), the posterior cumulative distribution function (cdf) follows:

$$P_{\Theta|X}(\hat{\theta}|x) = \begin{cases}
\frac{\exp(\varphi)\cdot\mathrm{erfc}\left(\psi+\frac{x-\hat{\theta}}{\sqrt{2}\sigma_r}\right)}{\mathrm{A+B}}, & \hat{\theta}\le 0 \\
1 - \frac{\exp(-\varphi)\cdot\mathrm{erfc}\left(\psi-\frac{x-\hat{\theta}}{\sqrt{2}\sigma_r}\right)}{\mathrm{A+B}}, & \hat{\theta}>0\,.
\end{cases} \qquad (3.51)$$

The MMAE estimator in (3.36) is obtained by numerically solving $P_{\Theta|X}(\hat{\theta}|x) = 0.5$.

3.5.2 MIX–G model: derivation of MMSE estimator

To evaluate the MMSE estimator, the numerator and the denominator in equation (3.7) are needed. According to the MIX–G model, the quantity $p_X(x)$ appearing at the denominator is given by

$$p_X(x) = \int_{-\infty}^{+\infty} \left[\alpha\frac{1}{\sqrt{2}\sigma_\theta}\exp\left(-\frac{\sqrt{2}|\theta|}{\sigma_\theta}\right) + (1-\alpha)\frac{1}{\sqrt{2\pi}\sigma_\theta}\exp\left(-\frac{\theta^2}{2{\sigma_\theta}^2}\right)\right]$$

$$
\begin{aligned}
&\cdot \frac{1}{\sqrt{2\pi}\sigma_r} \exp\left[-\frac{(x-\theta)^2}{2{\sigma_r}^2}\right] d\theta \\
=&\alpha \frac{1}{2\sqrt{2}\sigma_\theta} e^{\psi^2} (B+A) + (1-\alpha) \frac{1}{\sqrt{2\pi\,(\sigma_\theta^2+\sigma_r^2)}} \exp\left[-\frac{x^2}{2\,(\sigma_\theta^2+\sigma_r^2)}\right] \\
=&\alpha \frac{1}{2\sqrt{2}\sigma_\theta} e^{\psi^2} (B+A) + (1-\alpha)\mathrm{C}\,. \qquad (3.52)
\end{aligned}
$$

Since, in general, we have

$$
\int_{-\infty}^{\infty} \theta p_\Theta(\theta) p_R(x-\theta)\, d\theta = p_X(x)\ \hat{\theta}^{\mathrm{MMSE}}\,, \qquad (3.53)
$$

the numerator in (3.7) is given by

$$
\begin{aligned}
&\int_{-\infty}^{\infty} \theta p_\Theta(\theta) p_R(x-\theta)\, d\theta \\
=&\int_{-\infty}^{+\infty} \theta \left[\alpha \frac{1}{\sqrt{2}\sigma_\theta} \exp\left(-\frac{\sqrt{2}|\theta|}{\sigma_\theta}\right) + (1-\alpha)\,\frac{1}{\sqrt{2\pi}\sigma_\theta} \exp\left(-\frac{\theta^2}{2{\sigma_\theta}^2}\right)\right] \\
&\cdot \frac{1}{\sqrt{2\pi}\sigma_r} \exp\left[-\frac{(x-\theta)^2}{2{\sigma_r}^2}\right] d\theta \\
=&\alpha \left[\int_{-\infty}^{\infty} \theta\ p_\Theta(\theta) p_R(x-\theta)\, d\theta\right]_{\text{L–G model}} \\
&+ (1-\alpha) \left[\int_{-\infty}^{\infty} \theta\ p_\Theta(\theta) p_R(x-\theta)\, d\theta\right]_{\text{G–G model}} \\
=&\alpha \left[p_X(x)\hat{\theta}^{\mathrm{MMSE}}\right]_{\text{L–G model}} + (1-\alpha) \left[p_X(x)\hat{\theta}^{\mathrm{MMSE}}\right]_{\text{G–G model}}\,. \qquad (3.54)
\end{aligned}
$$

A zero-mean Gaussian function with variance $\sigma_\theta^2 + \sigma_r^2$ and the estimator (3.30) must be substituted for the G-G model, whereas the expression in (3.43) and the estimator in (3.35) must be substituted for the L–G model. Hence, the above expression becomes

$$
\begin{aligned}
\int_{-\infty}^{\infty} \theta\ p_\Theta(\theta) p_R(x-\theta)\, d\theta =&\alpha \frac{1}{2\sqrt{2}\sigma_\theta} e^{\psi^2} \left[(x-\rho)\mathrm{A} + (x+\rho)\mathrm{B}\right] \\
&+ (1-\alpha) \frac{x}{1+\psi} \frac{1}{\sqrt{2\pi\,(\sigma_\theta^2+\sigma_r^2)}} \exp\left[-\frac{x^2}{2\,(\sigma_\theta^2+\sigma_r^2)}\right] \\
=&\alpha \frac{1}{2\sqrt{2}\sigma_\theta} e^{\psi^2} \left[(x-\rho)\mathrm{A} + (x+\rho)\mathrm{B}\right] + (1-\alpha)\cdot \mathrm{DC}\,. \\
& \qquad (3.55)
\end{aligned}
$$

The ratio between (3.55) and (3.52) yields the MMSE estimator, that is

$$\hat{\theta}^{\text{MMSE}} = \frac{\alpha \exp(\psi^2)\left[(x-\rho)\,\text{A} + (x+\rho)\,\text{B}\right] + (1-\alpha)\,2\sqrt{2}\sigma_\theta \cdot \text{DC}}{\alpha \exp(\psi^2)\,(\text{A}+\text{B}) + (1-\alpha)\,2\sqrt{2}\sigma_\theta \text{C}}\,, \quad (3.56)$$

which coincides with (3.39).

3.5.3 MIX–G model: derivation of MMAE estimator

The quantity appearing at the denominator in the estimator given in (3.9) has been computed in (3.52). The expression at the numerator can be computed as follows. In general, it is given that

$$\int_{-\infty}^{\hat{\theta}} p_\Theta(\theta) p_R(x-\theta)\,d\theta = p_X(x)\; P_{\Theta|X}(\hat{\theta}|x)\,, \quad (3.57)$$

where $P_{\Theta|X}(\hat{\theta}|x)$ is the posterior cdf computed in $\hat{\theta}$. Hence, it follows

$$\begin{aligned}
&\int_{-\infty}^{\hat{\theta}} p_\Theta(\theta) p_R(x-\theta)\,d\theta \\
&= \alpha \int_{-\infty}^{\hat{\theta}} \frac{1}{\sqrt{2}\sigma_\theta} \exp\left(-\frac{\sqrt{2}|\theta|}{\sigma_\theta}\right) \frac{1}{\sqrt{2\pi}\sigma_r} \exp\left[-\frac{(x-\theta)^2}{2{\sigma_r}^2}\right] d\theta \\
&+ (1-\alpha) \int_{-\infty}^{\hat{\theta}} \frac{1}{\sqrt{2\pi}\sigma_\theta} \exp\left(-\frac{\theta^2}{2{\sigma_\theta}^2}\right) \frac{1}{\sqrt{2\pi}\sigma_r} \exp\left[-\frac{(x-\theta)^2}{2{\sigma_r}^2}\right] d\theta \\
&= \alpha \left[\int_{-\infty}^{\hat{\theta}} p_\Theta(\theta) p_R(x-\theta)\,d\theta\right]_{\text{L–G model}} + (1-\alpha) \left[\int_{-\infty}^{\hat{\theta}} p_\Theta(\theta) p_R(x-\theta)\,d\theta\right]_{\text{G–G model}} \\
&= \alpha \left[p_X(x) P_{\Theta|X}(\hat{\theta}|x)\right]_{\text{L–G model}} + (1-\alpha) \left[p_X(x) P_{\Theta|X}(\hat{\theta}|g)\right]_{\text{G–G model}}\,, \quad (3.58)
\end{aligned}$$

where $P_{\Theta|X}(\hat{\theta}|g)$ denotes the posterior cdf, computed in $\hat{\theta}$, relative to the indicated model.

The first term is given by the product of the expressions in (3.46) and in (3.51), and eventually can be written as

$$\alpha \left[p_X(x) P_{\Theta|X}(\hat{\theta}|x)\right]_{\text{G–G model}} = \frac{\alpha}{2\sqrt{2}\sigma_\theta} e^{\psi^2} \text{F}(\hat{\theta})\,, \quad (3.59)$$

where the function F has been defined in (3.29).

The second term in (3.58) involves a Gaussian pdf of the variable $x \sim \mathcal{N}(0, \sigma_\theta^2 + \sigma_r^2)$ and a Gaussian posterior cdf, i.e., $\theta|x \sim \mathcal{N}\left(\frac{x\sigma_\theta^2}{\sigma_\theta^2+\sigma_r^2}, \frac{\sigma_\theta^2\sigma_r^2}{\sigma_\theta^2+\sigma_r^2}\right)$.

Exploiting the property

$$\int_{-\infty}^{\theta_0} \frac{1}{\sqrt{2\pi}b} e^{-\frac{(t-a)^2}{2b^2}}\, dt = \frac{1}{2}\mathrm{erfc}\left(\frac{a-\theta_0}{\sqrt{2}b}\right), \qquad b>0\,, \tag{3.60}$$

and after some manipulation, we can achieve

$$\begin{aligned}(1-\alpha)\left[p_X(x)P_{\Theta|x}(\hat{\theta}|x)\right]_{\text{G–G model}} = \\ (1-\alpha)\frac{\mathrm{C}}{2}\mathrm{erfc}\left[\left(\mathrm{D}-\hat{\theta}\right)\left(\frac{\sqrt{1+\psi^2}}{\sqrt{2}\psi}\right)\right]\,.\end{aligned} \tag{3.61}$$

Combining (3.59) and (3.61), the following posterior cdf for the MIX-G model can be achieved:

$$\begin{aligned}P_{\Theta|X}(\hat{\theta}|x) = \\ \frac{\alpha\exp(\psi^2)\mathrm{F}(\hat{\theta}) + (1-\alpha)\sqrt{2}\sigma_\theta \mathrm{C}\,\mathrm{erfc}\left[\left(D-\hat{\theta}\right)\left(\frac{\sqrt{1+\psi^2}}{\sqrt{2}\psi}\right)\right]}{\alpha\exp(\psi^2)(\mathrm{A}+\mathrm{B}) + (1-\alpha)\,2\sqrt{2}\sigma_\theta \mathrm{C}}\,.\end{aligned} \tag{3.62}$$

The MMAE estimator in (3.40) is achieved by searching $\hat{\theta}$ such that $P_{\Theta|X}(\hat{\theta}|x) = 0.5$.

Chapter 4

Image formats for despeckling

As already pointed out in Section 3.1.3, the knowledge of the pdf of the speckle is fundamental in the formulation of despeckling filters based on Bayesian estimation that attempt to extract the noise-free reflectivity from a speckled observation [45, 11] as well as for other tasks, e.g., SAR imagery segmentation [46]. Such pdf is related to the format of the single-look image, that is, the original incoherent image; for instance, the amplitude format (AF) is obtained, according to (2.2), when the modulus of complex data is used; instead, the intensity format (IF) expressed in (2.3) is given by using the square modulus. In order to reduce the variance of speckle (at price of resolution degradation), the multilooking process can be adopted by averaging over L independent adjacent samples; if a IF single–look image is multilooked, then the intensity of the multi-look datum is distributed according to a (2.7), whereas its square root is distributed according to a Nakagami distribution [22]. If an AF single-look image is multilooked, the pdf of the speckle can not be expressed in a closed form, even though its moment can be computed.

The introduction of despeckling methods using Bayesian estimation in the UDWT domain has somehow "shifted" the problem of statistical characterization from the space domain to the UDWT domain. Such methods have been proposed, for instance, in [37, 35, 47, 36, 41, 48, 2, 49] for the case of SAR data and in [50, 51, 52, 53, 54] for the case of ultrasound and sonar data. Although the above methods are based on different models of the wavelet coefficients, a common feature is that they consider only IF images. However, the pdf modeling of the wavelet coefficients is very often *conjectured a-priori* and it is not directly related to the actual distribution of the speckle, i.e., on the format of the SAR image. For example, in [36] wavelet coefficients are modelled by a very flexible generalized Gaussian model, requiring only the knowledge of the moments of the involved variables. To the best of our

knowledge, there is no study in the literature assessing whether it is more convenient to filter wavelet coefficients of intensity or amplitude images.

In this chapter, the problem of despeckling SAR images when the input data is either an intensity or an amplitude signal is revisited. State-of-the-art despeckling methods based on Bayesian estimators in the UDWT domain, presented in 4.0 3, are taken into consideration. First, how these methods proposed for one format (e.g., intensity) can be adapted to the other format (e.g., amplitude) is investigated. Second, the performance of such algorithms in both cases is analyzed. Experimental results carried out on simulated speckled images and on true SAR data are presented and discussed in order to assess the best strategy. From these results, it can be observed that filtering in the amplitude domain yields better performances in terms of objective quality indexes, such as preservation of structural details, as well as in terms of visual inspection of the filtered SAR data.

4.1 Unique formulation of Bayesian despeckling in the UDWT domain

4.1.1 Image formats

For sake of simplicity, we recall the multiplicative model (2.13) given in Section 2.2

$$g(n) = f(n)u(n)$$

In this expression, $f(n)$ and $g(n)$ are the noise-free reflectivity and the observed signal at the position n, respectively. They can be in either amplitude or intensity format. The random variable $u(n)$ represents the fully developed speckle noise. We assume that $u(n)$ is unit-mean, uncorrelated and independent from $f(n)$ [55, 18, 17]. An equivalent additive model, as in (2.14), can be straightforwardly derived.

$$\begin{aligned} g(n) &= f(n) + f(n) \cdot (u(n) - 1) = f(n) + f(n) \cdot u'(n) \\ &= f(n) + v(n). \end{aligned} \tag{4.1}$$

The mean of $u'(n) = u(n) - 1$ is zero and its pdf is directly derived from that of $u(n)$. The term $v(n)$ is signal-dependent and accounts for speckle disturbance.

The pdf of the speckle process u depends on the specific format of the signal [22]. For IF single-look images the pdf of u is exponential, whereas for

multi-look images the pdf of u becomes a $\Gamma(L, L)$, given by

$$p_U(u) = \frac{L^L}{\Gamma(L)} u^{L-1} e^{-uL}. \tag{4.2}$$

For AF single-look images the pdf of u is a unit mean Rayleigh pdf, given by

$$p_U(u) = \frac{\pi u}{2} e^{-\frac{\pi u^2}{4}} \tag{4.3}$$

whereas for AF multi-look images u is distributed according to the average of L independent unit mean Rayleigh variables and its pdf can not be expressed in a closed form.

Sometimes, it is convenient to consider also the squared root of an IF (SIF) image, which can be considered as an alternative amplitude format. In this case, for a SIF single-look image u is Rayleigh distributed with mean equal to $\sqrt{\pi}/2$, whereas for SIF multi-look images the pdf of u is a Nakagami pdf given by

$$p_U(u) = \frac{2L^L}{\Gamma(L)} u^{2L-1} e^{-u^2 L}. \tag{4.4}$$

For SIF images the mean of u is different from one, however the model in (2.13) is still valid if we rescale the square root of the intensity by a factor $\mu_{\mathrm{SIF}}(L) = L^{-\frac{1}{2}}\Gamma(L)/\Gamma(L + \frac{1}{2})$. It is worth noting that single-look AF and rescaled SIF images have identical distribution, whereas multi-look AF and rescaled SIF images have different distributions and must be considered different formats. In the following, with SIF images we will always refer to rescaled SIF images.

As to the knowledge about u in (4.1), it will be shown that to achieve the solution of the despeckling problem only the moments of u are necessary. In the following, some despeckling methods are reviewed and the necessary information that is needed to achieve the solution is provided for the IF, AF, and SIF signals.

As to the knowledge about u in (2.13), it will be shown that to achieve the solution of the despeckling problem only the moments of u are necessary.

4.1.2 Generalizing Bayesian filters as function of moments

In the last decade, several despeckling methods based on Bayesian estimation in the DWT or in the undecimated DWT domain have been proposed. The methods differ each other for the choice of the estimation criterion used

to achieve the despeckled coefficients and for the modelling of the data in the wavelet domain.

Bayesian estimation requires the knowledge of the pdfs of the wavelet coefficients relative to the signal of interest (the reflectivity), also referred to as *prior* pdf, and to the noise component.

In the following list, some of the despeckling methods already presented in Section 3.2 and Section 3.3 are reviewed and their dependency upon the moments of wavelet coefficients is highlighted.

- **LMMSE filter**: the moments of the second order of both noise-free and noise component wavelet coefficients appear directly in (3.30).

- **MAP GG filter**: the scale and shape factors of both the noise-free (η_{W_f}, ν_{W_f}) and noise component (η_{W_v}, ν_{W_v}) wavelet coefficients appear in (3.31); the shape factors can be estimated by inverting the following relation [36]:
$$\frac{E\left[X^2\right]}{\sqrt{E\left[X^4\right]}} = \frac{\Gamma(3/\nu_X)}{\sqrt{\Gamma(1/\nu_X)\Gamma(5/\nu_X)}} \tag{4.5}$$
where X is either $W_f(n)$ or $W_v(n)$; then the related scale factors are obtained by means of (3.17). Thus MAP GG filter requires the knowledge of the second and the fourth order moments of both noise-free and noise component wavelet coefficients.

- **GG MAP-S filter**: same as MAP GG filter, since (3.31) is still valid, provided that the correct expression of σ_u is used in the computation of the variance of the texture component [41].

- **MAP LG filter**: the moments of the second order of both noise-free and noise component wavelet coefficients appear in (3.34)

- **LG MAP-S filter**: same as MAP LG filter or LMMSE filter (see Section 3.3.2).

Interestingly, all of the above solutions are based on the knowledge of some moments of either $W_f(n)$ or $W_v(n)$. In general, such moments can be expressed as a function of the moments of the observed variables $g(n)$ and $W_g(n)$, the equivalent filter $h(n)$, and the moments of the speckle variables u and u'. Several expressions have been proposed in the literature. We report

the exact expression derived in [41]:

$$E\left[W_v^2(n)\right] = \frac{\mu_{u'}^{[2]}}{\mu_u^{[2]}} E\left[M_g^{[2]}(n)\right] \tag{4.6}$$

$$E\left[W_f^2(n)\right] = E\left[W_g^2(n) + \left(\frac{1}{\mu_u^{[2]}} - 1\right) M_g^{[2]}(n)\right] \tag{4.7}$$

$$\begin{aligned} E\left[W_v^4(n)\right] = E\Bigg[& 3\left(\frac{\mu_{u'}^{[2]}}{\mu_u^{[2]}}\right)^2 \left(M_g^{[2]}(n)\right)^2 \\ & + \left(\frac{\mu_{u'}^{[4]}}{\mu_u^{[4]}} - 3\left(\frac{\mu_{u'}^{[2]}}{\mu_u^{[2]}}\right)^2\right) M_g^{[4]}(n)\Bigg] \end{aligned} \tag{4.8}$$

$$\begin{aligned} E[W_f^4(n)] = E\Bigg[& W_g^4(n) + \left(\frac{6}{\mu_u^{[2]}} - 6\right) W_g^2(n) M_g^{[2]}(n) \\ & + \left(\frac{3}{\left(\mu_u^{[2]}\right)^2} - \frac{6}{\mu_u^{[2]}} + 3\right) \left(M_g^{[2]}(n)\right)^2 \\ & + \left(\frac{4}{\mu_u^{[3]}} - \frac{12}{\mu_u^{[2]}} + 8\right) W_g(n) M_g^{[3]}(n) \\ & + \left(\frac{1}{\mu_u^{[4]}} - \frac{4}{\mu_u^{[3]}} - \frac{3}{\left(\mu_u^{[2]}\right)^2} + \frac{12}{\mu_u^{[2]}} - 6\right) M_g^{[4]}(n)\Bigg] \end{aligned} \tag{4.9}$$

where we define $\mu_u^{[k]} = E[u^k]$ and $M_g^{[k]}(n) = \sum_i h^k(i) g^k(n-i)$. In practice, the moments of the observed variables can be estimated using local averages, whereas the moments of u and u' can be computed according to the number of look L and the image format, as specified in the following.

The solutions derived so far are not based on a specific image format. As long as the input signal obeys the model in (2.13), the filters defined by (3.8), (3.31) and (3.34), based on the moments given in (4.6)-(4.9), can be applied to IF, AF, or rescaled SIF images, provided that the correct moments of the speckle variables are use. Hence they represent a unique formulation of Bayesian filters in the UDWT domain. Such conclusions are still valid for the remaining filters presented in Section 3.2 and every Bayesian filter in the UDWT domain, provided that the expressions of the moments in the transformed domain are given.

4.1.3 Moments of speckle noise variables

In order to use the relations (4.6)-(4.9) for filtering, the quantities $\mu_u^{[k]}$, $k = 1, 2, 3, 4$, are required. In the following, we will derive the expression of the moments of u according to the number of look L and the image format. As to the moments of u', they can be easily derived from the moments of u as follows:

$$\begin{aligned}
\mu_{u'}^{[1]} &= 0 \\
\mu_{u'}^{[2]} &= \mu_u^{[2]} - 1 \\
\mu_{u'}^{[3]} &= \mu_u^{[3]} - 3\mu_u^{[2]} + 2 \\
\mu_{u'}^{[4]} &= \mu_u^{[4]} - 4\mu_u^{[3]} + 6\mu_u^{[2]} - 3
\end{aligned}$$

Intensity

When u is distributed according to (4.2), its moments can be expressed as [56]

$$\mu_u^{[m]}(L) = \frac{\Gamma(L+m)}{\Gamma(L)} \frac{1}{L^m}. \tag{4.10}$$

Amplitude

In the case of single-look AF signals, u has a Rayleigh pdf given by (4.3) and its moments can be expressed as

$$\mu_u^{[m]}(1) = \left(\frac{4}{\pi}\right)^{\frac{m}{2}} \Gamma\left(1 + \frac{m}{2}\right). \tag{4.11}$$

When u is the average of L i.i.d. variables distributed according to (4.3), it can be shown (see Section 4.4.1) that its moments can be expressed by

$$\mu_u^{[1]}(L) = 1 \tag{4.12}$$

$$\mu_u^{[2]}(L) = \frac{1}{\pi L}[4 + \pi(L-1)] \tag{4.13}$$

$$\mu_u^{[3]}(L) = \frac{1}{\pi L^2}[6 + 12(L-1) + \pi(L-2)(L-1)] \tag{4.14}$$

$$\begin{aligned}
\mu_u^{[4]}(L) = &\frac{1}{\pi^2 L^3}\big[32 + 48(L-1) + 24\pi(L-1)^2 \\
&+ \pi^2(L-3)(L-2)(L-1)\big]
\end{aligned} \tag{4.15}$$

Square Root of Intensity

If we denote as $\tilde{u}$ the square root of an intensity speckle process, distributed as (4.4), its moments are given by [22]

$$\mu_{\tilde{u}}^{[m]}(L) = \frac{\Gamma\left(L+\frac{m}{2}\right)}{\Gamma(L)}\frac{1}{L^{\frac{m}{2}}}. \tag{4.16}$$

Hence, the moments of u for a rescaled SIF signal can be obtained as

$$\mu_{u}^{[m]}(L) = \frac{\mu_{\tilde{u}}^{[m]}(L)}{\left(\mu_{\tilde{u}}^{[1]}(L)\right)^m} = \frac{\Gamma(L)^{m-1}\Gamma\left(L+\frac{m}{2}\right)}{\Gamma\left(L+\frac{1}{2}\right)^m}. \tag{4.17}$$

4.2 Experimental Results

The performances of the different filters on different image formats have been assessed on both simulated images and true SAR images. As to simulated images, the performances are measured by computing the PSNR and the mean structural similarity index (MSSIM) between the original and the filtered images. For sake of convenience, the PSNR, already defined in Section 3.2.5, is redefined as

$$\mathrm{PSNR} = 10\log_{10}\left(\frac{I_{peak}^2}{E[(\hat{I}-I)^2]}\right) \tag{4.18}$$

where I is the original image, $\hat{I}$ is the filtered image, and I_{peak} is the peak value (for 8-bit images, we assume $I_{peak} = 255$). The PSNR, as well as closely related metrics like the mean square error between the original and the filtered images, have been often used to assess the performance of despeckling applications [36, 57]. The MSSIM is a measure of degradation of structural information and it is defined as [58]

$$\mathrm{MSSIM} = E\left[\frac{(2\mu_I\mu_{\hat{I}}+C_1)(2\sigma_{I\hat{I}}+C_2)}{(\mu_I^2+\mu_{\hat{I}}^2+C_1)(\sigma_I^2+\sigma_{\hat{I}}^2+C_2)}\right] \tag{4.19}$$

where μ_I, σ_I^2, $\mu_{\hat{I}}$, $\sigma_{\hat{I}}^2$, and $\sigma_{I\hat{I}}$ are the local mean, variance, and covariance of the original and filtered images, whereas C_1 and C_2 are two suitable constants. Since we want to avoid the comparison to be biased by the the format in which the measures are taken, we consider both I and $\hat{I}$ in the amplitude

format; that is, for IF we use $I = \sqrt{f}$ and $\hat{I} = \sqrt{\hat{f}}$, while for both SIF and AF we use $I = f$ and $\hat{I} = \hat{f}$.

Moreover, as a no-reference index of the quality of the filtered images, we report the sample mean and the sample variance of the ratio between the observed and the filtered images, $\hat{u} = g/\hat{f}$. For a good despeckling filter, $\hat{u}$ should be as close as possible to the speckle process u and we should obtain $\mu_{\hat{u}} = 1$ and $\sigma^2_{\hat{u}} = \sigma^2_u$. In the case of IF and SIF images, the statistics have been evaluated on intensity values and we have $\sigma^2_u = 1/L$. In the case of AF images, the statistics have been evaluated on amplitude values and we have $\sigma^2_u = (4-\pi)/(\pi L)$. For a better evaluation of the estimated values, in all the following tables the normalized values $\sigma^2_u \cdot L$ or $\sigma^2_u \cdot (\pi L)/(4-\pi)$ are reported. Since there is no need of using the original image as a reference, the above indexes can be used for both simulated and true SAR images.

For all tested filters, the biorthogonal 9/7 wavelets [59] have been used, with a four level decomposition.

4.2.1 Simulated Images

We considered three 8-bit 512×512 optical images, *Lena*, *Barbara*, and *San Francisco*, corrupted by synthetic speckle generated according to the models in (4.2)-(4.4) considering different number of look L. The original images are shown in Figure 4.1. In Tables 4.1–4.3, we report the results obtained in the case of IF and SIF images, whereas in Tables 4.4–4.6 we report the results obtained in the case of AF images.

(a) (b) (c)

Figure 4.1: *Original images: (a)* Lena*; (b)* Barbara*; (c)* San Francisco.

The results clearly show that filtering SIF images outperforms filtering IF images. For each image and for each number of look, all filters yield a higher PSNR when operating in the SIF domain. For example, the MAP-GG filter gains about 0.6 dB in PSNR for the single-look *Lena* and *Barbara* images and about 0.9 dB in PSNR for the single-look *San Francisco* image. As to the MSSIM, in the case of the *Lena* image we have very similar values for both

Table 4.1: *Results for despeckling of simulated image* Lena*, obtained on different number of looks by means of various filter, in the case of IF and SIF.*

L	filter	PSNR		MSSIM		$\mu_{\hat{u}}$		$\sigma^2_{\hat{u}} \cdot L$	
		IF	SIF	IF	SIF	IF	SIF	IF	SIF
1	noisy	11.30		0.109		-		-	
	LMMSE	24.55	24.69	0.513	0.524	0.90	0.89	0.639	0.619
	MAP GG	26.32	26.90	0.736	0.735	0.98	0.98	0.998	0.938
	GG MAP-S	26.33	26.87	0.736	0.734	0.98	0.98	0.999	0.937
	MAP LG	26.16	26.67	0.725	0.718	0.95	0.96	0.874	0.875
	LG MAP-S	26.17	26.66	0.725	0.718	0.95	0.96	0.874	0.874
2	noisy	14.46		0.175		-		-	
	LMMSE	26.65	26.95	0.630	0.635	0.93	0.94	0.666	0.661
	MAP GG	28.03	28.74	0.785	0.787	0.99	0.98	1.037	0.935
	GG MAP-S	28.06	28.71	0.785	0.786	0.99	0.98	1.014	0.933
	MAP LG	27.82	28.48	0.775	0.772	0.97	0.97	0.885	0.887
	LG MAP-S	27.86	28.50	0.775	0.772	0.97	0.97	0.888	0.886
4	noisy	17.55		0.258		-		-	
	LMMSE	28.53	28.98	0.720	0.725	0.96	0.96	0.678	0.683
	MAP GG	29.64	30.34	0.824	0.824	0.99	0.99	1.085	0.938
	GG MAP-S	29.71	30.32	0.825	0.824	0.99	0.99	1.041	0.933
	MAP LG	29.38	30.10	0.814	0.815	0.97	0.98	0.899	0.901
	LG MAP-S	29.50	30.19	0.816	0.817	0.98	0.98	0.914	0.895
16	noisy	23.68		0.468		-		-	
	LMMSE	32.55	32.95	0.850	0.852	0.98	0.99	0.672	0.668
	MAP GG	33.13	33.70	0.883	0.886	1.00	0.99	1.066	0.917
	GG MAP-S	33.16	33.64	0.881	0.884	1.00	0.99	1.021	0.892
	MAP LG	32.89	33.52	0.880	0.883	0.99	0.99	0.926	0.894
	LG MAP-S	33.18	33.66	0.882	0.883	0.99	0.99	0.989	0.869

Table 4.2: *Results for despeckling of simulated image* Barbara*, obtained on different number of looks by means of various filter, in the case of IF and SIF.*

L	filter	PSNR		MSSIM		$\mu_{\hat{u}}$		$\sigma^2_{\hat{u}} \cdot L$	
		IF	SIF	IF	SIF	IF	SIF	IF	SIF
1	noisy	11.52		0.181		-		-	
	LMMSE	22.61	22.85	0.518	0.548	0.88	0.88	0.633	0.593
	MAP GG	22.89	23.51	0.606	0.640	0.98	0.97	1.198	0.969
	GG MAP-S	23.05	23.70	0.617	0.653	0.98	0.97	1.190	0.953
	MAP LG	22.89	23.44	0.603	0.631	0.94	0.96	0.903	0.883
	LG MAP-S	23.00	23.59	0.610	0.640	0.94	0.95	0.897	0.874
2	noisy	14.68		0.280		-		-	
	LMMSE	24.33	24.68	0.634	0.657	0.92	0.92	0.636	0.624
	MAP GG	24.42	25.11	0.691	0.720	0.98	0.97	1.220	0.929
	GG MAP-S	24.79	25.38	0.707	0.734	0.98	0.97	1.172	0.909
	MAP LG	24.17	24.89	0.680	0.709	0.95	0.96	0.883	0.879
	LG MAP-S	24.56	25.18	0.696	0.722	0.95	0.96	0.870	0.863
4	noisy	17.80		0.397		-		-	
	LMMSE	26.17	26.56	0.737	0.754	0.94	0.95	0.637	0.630
	MAP GG	26.31	26.92	0.777	0.794	0.99	0.98	1.215	0.897
	GG MAP-S	26.64	27.18	0.792	0.806	0.99	0.98	1.321	0.872
	MAP LG	25.86	26.59	0.762	0.783	0.96	0.97	0.878	0.868
	LG MAP-S	26.30	26.96	0.780	0.797	0.97	0.97	0.941	0.844
16	noisy	23.93		0.630		-		-	
	LMMSE	30.21	30.55	0.873	0.878	0.98	0.98	0.610	0.581
	MAP GG	30.35	30.86	0.886	0.892	0.99	0.99	1.052	0.826
	GG MAP-S	30.30	30.84	0.890	0.895	1.00	0.99	1.149	0.778
	MAP LG	29.93	30.55	0.879	0.887	0.98	0.99	0.879	0.819
	LG MAP-S	30.35	30.84	0.888	0.893	0.99	0.99	0.955	0.765

Table 4.3: *Results for despeckling of simulated image* San Francisco, *obtained on different number of looks by means of various filter, in the case of IF and SIF.*

L	filter	PSNR		MSSIM		$\mu_{\hat{u}}$		$\sigma^2_{\hat{u}} \cdot L$	
		IF	SIF	IF	SIF	IF	SIF	IF	SIF
1	noisy	15.23		0.194		-		-	
	LMMSE	23.94	24.58	0.573	0.588	0.88	0.88	0.655	0.620
	MAP GG	23.99	24.90	0.623	0.646	0.98	0.98	1.184	1.009
	GG MAP-S	24.03	24.89	0.624	0.646	0.98	0.98	1.128	1.002
	MAP LG	24.00	24.87	0.624	0.645	0.94	0.96	0.919	0.917
	LG MAP-S	24.03	24.89	0.624	0.645	0.94	0.96	0.919	0.915
2	noisy	18.42		0.303		-		-	
	LMMSE	25.47	26.23	0.658	0.675	0.92	0.92	0.668	0.647
	MAP GG	25.27	26.28	0.672	0.695	0.99	0.98	1.379	0.983
	GG MAP-S	25.35	26.28	0.674	0.695	0.99	0.98	1.517	0.972
	MAP LG	25.27	26.25	0.674	0.695	0.95	0.97	0.921	0.915
	LG MAP-S	25.39	26.34	0.677	0.697	0.96	0.97	0.961	0.908
4	noisy	21.53		0.435		-		-	
	LMMSE	27.07	27.84	0.727	0.741	0.94	0.95	0.673	0.646
	MAP GG	26.71	27.73	0.719	0.738	1.00	0.99	2.226	0.972
	GG MAP-S	26.88	27.79	0.722	0.739	1.00	0.98	1.652	0.947
	MAP LG	26.67	27.70	0.721	0.740	0.96	0.98	0.955	0.923
	LG MAP-S	26.92	27.86	0.726	0.743	0.98	0.98	1.446	0.901
16	noisy	27.66		0.716		-		-	
	LMMSE	30.80	31.36	0.840	0.846	0.97	0.98	0.611	0.544
	MAP GG	30.39	31.10	0.813	0.822	1.00	0.99	1.633	0.884
	GG MAP-S	30.35	30.86	0.813	0.822	1.00	0.99	1.102	0.762
	MAP LG	30.24	31.12	0.818	0.827	0.98	0.99	1.039	0.868
	LG MAP-S	30.69	31.22	0.824	0.830	0.99	0.99	1.197	0.772

Table 4.4: *Results for despeckling of simulated image* Lena*, obtained on different number of looks by means of various filter, in the case of AF.*

L	filter	PSNR	MSSIM	$\mu_{\hat{u}}$	$\sigma^2_{\hat{u}} \cdot \frac{\pi L}{4-\pi}$
1	noisy	11.27	0.109	-	-
	LMMSE	24.67	0.520	0.97	0.744
	MAP GG	26.92	0.736	0.99	0.969
	GG MAP-S	26.88	0.735	0.99	0.968
	MAP LG	26.68	0.717	0.99	0.937
	LG MAP-S	26.67	0.717	0.99	0.936
2	noisy	14.29	0.170	-	-
	LMMSE	26.79	0.628	0.98	0.739
	MAP GG	28.55	0.781	0.99	0.957
	GG MAP-S	28.52	0.781	0.99	0.955
	MAP LG	28.30	0.766	0.99	0.928
	LG MAP-S	28.31	0.767	0.99	0.927
4	noisy	17.31	0.252	-	-
	LMMSE	28.89	0.722	0.99	0.728
	MAP GG	30.29	0.825	1.00	0.949
	GG MAP-S	30.25	0.824	0.99	0.945
	MAP LG	30.04	0.815	0.99	0.924
	LG MAP-S	30.12	0.816	0.99	0.919
16	noisy	23.31	0.455	-	-
	LMMSE	32.74	0.847	1.00	0.684
	MAP GG	33.52	0.883	1.00	0.926
	GG MAP-S	33.46	0.881	1.00	0.902
	MAP LG	33.35	0.880	1.00	0.908
	LG MAP-S	33.49	0.880	1.00	0.882

Table 4.5: *Results for despeckling of simulated image* Barbara, *obtained on different number of looks by means of various filter, in the case of AF.*

L	filter	PSNR	MSSIM	$\mu_{\hat{u}}$	$\sigma^2_{\hat{u}} \cdot \frac{\pi L}{4-\pi}$
1	noisy	11.54	0.180	-	-
	LMMSE	22.83	0.548	0.96	0.722
	MAP GG	23.50	0.641	0.99	0.980
	GG MAP-S	23.68	0.653	0.99	0.969
	MAP LG	23.40	0.632	0.98	0.939
	LG MAP-S	23.56	0.641	0.98	0.933
2	noisy	14.54	0.276	-	-
	LMMSE	24.65	0.659	0.97	0.708
	MAP GG	25.06	0.720	0.99	0.955
	GG MAP-S	25.36	0.734	0.99	0.938
	MAP LG	24.83	0.708	0.98	0.926
	LG MAP-S	25.15	0.722	0.98	0.912
4	noisy	17.55	0.388	-	-
	LMMSE	26.44	0.746	0.98	0.685
	MAP GG	26.77	0.788	0.99	0.929
	GG MAP-S	27.04	0.801	0.99	0.904
	MAP LG	26.45	0.777	0.99	0.911
	LG MAP-S	26.81	0.791	0.99	0.885
16	noisy	23.57	0.617	-	-
	LMMSE	30.32	0.873	0.99	0.602
	MAP GG	30.65	0.888	1.00	0.842
	GG MAP-S	30.63	0.892	1.00	0.795
	MAP LG	30.32	0.883	0.99	0.841
	LG MAP-S	30.62	0.890	1.00	0.784

Table 4.6: *Results for despeckling of simulated image* San Francisco, *obtained on different number of looks by means of various filter, in the case of AF.*

L	filter	PSNR	MSSIM	$\mu_{\hat{u}}$	$\sigma^2_{\hat{u}} \cdot \frac{\pi L}{4-\pi}$
1	noisy	15.23	0.194	-	-
	LMMSE	24.67	0.594	0.96	0.740
	MAP GG	24.97	0.648	0.99	0.988
	GG MAP-S	24.98	0.648	0.99	0.985
	MAP LG	24.93	0.646	0.98	0.948
	LG MAP-S	24.96	0.647	0.98	0.947
2	noisy	18.26	0.297	-	-
	LMMSE	26.14	0.672	0.97	0.727
	MAP GG	26.19	0.692	0.99	0.991
	GG MAP-S	26.23	0.693	0.99	0.981
	MAP LG	26.15	0.692	0.99	0.953
	LG MAP-S	26.24	0.694	0.99	0.945
4	noisy	21.29	0.426	-	-
	LMMSE	27.77	0.739	0.98	0.700
	MAP GG	27.66	0.736	0.99	0.986
	GG MAP-S	27.69	0.737	0.99	0.962
	MAP LG	27.63	0.738	0.99	0.953
	LG MAP-S	27.78	0.741	0.99	0.930
16	noisy	27.30	0.702	-	-
	LMMSE	31.13	0.841	0.99	0.578
	MAP GG	30.85	0.816	1.00	0.913
	GG MAP-S	30.68	0.818	1.00	0.801
	MAP LG	30.88	0.821	0.99	0.901
	LG MAP-S	31.00	0.825	1.00	0.808

formats, whereas in the case of the *Barbara* and *San Francisco* images, the MSSIM is slightly better for SIF, indicating that filtering the square root of intensity neither introduces artifacts nor alters structural information. The above results are also confirmed by inspecting the values of $\mu_{\hat{u}}$ and $\sigma^2_{\hat{u}}$ for the different filters: the values of $\mu_{\hat{u}}$ are always very similar for both formats, whereas the values of $\sigma^2_{\hat{u}}$, especially for the MAP-GG and MAP-GG-S filters, in the case of SIF tend to be closer to the theoretical variance of the speckle.

In the case of AF images, we can see that all filters obtain results very close to those obtained on SIF images. Also the values of the statistical parameters $\mu_{\hat{u}}$ and $\sigma^2_{\hat{u}}$ confirm a good performance of the filters for this kind of images, especially in the case of the MAP-GG filter, which yields a $\sigma^2_{\hat{u}}$ quite close to the theoretical value. It is interesting to note that the LMMSE filter exhibits a bias irrespective of the SAR image format, indicating that Gaussian modeling of wavelet coefficients is not adequate even in the case of amplitude and square root of intensity signals.

4.2.2 True SAR images

Results on true SAR data have been assessed by using two 16 bit 512×512 COSMO-SkyMed 1-look X-HH images showing the area near the airport of Florence, Italy. For showing results on intensity multilooked data, two corresponding 4-look 256×256 intensity images have been obtained by averaging four neighbouring pixels and downsampling the intensity of the 1–look images. Furthermore, by means of the same procedure, two corresponding 4-look 256×256 amplitude images have been obtained from the amplitude of the 1–look images. The 1-look COSMO-SkyMed images are shown in Figure 4.2.

The statistics $\mu_{\hat{u}}$ and $\sigma^2_{\hat{u}}$ of the extracted speckle in the three considered image formats and for all the considered filters have been evaluated on two different homogeneous areas, denoted as "A" and "B" in Figure 4.2.

The results for the IF and SIF domains, reported in Table 4.7, indicate that the despeckling performance of both approaches is very similar on areas affected by fully developed speckle. All filters, apart from the LMMSE one, are virtually unbiased irrespective of the image format. Also, the variance of the estimated speckle noise is quite close to the theoretical value, with no appreciable difference between IF and SIF. In Table 4.8, the results for the 4–look image in the AF domain are shown. It is interesting to note that the indexes are very similar to those obtained for the 4–look SIF case, except for the LMMSE filter where a reduction of bias is observed in the AF domain.

For visual inspection, we propose the images obtained by applying the MAP-GG-S filter in the IF and SIF domains for the 1-look case (Figure 4.3)

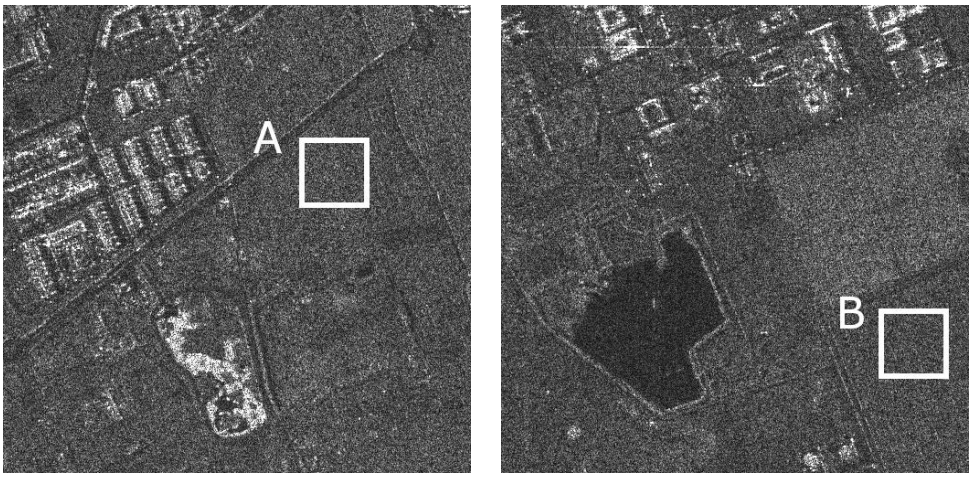

Figure 4.2: 1-*look COSMO-SkyMed images selected for the experiments; highlighted homogeneous zones are used to compute performance indexes.*

and for the 4-look case (Figure 4.4), as well as the images obtained by applying the same filter for the 4–look case in the AF domain (Figure 4.5). From all the examples, it is apparent that filtering SIF or AF images is usually beneficial. As to homogeneous areas, the smoothing degree obtained by the filter, as well as the artifacts produced by the wavelet synthesis stage, are similar for all the proposed formats. Conversely, it is particularly evident that filtering SIF or AF images yields a better preservation of details, since it produces less artifacts near edges, high variance regions, and targets. From the comparison of 4–look SIF and AF images we can observe no appreciable differences between the despeckled images obtained from the two formats.

4.3 Conclusions

In this chapter, we have presented a study on despeckling images affected by multiplicative noise in either amplitude or intensity format. Bayesian despeckling algorithms in the wavelet domain have been considered. We have shown that a common framework for the despeckling problem can be setup for various formats - satisfying the multiplicative model - based on the computation of the moments of the speckle component. Such moments are derived for single-look and multi-look images. In the latter case, amplitude multi-look images can be obtained either averaging amplitude signals or taking the square root of the average of intensity signals. The experimental results have been carried out on both synthetically speckled images and on true SAR COSMO-SkyMed images.

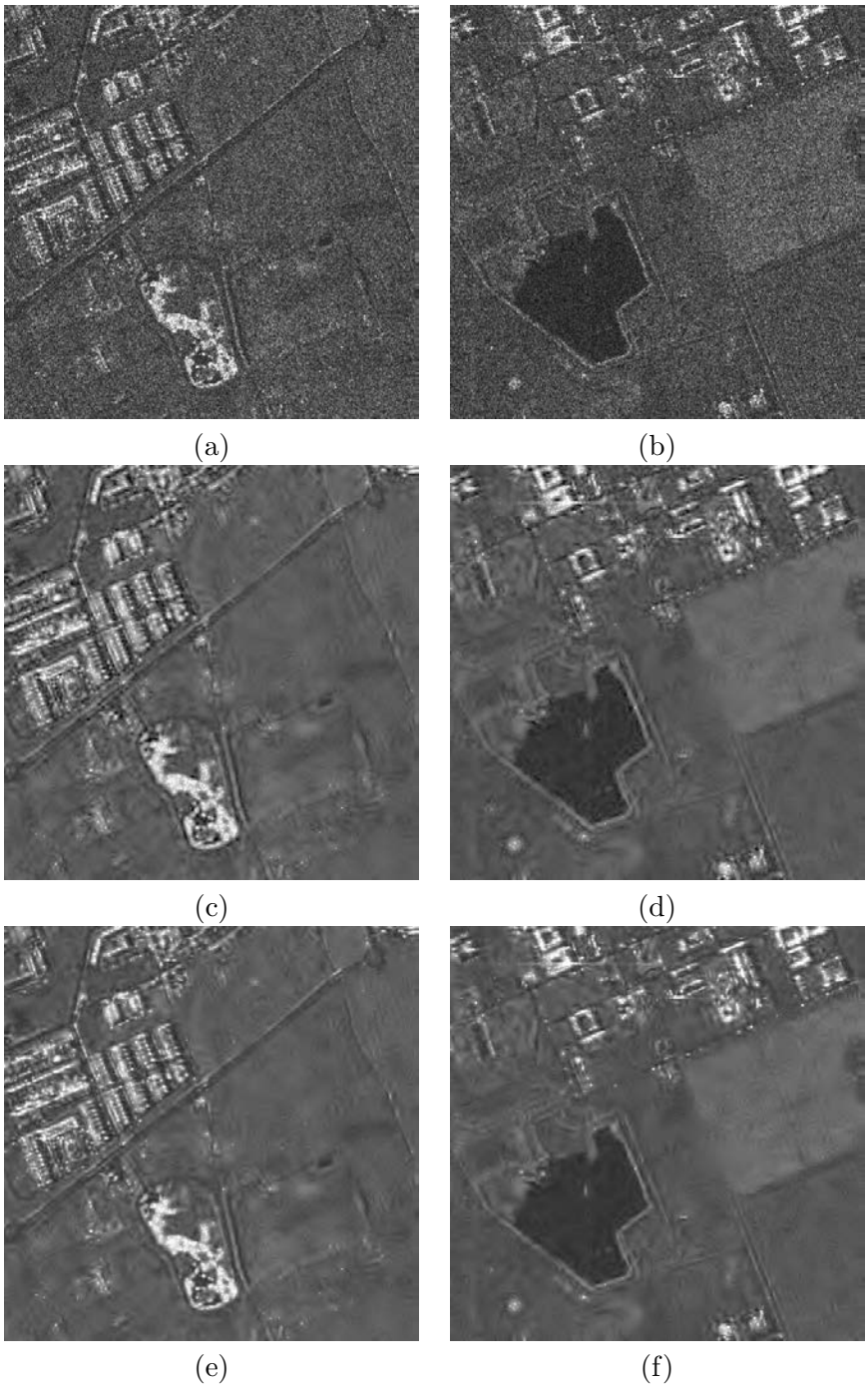

Figure 4.3: *Example of despeckling of the* 1*-look COSMO-SkyMed images: (a)-(b) original; (c)-(d) MAP-GG-S filtered, IF; (e)-(f) MAP-GG-S filtered, SIF.*

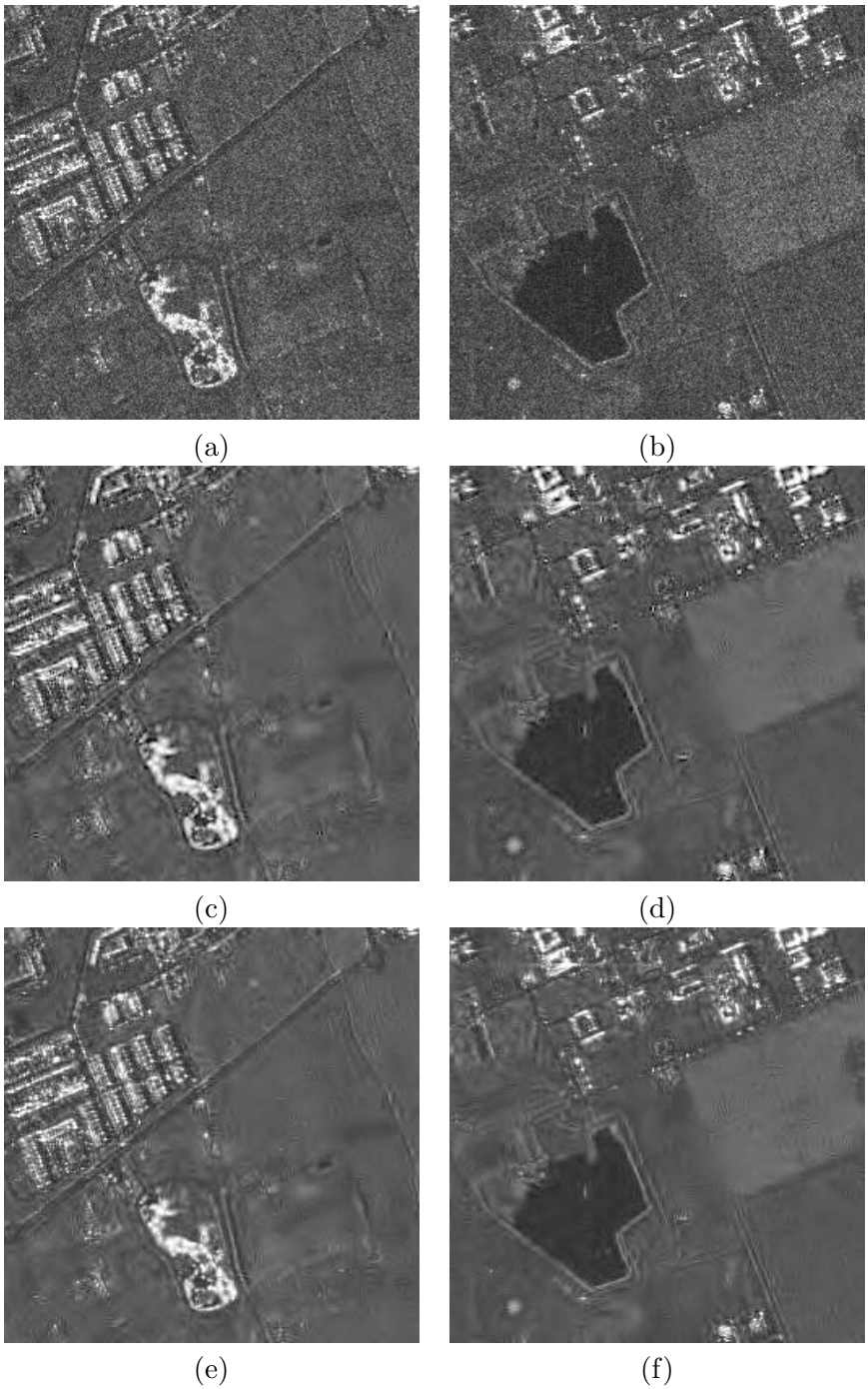

Figure 4.4: *Example of despeckling of the 4-look intensity COSMO-SkyMed images: (a)-(b) original; (c)-(d) MAP-GG-S filtered, IF; (e)-(f) MAP-GG-S filtered, SIF.*

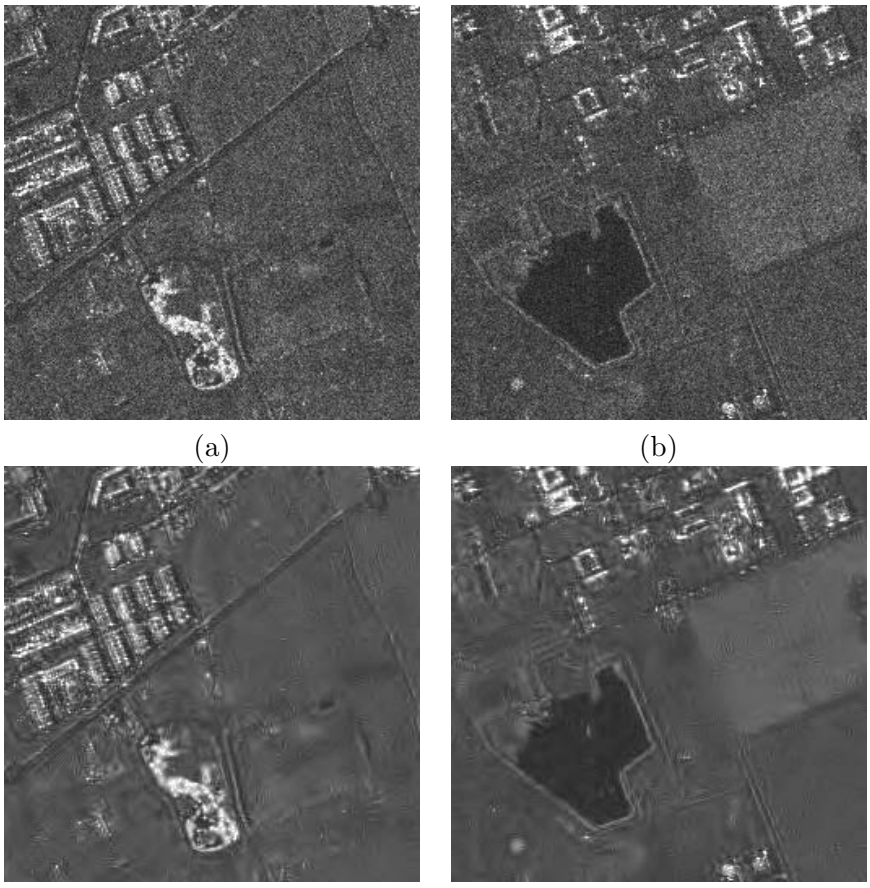

Figure 4.5: *Example of despeckling of the 4-look amplitude COSMO-SkyMed images: (a)-(b) original; (c)-(d) MAP-GG-S filtered.*

Table 4.7: *Statistical parameters derived from 1-look (CS–1L) and 4-look intensity (CS–4L) COSMO-SkyMed images despeckled by means of various filter.*

image	filter	Zone A				Zone B			
		$\mu_{\hat{u}}$		$\sigma^2_{\hat{u}} \cdot L$		$\mu_{\hat{u}}$		$\sigma^2_{\hat{u}} \cdot L$	
		IF	SIF	IF	SIF	IF	SIF	IF	SIF
CS–1L	LMMSE	0.92	0.91	0.661	0.627	0.91	0.90	0.630	0.606
	MAP GG	0.99	0.99	0.980	0.954	0.98	0.98	0.935	0.918
	GG MAP-S	0.99	0.99	0.980	0.954	0.98	0.98	0.935	0.918
	MAP LG	0.98	0.98	0.912	0.890	0.96	0.97	0.868	0.859
	LG MAP-S	0.98	0.98	0.912	0.890	0.96	0.97	0.868	0.859
CS–4L	LMMSE	0.95	0.96	0.726	0.721	0.95	0.96	0.701	0.706
	MAP GG	0.99	1.00	1.280	1.170	0.99	1.00	1.143	1.117
	GG MAP-S	0.99	1.00	1.269	1.156	0.99	1.00	1.143	1.117
	MAP LG	0.98	0.99	1.078	1.085	0.98	0.99	1.034	1.045
	LG MAP-S	0.98	0.99	1.073	1.079	0.98	0.99	1.034	1.045

Table 4.8: *Statistical parameters derived from 4-look amplitude (CS–4L–AF) COSMO-SkyMed images despeckled by means of various filter.*

image	filter	Zone A		Zone B	
		$\mu_{\hat{u}}$	$\sigma^2_{\hat{u}} \cdot L$	$\mu_{\hat{u}}$	$\sigma^2_{\hat{u}} \cdot \frac{\pi L}{4-\pi}$
CS–4L–AF	LMMSE	0.99	0.731	0.99	0.736
	MAP GG	1.00	1.140	1.00	1.121
	GG MAP-S	1.00	1.127	1.00	1.121
	MAP LG	0.99	1.062	0.99	1.068
	LG MAP-S	0.99	1.057	0.99	1.069

The results obtained on synthetically degraded images show that a significant improvement of objective quality measures can be observed when the wavelet decomposition is applied on amplitude images. On the other hand, for both synthetically speckled and true SAR images, filtering either in the amplitude or in the intensity domain yields statistical parameters of the extracted speckle noise which are quite similar. For the MAP GG and MAP GG-S filters this is not surprising, since both filters already achieved almost optimal performance in the SIF case. Moreover, this fact indicates that, even though the domain of filtering may not significantly affect the global statistical performance of the filters, filtering in the amplitude domain yields a better preservation of structural details. The above observation is confirmed by the visual inspection of filtered SAR data, since images filtered in either SIF or AF domain show less artifacts in the presence of highly heterogeneous areas.

The observed behaviour can be explained by a more effective modeling of the wavelet coefficients of amplitude SAR signals and a more robust estimation of the moments for the amplitude case. The above results also suggest that AF and SIF should be the preferred image formats when despeckling is performed in the wavelet domain, and that existing IF images should always be converted to SIF before processing with this kind of despeckling filters.

4.4 Appendix

4.4.1 Derivation of amplitude multi-look speckle moments

In this section we explicitly derive the relations in (4.12).

When u is the average of L i.i.d. variables r_i, $i = 1, \ldots, L$, distributed according to (4.3), its moments can be derived as follows:

$$\mu_u^{[1]}(L) = E\left[\frac{1}{L}\sum_i r_i\right] = \frac{1}{L}\sum_i E[r_i] = E[r] \tag{4.20}$$

$$
\begin{aligned}
\mu_u^{[2]}(L) &= E\left[\left(\frac{1}{L}\sum_i r_i\right)^2\right] \\
&= \frac{1}{L^2}\left(\sum_i E[r_i^2] + \sum_i \sum_{j\neq i} E[r_i]E[r_j]\right) \\
&= \frac{1}{L}E[r^2] + \frac{L-1}{L}E[r]^2
\end{aligned}
\tag{4.21}
$$

$$
\begin{aligned}
\mu_u^{[3]}(L) =& E\left[\left(\frac{1}{L}\sum_i r_i\right)^3\right] \\
=& \frac{1}{L^3}\left(\sum_i E[r_i^3] + 3\sum_i \sum_{j\neq i} E[r_i^2]E[r_j]\right. \\
&\left. + \sum_i \sum_{j\neq i} \sum_{k\neq j\neq i} E[r_i]E[r_j]E[r_k]\right) \\
=& \frac{1}{L^2}E[r^3] + \frac{3(L-1)}{L^2}E[r^2]E[r] \\
&+ \frac{(L-2)(L-1)}{L^2}E[r]^3
\end{aligned}
\tag{4.22}
$$

$$
\begin{aligned}
\mu_u^{[4]}(L) =& E\left[\left(\frac{1}{L}\sum_i r_i\right)^4\right] \\
=& \frac{1}{L^4}\left(\sum_i E[r_i^4] + 4\sum_i\sum_{j\neq i} E[r_i^3]E[r_j]\right. \\
&+3\sum_i\sum_{j\neq i} E[r_i^2]E[r_j^2] \\
&+6\sum_i\sum_{j\neq i}\sum_{k\neq j\neq i} E[r_i^2]E[r_j]E[r_k] \\
&\left.+\sum_i\sum_{j\neq i}\sum_{k\neq j\neq i}\sum_{h\neq k\neq j\neq i} E[r_i]E[r_j]E[r_k]E[r_h]\right) \\
=& \frac{1}{L^3}E[r^4] + \frac{4(L-1)}{L^3}E[r^3]E[r] + \frac{3(L-1)}{L^3}E[r^2]^2 \\
&+\frac{6(L-2)(L-1)}{L^3}E[r^2]E[r]^2 \\
&+\frac{(L-3)(L-2)(L-1)}{L^3}E[r]^4
\end{aligned}
\tag{4.23}
$$

where $E[r^m] = \mu_u^{[m]}(1)$. After some simple algebra, the moments result to be those expressed in (4.12).

Chapter 5

Removal of correlated speckle noise

An assumption that is made in most of the despeckling methods that have been proposed in the literature is that the speckle noise is an uncorrelated process that affects the noise-free data. However, this hypothesis does not often hold in practice and other issues inherent to the acquisition system, such as band-limitedness, suggest the use of a more sophisticated model. A model of a SAR acquisition system, often considered as sufficiently realistic, includes a linear time-invariant system, whose impulse response or point spread function spatially correlates the data. In actual SAR data, the point spread function (PSF) must be considered as an unknown and its estimation is based on the observed image. An accurate description of a model that includes the presence of a PSF and of the statistical properties of a SAR image satisfying that model is given in [18].

Applying despeckling methods derived from the uncorrelated data hypothesis to actually correlated data yields a significant loss of performance in speckle removal. Hence, some methods have been developed relying upon the correlated signal model. In [60], using a linear minimum mean square error (LMMSE) estimation approach, a local Wiener solution that assumes correlated data is proposed. In [61], a whitening/Gaussianization approach is developed for despeckling ultrasound images. Ultrasound (US) probes are incoherent imaging systems that produce data having a model quite close to that of SAR systems, so that despeckling methods developed for US are also useful for SAR data. Spectrum flattening is applied in [61] to the radiofrequency ultrasound signal; the envelope of the signal is then followed by a logarithmic transformation and Gaussianization process in order to apply denoising algorithms developed for additive noise. In [19], a Wiener filter for correlated SAR images working in the stationary-wavelet domain

is proposed. The method uses some results derived in [18]. It also uses the hypothesis that the imaged scene is characterized by homogeneous statistics; hence, a quad-tree decomposition is found before applying the filter. The problem of estimating the PSF and image decorrelation is also faced in [62].

In this chapter, we propose a whitening approach to produce single–look complex (SLC) data that can be suitably processed with despeckling filters designed for uncorrelated speckle noise. For invertible PSFs, we demonstrate that the whitening stage is optimal to achieve the information of interest, that is the variance of the underlying reflectivity. This result is obtained both in the Bayesian and in the classical estimation framework. The PSF is estimated by using the results in [18]. Several issues related to robustly decorrelating the SLC image, such as the treatment of point targets, whose model deviates from the fully developed speckle one, are also described. The experimental results demonstrate that the whitening process is effective and allow classical despeckling filters, derived under the hypothesis of uncorrelated noise, to be fully exploited. Three different filters, having different characteristics, have been chosen in order to assess the generality of the proposed procedure and to quantify the performance gain introduced by the whitening stage. Our tests also show that whitening is useful even when the invertible PSF hypothesis does not hold. The experimental results have been produced by using both synthetically speckled correlated images and true SAR images acquired by the COSMO-SkyMed constellation of satellites, which are affected by a strongly correlated speckle.

The following notation is used in this chapter: boldface upper case and lower case letters denote matrices and vectors, respectively; a superscript H indicates the Hermitian, i.e., the transpose and conjugation, operator; the expectation operator is denoted by $\mathbb{E}[\cdot]$ (a subscript letter may be added to indicate the variable it operates on); $\mathcal{CN}(\boldsymbol{\mu}, \mathbf{C})$ denotes a complex-valued Gaussian variable with mean $\boldsymbol{\mu}$ and covariance matrix $\mathbf{C}$.

5.1 Modelling of correlated SLC data

In Section 2.1.2 the SAR imaging system has been accounted in the acquisition process; it has been stated that, under the hypothesis of negligible thermal noise, the SLC signal after the image preprocessor is given by (2.9). In order to develop a useful model from the despeckling perspective, we firstly point out how (2.9) represents a generalization of the multiplicative model (2.5) under the hypothesis of fully–developed speckle for SLC images[18].

Assuming the observed scene be composed by a set of point scatterers, let $\sigma_c(\mathbf{r})$ be the discrete *complex backscatter* coefficient per area that describes

the radar target scene for each 2–D Cartesian coordinates $\mathbf{r} = (r_x; r_y)$. Under the hypothesis of fully–developed speckle, $\sigma_c(\mathbf{r})$ is modelled as a white complex circular symmetric Gaussian process, having zero mean and variance $\sigma(\mathbf{r})$, where $\sigma(\mathbf{r})$ is the *radar backscatter* or *target scene* that we would like to estimate. Supposing that the entire acquisition chain is likely represented by a cascade of linear filters, we can denote the transfer function of the SAR system as $h(\mathbf{r})$. Using the previous assumptions, the complex radar image $g_c(\mathbf{r})$, i.e. the coherently acquired image, can be defined as

$$g_c(\mathbf{r}) = \sigma_c(\mathbf{r}) \star h(\mathbf{r}) \tag{5.1}$$

where $\star$ denotes spatial convolution; clearly, (5.1) matches (2.9) by assuming (without loss of generality) $C = 1$. In an equivalent way, using the 2-D Fourier transform, (5.1) becomes

$$g_c(\mathbf{r}) = \mathfrak{F}^{-1}\left\{\Sigma_c(\mathbf{f}) \cdot H(\mathbf{f})\right\} \tag{5.2}$$

where $\mathfrak{F}^{-1}\{\cdot\}$ denotes the inverse Fourier transform operator, $\Sigma_c(\mathbf{f})$ denotes the Fourier transform of $\sigma_c(\mathbf{r})$, $H(\mathbf{f})$ is the Fourier transform of $h(\mathbf{r})$, and $\mathbf{f} = (f_x; f_y)$ denotes 2-D spatial frequencies. Hence, the despeckling problem consists in finding the estimator of the non-stationary radar backscatter $\sigma(\mathbf{r})$ given the observation of $g(\mathbf{r})$. Although its general validity, the model expressed in (5.2) requires the knowledge of the frequency response $H(\mathbf{f})$ of the SAR system. The problem of its estimation will be dealt with in a successive section.

In the particular case $h(\mathbf{r}) = \delta(\mathbf{r})$, the mostly used multiplicative model is obtained [14]

$$|g_c(\mathbf{r})|^2 = |\sigma_c(\mathbf{r})|^2 = \sigma(\mathbf{r}) \cdot u(\mathbf{r}) \tag{5.3}$$

where $u(\mathbf{r})$ is a white random process having exponential distribution, with unitary mean and variance.

A more general model assumes that

$$|g_c(\mathbf{r})|^2 \approx \sigma(\mathbf{r}) \cdot cs(\mathbf{r}) \tag{5.4}$$

where $cs(\mathbf{r})$ is a noise process that is supposed to be statistically independent from $\sigma(\mathbf{r})$ but spatially correlated. In [18], it has been shown that the correlation of the process $cs(\mathbf{r})$ depends on the frequency response of the SAR system and that the model expressed in (5.4) is valid when the power spectral density (PSD) of $\sigma(\mathbf{r})$ is narrower than the PSF of the SAR system. However, even the model in (5.4) may not be very accurate for a generic

$\sigma(\mathbf{r})$. According to (5.1), the expected value of $|g_c(\mathbf{r})|^2$ can be derived as

$$\begin{aligned}\mathbb{E}[|g_c(\mathbf{r})|^2] &= \sum_{\mathbf{r}'}\sum_{\mathbf{r}''} h(\mathbf{r}')h^*(\mathbf{r}'')\mathbb{E}\left[\sigma_c(\mathbf{r}-\mathbf{r}')\sigma_c^*(\mathbf{r}-\mathbf{r}'')\right] \\ &= \sum_{\mathbf{r}'} |h(\mathbf{r}')|^2 \mathbb{E}\left[|\sigma_c(\mathbf{r}-\mathbf{r}')|^2\right] \\ &= \sum_{\mathbf{r}'} |h(\mathbf{r}')|^2 \sigma(\mathbf{r}-\mathbf{r}'),\end{aligned} \tag{5.5}$$

where we have exploited the fact that $\sigma_c(\mathbf{r})$ is a zero-mean white process having variance $\sigma(\mathbf{r})$. The above equation shows that the expected value of $|g_c(\mathbf{r})|^2$ is in general different from $\sigma(\mathbf{r})$, implying that $cs(\mathbf{r})$ has not unit mean and should be modelled as a nonstationary process, which is quite far from the classical model in (5.3).

Despite of the fact that the model in (5.1) is more general and more realistic, most of the despeckling filters present in the literature are based on the multiplicative model with uncorrelated speckle, i.e., on (5.3), due to its simplicity. However, applying despeckling methods derived from the uncorrelated speckle hypothesis to SAR images satisfying the model in (5.1) yields a significant loss of performances.

5.2 Optimal whitening for correlated SLC data

5.2.1 Two stages method for despeckling

In order to obtain a more effective despeckling process, we propose to divide the task of despeckling in two consecutive steps:

1 *Whitening stage*: an estimator of the complex backscatter coefficients, $\hat{\sigma}_c(\mathbf{r})$, is obtained from the complex image $g_c(\mathbf{r})$ using the general model given in (5.2).

2 *Despeckling stage*: despeckling filters based on the model given in (5.3) are applied to $\hat{\sigma}_c(\mathbf{r})$ in order to obtain the estimated radar backscatter $\hat{\sigma}(\mathbf{r})$.

Under the hypothesis that the linear transformation in (5.1) is invertible, it will be shown in the following that an appropriate preprocessing applied to $g_c(\mathbf{r})$ allows classical despeckling methods to work without loss of performances. Hence, we do not focus our attention in developing a new despeckling filter, but instead in showing that the *whitening stage* permits to

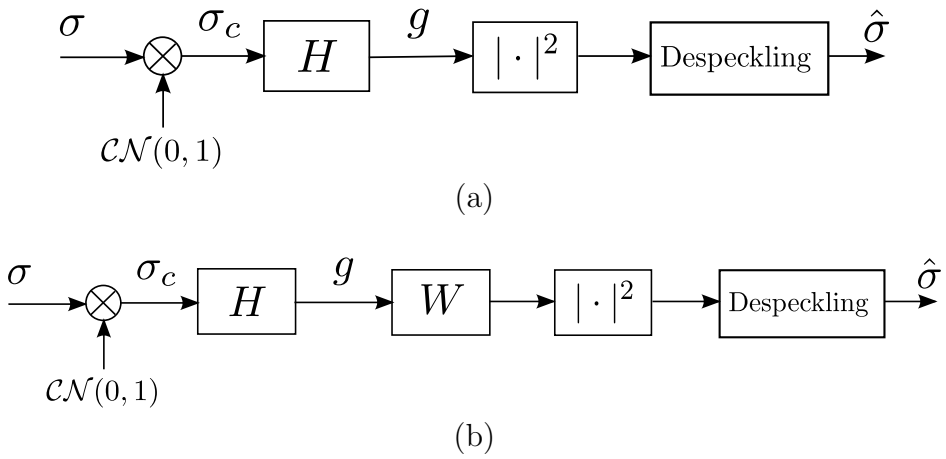

Figure 5.1: *Despeckling model in the presence of a correlated signal (a); inclusion of the whitening stage (b).*

achieve optimal solutions by using already known despeckling filters working on $\hat{\sigma}_c(\mathbf{r})$. Before stating such an optimality, some notation describing the observed variables is given. In Figure 5.1, the despeckling model in the presence of a correlated signal and that including the whitening stage are shown.

Equation (5.1) can be manipulated using R and I superscripts in order to indicate real and imaginary parts, respectively. Equation (5.1) can be rewritten as (the index $\mathbf{r}$ is dropped for the sake of simplicity)

$$\begin{aligned} g_c^R + j \cdot g_c^I &= \left(h^R + j \cdot h^I\right) \star \left(\sigma_c^R + j \cdot \sigma_c^I\right) \\ &= \left(h^R \star \sigma_c^R - h^I \star \sigma_c^I\right) + j \cdot \left(h^I \star \sigma_c^R + h^R \star \sigma_c^I\right) \end{aligned} \tag{5.6}$$

where $j = \sqrt{-1}$. Without loss of generality, suppose that the observed discrete complex backscatter signal $g_c(\mathbf{r})$ is constituted by N samples. Thus, the model in (5.6) can be expressed in vector notation as follows:

$$\mathbf{g_c} = \mathbf{H}\boldsymbol{\sigma_c} \tag{5.7}$$

where

$$\begin{aligned} \mathbf{g_c} &= \left[g^R(0) \cdots g^R(N-1), g^I(0) \cdots g^I(N-1)\right]^T \\ \boldsymbol{\sigma_c} &= \left[\sigma_c^R(0) \cdots \sigma_c^R(N-1), \sigma_c^I(0) \cdots \sigma_c^I(N-1)\right]^T \end{aligned} \tag{5.8}$$

and

$$\mathbf{H} = \begin{bmatrix} \mathbf{H^R} & -\mathbf{H^I} \\ \mathbf{H^I} & \mathbf{H^R} \end{bmatrix} \tag{5.9}$$

where $\mathbf{H^R}$ and $\mathbf{H^I}$ are the matrix representations of the linear filters h^R and h^I, respectively.

Considering that $\sigma_c(\mathbf{r})$ is a realization of a white circular symmetric complex Gaussian random process having zero mean, we have that

$$\boldsymbol{\sigma_c} \sim \mathcal{CN}\left(\mathbf{0}, \mathbf{C}_{\sigma_\mathbf{c}}\right), \quad \mathbf{C}_{\sigma_\mathbf{c}} = \operatorname{diag}\left(\left[\boldsymbol{\sigma}^T, \boldsymbol{\sigma}^T\right]^T\right)/2 \tag{5.10}$$

with $\boldsymbol{\sigma} = [\sigma(0) \cdots \sigma(N-1)]^T$.

Since $\mathbf{g_c}$ is a vector of linear combinations of $\boldsymbol{\sigma_c}$, it follows that

$$\mathbf{g_c} \sim \mathcal{CN}\left(\mathbf{0}, \mathbf{C}_{\mathbf{g_c}}\right), \quad \mathbf{C}_{\mathbf{g_c}} = \mathbf{H}\mathbf{C}_{\sigma_\mathbf{c}}\mathbf{H}^T. \tag{5.11}$$

In the following, we will state the optimality of a whitening stage for the estimation of $\boldsymbol{\sigma}$. The classical and Bayesian estimation frameworks are dealt with separately.

5.2.2 Classical estimation theory framework

In a classical estimation framework, the vector of parameters $\boldsymbol{\sigma}$ is a deterministic, but unknown, vector. Optimality of estimators can be assessed by computing the Cramer-Rao lower bound (CRLB) for any estimator of $\boldsymbol{\sigma}$.

In Section 5.7.1, it is shown that the CRLB for any unbiased estimator $\hat{\boldsymbol{\sigma}}$ of the target scene $\boldsymbol{\sigma}$ given the acquired signal $\mathbf{g_c}$ is given by

$$\mathbf{C}_{\hat{\boldsymbol{\sigma}}} - \operatorname{diag}\left(\boldsymbol{\sigma}\right)^2 \geq \mathbf{0} \tag{5.12}$$

where $\mathbf{C}_{\hat{\boldsymbol{\sigma}}}$ is the covariance matrix of the estimator and the notation $\mathbf{A} \geq \mathbf{0}$ means that the matrix $\mathbf{A}$ is positive-semidefinite. The relation in (5.12) shows that the CRLB is not influenced by the presence of the frequency response of the SAR system. This fact suggests that an estimator may remove the influence of the SAR system frequency response in order to reach the CRLB. Furthermore, it is interesting to note that the performance of each estimator is locally bounded by the local parameter itself, i.e., estimations of brighter points are noisier than estimations of darker ones.

The inequality expressed in (5.12) has a general validity since it has been derived only under the hypothesis that the filtering matrix $\mathbf{H}$ (representing the SAR system impulse response) is invertible. Interestingly, in this case an efficient estimator based on the observation of $\mathbf{g_c}$ exists. Let's define the

$N \times 1$ estimated vector $\hat{\boldsymbol{\sigma}}_{\text{eff}}$ as

$$[\hat{\boldsymbol{\sigma}}_{\text{eff}}]_n = \left|\left[\mathbf{H}^{-1}\mathbf{g_c}\right]_n\right|^2 + \left|\left[\mathbf{H}^{-1}\mathbf{g_c}\right]_{n+N}\right|^2, \qquad 0 \leq n \leq N-1. \tag{5.13}$$

or equivalently, in scalar form,

$$\hat{\sigma}_{\text{eff}}(\mathbf{r}) = \left|h^{-1}(\mathbf{r}) \star g_c(\mathbf{r})\right|^2 \qquad 0 \leq n \leq N-1, \tag{5.14}$$

where $h^{-1}(\mathbf{r})$ denotes the inverse filter of $h(\mathbf{r})$, that is $h^{-1}(\mathbf{r}) = \mathfrak{F}^{-1}\{1/H(\mathbf{f})\}$. In section 5.7.1, it is shown that such an estimator is efficient for the despeckling problem.

The expression in (5.14) highlights that the efficient estimator can be seen as a cascade of the whitening filter $h^{-1}(\mathbf{r})$ followed by the squared modulus operator $|\cdot|^2$. In other words, the whitening stage is the first part of the minimum–variance estimation strategy within the framework of classical estimation theory. It is interesting to note that no assumptions have been made on the value of $\boldsymbol{\sigma}$, except that it has no zero entries.

5.2.3 Bayesian estimation theory framework

In this section, we reformulate the optimality of the whitening processing in the framework of Bayesian estimation, in which the parameter vector $\boldsymbol{\sigma}$ is assumed as a random vector. In particular, we show that any Bayesian estimator based on the observation of the variable $\mathbf{g_c}$ coincides with that obtained observing any linear invertible transformation of $\mathbf{g_c}$.

Let $\boldsymbol{\sigma}$ be the vector of parameters to be estimated, coinciding with the radar backscatter and let $\boldsymbol{\sigma_c}$ and $\mathbf{g_c}$ be the observed signals in the whitened and correlated domain, respectively. Bayesian estimation is based on the posterior probability density function (pdf) of the parameter $\boldsymbol{\sigma}$ after observing either $\boldsymbol{\sigma_c}$ or $\mathbf{g_c}$, that is either $p(\boldsymbol{\sigma}|\boldsymbol{\sigma_c})$ or $p(\boldsymbol{\sigma}|\mathbf{g_c})$.

Let $\mathbf{x} = [\boldsymbol{\sigma}^H \ \mathbf{g_c}^H]^H$ and $\mathbf{y} = [\boldsymbol{\sigma}^H \ \boldsymbol{\sigma_c}^H]^H$ be the random vector obtained concatenating the parameter vector and the observed variables, so that $p(\mathbf{x}) = p(\boldsymbol{\sigma}, \mathbf{g_c})$ and $p(\mathbf{y}) = p(\boldsymbol{\sigma}, \boldsymbol{\sigma_c})$. According to (5.7), $\mathbf{x}$ is obtained from $\mathbf{y}$ by using a linear transformation, that is

$$\mathbf{x} = \mathbf{T}\mathbf{y} \tag{5.15}$$

where $\mathbf{T}$ denotes the invertible transformation given by

$$\mathbf{T} = \begin{bmatrix} \mathbf{I} & \mathbf{0} \\ \mathbf{0} & \mathbf{H} \end{bmatrix}. \tag{5.16}$$

The relation between $p(\mathbf{x})$ and $p(\mathbf{y})$ is given by

$$p(\mathbf{x}) = p(\mathbf{y})|J_{\mathbf{T}}(\mathbf{y})| \tag{5.17}$$

where $J_{\mathbf{T}}$ denotes the Jacobian of the transformation $\mathbf{T}$, defined by $[J_{\mathbf{T}}(\mathbf{y})]_{i,j} = \frac{\partial x_i}{\partial y_j}$, and $|\mathbf{A}|$ denotes the determinant of the matrix $\mathbf{A}$. According to the previous definitions, we have

$$J_{\mathbf{T}}(\mathbf{y}) = \mathbf{T}. \tag{5.18}$$

Hence, the posterior pdf $p(\boldsymbol{\sigma}|\mathbf{g_c})$ is given by

$$\begin{aligned} p(\boldsymbol{\sigma}|\mathbf{g_c}) &= \frac{p(\boldsymbol{\sigma}, \mathbf{g_c})}{p(\mathbf{g_c})} = \frac{p(\mathbf{x})}{p(\mathbf{g_c})} = \frac{p(\mathbf{y})|\mathbf{T}|}{p(\mathbf{g_c})} \\ &= \frac{p(\boldsymbol{\sigma}, \boldsymbol{\sigma_c})|\mathbf{T}|}{p(\mathbf{g_c})} = \frac{p(\boldsymbol{\sigma}|\boldsymbol{\sigma_c})p(\boldsymbol{\sigma_c})|\mathbf{T}|}{p(\mathbf{g_c})}. \end{aligned} \tag{5.19}$$

Considering the transformation from $\boldsymbol{\sigma_c}$ to $\mathbf{g_c}$, we have

$$p(\mathbf{g_c}) = p(\boldsymbol{\sigma_c})|J_{\mathbf{H}}(\boldsymbol{\sigma_c})| \tag{5.20}$$

where $J_{\mathbf{H}}$ denotes the Jacobian of the transformation $\mathbf{H}$ given in (5.7). Hence, we have

$$J_{\mathbf{H}}(\boldsymbol{\sigma_c}) = \mathbf{H}. \tag{5.21}$$

Since $|\mathbf{T}| = |\mathbf{H}|$, substituting (5.20) and (5.21) into (5.19) yields

$$p(\boldsymbol{\sigma}|\mathbf{g_c}) = p(\boldsymbol{\sigma}|\boldsymbol{\sigma_c}). \tag{5.22}$$

From this expression, we can conclude that any Bayesian estimator, e.g., those based on the MAP and MMSE criterion, can be derived in an equivalent way by using either the variable $\boldsymbol{\sigma_c}$ or the transformed variable $\mathbf{g_c}$.

5.3 Estimation of the complex backscatter coefficients

The estimation of the source signal $\sigma_c(\mathbf{r})$ given the observation of the output $g_c(\mathbf{r})$ from an unknown linear system $h(\mathbf{r})$ is a typical problem of blind deconvolution [63]. Several methods have been proposed in the literature in the last two decades in the field of image restoration [64, 63, 65]. Many of them are based on iterative algorithms and/or require some hypotheses on the prior distribution and the hyperparameters of the source signal in order to use the Bayesian inference framework.

In our approach, any assumption on the statistical distribution of the target scene $\sigma(\mathbf{r})$ is avoided. We will use some results from [18] as well as some hypothesis on the frequency response of the SAR system.

From the observation of the spectrum of a real SAR acquisition (see the experimental results section) it can be inferred that the SAR system can be represented by a band-limited lowpass filter with cutoff frequencies $f_{c,x}$ and $f_{c,y}$, i.e., by defining $\mathcal{F}_p = \{\mathbf{f} : |f_x| \leq f_{c,x}, |f_y| \leq f_{c,y}\}$ we have

$$H(\mathbf{f}) \approx 0 \quad \mathbf{f} \notin \mathcal{F}_p. \tag{5.23}$$

Moreover, without loss of generality, we can assume that the filter $H(\mathbf{f})$ has unit energy, i.e.,

$$\int_{\mathbf{f}\in\mathcal{F}_p} |H(\mathbf{f})|^2 \mathrm{d}\mathbf{f} = 1. \tag{5.24}$$

Equation (5.23) implies that the PSF of a real SAR system may not be invertible. In this case a true whitening operator can not be defined. Nevertheless, we may intuitively assume that flattening the spectrum of the received complex radar image in the passband of the filter $H(\mathbf{f})$ remains a good strategy to approximate a white process. A flattening approach to despeckle ultrasound images has been used in [61, 66]. Our experimental results show that the flattening strategy yields a significant improvement in terms of despeckling performance.

If $\hat{H}(\mathbf{f})$ is an estimate of $H(\mathbf{f})$, then we can define an estimate of the complex backscatter coefficients $\hat{\sigma}_c(\mathbf{r})$ as

$$\hat{\sigma}_c(\mathbf{r}) = \begin{cases} \mathfrak{F}^{-1}\left\{W(\mathbf{f}) \cdot G_c(\mathbf{f})\right\} & \mathbf{f} \in \mathcal{F}_p \\ 0 & \text{otherwise} \end{cases} \tag{5.25}$$

where $W(\mathbf{f}) = \gamma \hat{H}(\mathbf{f})^{-1}$ is the whitening filter, $G(\mathbf{f}) = \mathfrak{F}\{g(\mathbf{r})\}$, and γ is a suitable scaling constant. In Section 5.7.2, we show that the above solution yields the minimum norm estimate of $\hat{\sigma}_c(\mathbf{r})$.

5.3.1 Estimation of the SAR system frequency response

The estimation of $H(\mathbf{f})$ can be performed by using the results in [18], where it has been demonstrated that the average spectrum of $g_c(\mathbf{r})$, denoted as $\overline{S}_{g_c}(\mathbf{f})$, is given by

$$\overline{S}_{g_c}(\mathbf{f}) = \mathfrak{F}\left\{\overline{R_{g_c}}(\mathbf{r})\right\} = \overline{\sigma}\,|H(\mathbf{f})|^2\,, \tag{5.26}$$

where $\overline{R_{g_c}}(\mathbf{r})$ is the average autocorrelation of $g_c(\mathbf{r})$ taken over an $N_\mathcal{D} \times N_\mathcal{D}$ spatial window $\mathcal{D}$ when $N_\mathcal{D}$ tends to infinity [18], that is

$$\overline{R_{g_c}}(\mathbf{r}) = \lim_{N_\mathcal{D}\to\infty} \frac{1}{N_\mathcal{D}^2} \sum_{\mathbf{r}'\in\mathcal{D}} \mathbb{E}[g_c(\mathbf{r}+\mathbf{r}')g_c{}^*(\mathbf{r}')] \tag{5.27}$$

and where the spatial average radar backscatter $\overline{\sigma}$ is given by

$$\overline{\sigma} = \lim_{N_\mathcal{D}\to\infty} \frac{1}{N_\mathcal{D}^2} \sum_{\mathbf{r}'\in\mathcal{D}} \sigma(\mathbf{r}'). \tag{5.28}$$

It is worth noting that, under the hypothesis of a unit energy filter $H(\mathbf{f})$, the average radar backscatter of the scene is preserved, since $\int \overline{S}_{g_c}(\mathbf{f})\mathrm{d}\mathbf{f} = \overline{\sigma}$.

As in [19], we will use a nonparametric spectrum estimation method to achieve the average spectrum $\overline{S}_{g_c}(\mathbf{f})$. By using the Bartlett-Welch method [67], we have

$$\hat{S}_{g_c}(\mathbf{f}) = \frac{1}{N_\mathcal{C}} \sum_{\mathbf{c}\in\mathcal{C}} \left| \mathfrak{F}\left\{ g_c(\mathbf{r}) \cdot \frac{w(\mathbf{r}-\mathbf{c})}{N_w} \right\} \right|^2 \tag{5.29}$$

where $w(\mathbf{r})$ is a zero-centered N_w–points weighting window, $\mathbf{c}$ is a shift applied to the window, $\mathcal{C}$ is the set of all shifts of the window over the image, $N_\mathcal{C}$ is the cardinality of $\mathcal{C}$. It is well-known that $\hat{S}_{g_c}(\mathbf{f})$ is an asymptotically unbiased and efficient estimate of $\overline{S}_{g_c}(\mathbf{f})$, i.e.

$$\hat{S}_{g_c}(\mathbf{f}) = \overline{S}_{g_c}(\mathbf{f}) + \Delta(\mathbf{f}) \tag{5.30}$$

where $\Delta(\mathbf{f})$ represents a zero-mean approximation error. As to the average radar backscatter of the scene, this can be estimated as

$$\hat{\sigma} = \int \hat{S}_{g_c}(\mathbf{f})\mathrm{d}\mathbf{f}. \tag{5.31}$$

It is easy to verify that this is also an asymptotically unbiased estimator, since

$$\begin{aligned} \mathbb{E}\left[\hat{\sigma}\right] =& \mathbb{E}\left[\int \left[\overline{\sigma}|H(\mathbf{f})|^2 + \Delta(\mathbf{f})\right] \mathrm{d}\mathbf{f}\right] \\ =& \mathbb{E}\left[\overline{\sigma} + \int \Delta(\mathbf{f})\mathrm{d}\mathbf{f}.\right] \\ =& \overline{\sigma} \end{aligned} \tag{5.32}$$

In order to facilitate the whitening process and to avoid phase distor-

tion in the detected image, we will assume that the SAR system impulse response $h(\mathbf{r})$ is a linear-phase FIR filter. We will also assume that the SAR system frequency response $H(\mathbf{f})$ can be approximated by a real central–symmetric non-negative function with unit energy belonging to a set of known parameter-dependent curves $F(\mathbf{f};\boldsymbol{\phi})$, where $\boldsymbol{\phi}$ is a vector parameter. In the experimental results section, we will show that a raised-cosine function fits quite well the observed $\hat{S}_{g_c}(\mathbf{f})$. Formally, we assume that

$$\exists \boldsymbol{\phi}_0 \in \Phi : F(\mathbf{f};\boldsymbol{\phi}_0) \approx H(\mathbf{f}) \quad \forall \mathbf{f} \tag{5.33}$$

where Φ is the $\boldsymbol{\phi}$ parameter space and where, for all $\boldsymbol{\phi}$, $F(\mathbf{f};\boldsymbol{\phi})$ satisfies the properties

$$\begin{gathered} F(\mathbf{f};\boldsymbol{\phi}) \geq 0 \\ F(\mathbf{f};\boldsymbol{\phi}) = F(-\mathbf{f};\boldsymbol{\phi}) \\ \int_{\mathbf{f}\in\mathcal{F}_p} F^2(\mathbf{f};\boldsymbol{\phi})\mathrm{d}\mathbf{f} = 1. \end{gathered}$$

Hence, by using (5.33) together with (5.30), the approximation model becomes

$$\begin{aligned} \hat{S}_{g_c}(\mathbf{f}) &\approx \overline{\sigma} F^2(\mathbf{f};\boldsymbol{\phi}_0) + \Delta(\mathbf{f}) \\ &\approx \hat{\sigma} F^2(\mathbf{f};\boldsymbol{\phi}_0) + \Delta(\mathbf{f}) \end{aligned} \tag{5.34}$$

where, according to (5.32), we have assumed $\overline{\sigma} \approx \hat{\sigma}$.

The least square (LS) solution to our approximation model aims at minimizing the energy of $\Delta(\mathbf{f})$. Hence, the LS estimator of $\boldsymbol{\phi}_0$ is given by

$$\hat{\boldsymbol{\phi}}_{\mathrm{LS}} = \arg\min_{\boldsymbol{\phi}} \int_{\mathbf{f}\in\mathcal{F}_p} \left| \hat{S}_{g_c}(\mathbf{f}) - \hat{\sigma} F^2(\mathbf{f};\boldsymbol{\phi}) \right|^2 \mathrm{d}\mathbf{f}. \tag{5.35}$$

Finally, the whitening filter can be obtained as

$$W(\mathbf{f}) = \gamma \cdot F(\mathbf{f};\hat{\boldsymbol{\phi}}_{\mathrm{LS}})^{-1}. \tag{5.36}$$

5.4 Implementation of the despeckling algorithm

In this section, we take into account some practical issues that must be faced for implementing the proposed whitening method in order to pre-

vent undesired results. At the end, the complete procedure of the proposed method is given.

5.4.1 LS fitting and average spectrum estimation

In order to simplify the estimation of the whitening filter, we assume that the band-limited frequency response $H(\mathbf{f})$ of the SAR system can be expressed by a separable function

$$F(\mathbf{f};\boldsymbol{\phi}) = F_x(f_x;\phi_x)\cdot F_y(f_y;\phi_y),$$

where both $F_x(f_x;\phi_x)$ and $F_y(f_y;\phi_y)$ are such that

$$\int |F_x(f_x;\phi_x)|^2 df_x = \int |F_y(f_y;\phi_y)|^2 df_y = 1.$$

In this way, the approximation model in (5.34) can be simplified as

$$\hat{S}_{g_c,x}(f_x) = \int \hat{S}_{g_c}(\mathbf{f})df_y \approx \hat{\sigma}F_x^2(f_x;\phi_{0,x}) + \int \Delta(\mathbf{f})df_y \tag{5.37}$$

$$\hat{S}_{g_c,y}(f_y) = \int \hat{S}_{g_c}(\mathbf{f})df_x \approx \hat{\sigma}F_y^2(f_y;\phi_{0,y}) + \int \Delta(\mathbf{f})df_x \tag{5.38}$$

and the decorrelating filter can be estimated by solving two separate LS problems. The two quantities $\hat{S}_{g_c,x}(f_x)$, $\hat{S}_{g_c,y}(f_y)$, corresponding to one-dimensional average periodograms along the x and y coordinates, respectively, are estimated as follows

$$\hat{S}_{g_c,x}(f_x) = \int \left|\mathfrak{F}\left\{g_c(\mathbf{r})\right\}\right|^2 df_y \tag{5.39}$$

$$\hat{S}_{g_c,y}(f_y) = \int \left|\mathfrak{F}\left\{g_c(\mathbf{r})\right\}\right|^2 df_x. \tag{5.40}$$

According to (5.35), LS fitting only considers frequencies in which $H(\mathbf{f})$ is supposed to be nonzero. In our implementation, the cutoff frequencies along each spatial frequency are either supposed to be known from the technical specifications of the SAR system or manually estimated from the inspection of the average periodograms.

5.4.2 Choice of the scaling constant

The scaling constant γ influences the value of the radar backscatter of the decorrelated signal $\hat{\sigma}_c(\mathbf{r})$. In our implementation, we choose to preserve

the average backscatter $\overline{\sigma}$ of the observed scene, i.e., we impose

$$\int \overline{S}_{\hat{\sigma_c}}(\mathbf{f})\mathrm{d}\mathbf{f} = \overline{\sigma} \tag{5.41}$$

which, from (5.25) and (5.26), is equivalent to

$$\int_{\mathbf{f}\in\mathcal{F}_p} |W(\mathbf{f})H(\mathbf{f})|^2\mathrm{d}\mathbf{f} = 1. \tag{5.42}$$

If we assume that the whitening filter is ideal, i.e., $W(\mathbf{f}) = \gamma H(\mathbf{f})^{-1}$, the above condition implies

$$\gamma = \left(\int_{\mathbf{f}\in\mathcal{F}_p} \mathrm{d}\mathbf{f}\right)^{-1/2} \tag{5.43}$$

showing that the ideal scaling constant depends on the cutoff frequency of the system.

By ensuring that the average radar backscatter is preserved on the whole scene we also ensure that the backscatter is approximately preserved in locally stationary areas affected by fully developed speckle, i.e, in areas for which it is valid the approximation in (5.4). Nevertheless, the above strategy does not work well in highly heterogeneous areas that do not obey the fully developed speckle model, e.g., in the presence of point targets. In the following, we will see how to cope with the above problem.

5.4.3 Processing of point targets

Real SAR images usually contain point targets, which are due to man-made features or edges. Such strong scatterers must be generally preserved because they show a high level of reflectivity with no speckle noise. Since point targets do not obey the zero-mean white complex circular symmetric Gaussian model, they have to be detected and replaced in order to estimate the complex backscatter coefficients according to (5.25).

Let the set of non–point targets pixels of the complex image $g_c(\mathbf{r})$ be

$$\mathcal{Q}_{g_c} = \left\{\mathbf{r} \in \mathbb{Z}^2 : |g_c(\mathbf{r})|^2 < \tau\right\} \tag{5.44}$$

where τ is a suitable threshold, which can be experimentally determined by observing the histogram of $|g_c(\mathbf{r})|^2$. Then we define the modified complex

image $g_m(\mathbf{r})$ as

$$g_m(\mathbf{r}) = \begin{cases} g_c(\mathbf{r}) & \mathbf{r} \in \mathcal{Q}_{g_c} \\ \epsilon(\mathbf{r}) & \mathbf{r} \notin \mathcal{Q}_{g_c} \end{cases} \tag{5.45}$$

where $\epsilon(\mathbf{r})$ is a complex circular symmetric Gaussian variable satisfying

$$\epsilon(\mathbf{r}) \sim \mathcal{CN}\left(0\ ;\ \sum_{\mathbf{r}\in\mathcal{Q}_{g_c}} |g_c(\mathbf{r})|^2 / |\mathcal{Q}_{g_c}|\right) \tag{5.46}$$

with $|\mathcal{Q}_{g_c}|$ the number of the elements of $\mathcal{Q}_{g_c}$. In other words, we substitute each point target of the original complex image $g_c(\mathbf{r})$ with a realization of a zero–mean white complex circular symmetric Gaussian variable, whose variance is given by the average energy of non–point targets pixels.

It should be pointed out that, in the case of a band-limited SAR system, the replacement proposed in (5.45) is also useful to prevent the whitening method from spreading the energy of point targets in the surrounding areas and making cross-like features appear around strong scatterers.

5.4.4 Summary of the complete despeckling procedure

1) Detect the set of point targets $\mathcal{Q}_{g_c}$ according to (5.44);

2) Generate the modified complex image $g_m(\mathbf{r})$, removing point targets as stated in (5.46);

3) Estimate the SAR system frequency response, $\hat{H}(\mathbf{f})$, using (5.35), where the complex image $g_c(\mathbf{r})$ is replaced with the modified version $g_m(\mathbf{r})$;

4) Estimate the complex backscatter coefficients, $\hat{\sigma}_c(\mathbf{r})$, by means of (5.25), where the complex image $g_c(\mathbf{r})$ is replaced with the modified version $g_m(\mathbf{r})$;

5) Estimate the radar backscatter $\hat{\sigma}(\mathbf{r})$ applying a despeckling filter based on the uncorrelated speckle hypothesis to $|\hat{\sigma}_c(\mathbf{r})|^2$;

6) Re–insert the point targets in $\hat{\sigma}(\mathbf{r})$:

$$\hat{\sigma}(\mathbf{r}) = \begin{cases} \hat{\sigma}(\mathbf{r}) & \mathbf{r} \notin \mathcal{Q}_{g_c} \\ |g_c(\mathbf{r})|^2 & \mathbf{r} \in \mathcal{Q}_{g_c}. \end{cases} \tag{5.47}$$

5.5 Experimental results

In this section, the experimental results obtained with the proposed method are presented[1]. As to the despeckling stage, we will consider three different filters: the Γ-MAP filter [42], the MAP filter in the undecimated wavelet domain with the assumption of generalized Gaussian distributed coefficients and segmentation (GG MAP-S) [41], and the probabilistic patch–based (PPB) filter [57]. For each of them, we compare the results obtained with the inclusion of the whitening stage we have introduced (denoted in short as W) and without using it (denoted as NW).

Tests have been carried out on both synthetically speckled images and real SAR images. In all tests, we assumed that the separable components of the frequency response of the SAR system belong to the class of raised cosine functions, that is

$$H_z(f_z) = \begin{cases} A_z - B_z \cdot \cos[\pi(f_z + f_{c,z})/f_{c,z}] & |f_z| \leq f_{c,z} \\ 0 & \text{otherwise} \end{cases} \tag{5.48}$$

where $z \in \{x, y\}$, $f_{c,z}$ is the known cutoff frequency, and $A_z > B_z > 0$ are the model parameters chosen with the constraint of unit energy.

As to the threshold used to select the point targets, described in Section 5.4.3, we set $\tau = \infty$ for synthetically degraded images and $\tau = 5 \cdot \text{median}[|g_c(\mathbf{r})|^2]$ for real SAR images.

5.5.1 Performance indexes

The performances of the filters have been assessed by using different indexes. As to simulated images, the performances are measured by computing the PSNR (4.18) and MSSIM (4.19) between the original and the filtered image, defined in Section 4.2, where $I = \sqrt{\sigma}$ and $I_{peak} = 255$ are substituted.

As to performance index which does not require the reference image, according to Sections 3.3.3 and 4.2 and the notation adopted in this chapter, the ratio image is defined as $\hat{u}(\mathbf{r}) = |g_c(\mathbf{r})|^2/\hat{\sigma}(\mathbf{r})$, where $\hat{\sigma}(\mathbf{r})$ represents the estimated noise–free reflectivity. When a fully–developed uncorrelated speckle model can be assumed, the above image represents the filtered out speckle noise. Hence, for a good despeckling filter $\hat{u}(\mathbf{r})$ should satisfy $\mathbb{E}[\hat{u}(\mathbf{r})] = 1$ and $\text{Var}[\hat{u}(\mathbf{r})] = 1$ [11]. When the above statistics are computed on local windows, the method is accurate also in the case of real SAR images, for

[1] An implementation of the proposed whitening approach can be tested through a Web service available at http://iapp.dinfo.unifi.it/despeckle.

which the assumption of fully–developed speckle is not valid everywhere and global statistics would be biased due to the presence of outliers. However, when the SAR signal follows the general model in (5.1), the expected value of $|g_c(\mathbf{r})|^2$ is different from $\sigma(\mathbf{r})$, as shown in equation (5.5). As a consequence, even in the presence of an ideal despeckling filter the statistics of $\hat{u}(\mathbf{r})$ would differ from the expected ones. Hence, in the presence of correlated speckle we re-define the ratio image as

$$\hat{u}(\mathbf{r}) = \frac{|g_c(\mathbf{r})|^2}{\sum_{\mathbf{r}'} |h(\mathbf{r}')|^2 \hat{\sigma}(\mathbf{r}-\mathbf{r}')} \tag{5.49}$$

where in the case of real SAR images the impulse response of the SAR system is replaced by the estimated response $\hat{h}(\mathbf{r}) = \mathfrak{F}^{-1}\{F(\mathbf{f}; \hat{\boldsymbol{\phi}}_{\mathrm{LS}})\}$.

In the case of SAR images, we also compute some other indexes. The effectiveness of despeckling is evaluated by computing the ENL of the filtered image over manually selected regions in which a homogeneous backscatter is assumed; ENL is defined, according to Section 3.2.5, as

$$\mathrm{ENL}(\mathbf{r}) = \frac{\mathbb{E}[|\hat{\sigma}(\mathbf{r})|]^2}{\mathrm{Var}[|\hat{\sigma}(\mathbf{r})|]}. \tag{5.50}$$

The effectiveness of the whitening procedure is evaluated by estimating the normalized autocorrelation of the speckle. Following the approach in [18], this is computed as

$$\rho(\mathbf{r}) = \frac{|\rho_{g_c}(\mathbf{r})|^2}{|\rho_{g_c}(\mathbf{0})|^2} \tag{5.51}$$

where $\rho_{g_c}(\mathbf{r}) = \frac{1}{N(\mathbf{r})} \sum_{\mathbf{r}' \in \mathcal{Q}_{g_c}} g_c(\mathbf{r}+\mathbf{r}') g_c^*(\mathbf{r}')$ and $N(\mathbf{r})$ takes into account both the size of $\mathcal{Q}_{g_c}$ and the number of overlapping points between translated replicas of $g_c(\mathbf{r})$.

The preservation of radiometric features is measured using the target-to-clutter ratio (TCR), defined as

$$\mathrm{TCR} = 10 \log_{10} \frac{|\mathcal{P}| \cdot \max_{\mathbf{r} \in \mathcal{P}} |g_c(\mathbf{r})|^2}{\sum_{\mathbf{r} \in \mathcal{P}} |g_c(\mathbf{r})|^2} \tag{5.52}$$

and the bias between the original and the whitened image, measured as

$$\mathrm{Bias} = 10 \log_{10} \frac{\sum_{\mathbf{r} \in \mathcal{P}} |\hat{\sigma}_c(\mathbf{r})|^2}{\sum_{\mathbf{r} \in \mathcal{P}} |g_c(\mathbf{r})|^2} \tag{5.53}$$

where $\mathcal{P}$ denotes an appropriate image patch.

(a) (b) (c) (d)

Figure 5.2: *Original optical images:* Lena *(a)*, Barbara *(b)*, San Francisco *(c)*, Stockton *(d)*

5.5.2 Results on synthetically degraded images

A set of synthetically speckled images have been generated according to (5.2). A reference test image has been first multiplied with a white circular complex Gaussian process, with zero mean and unit variance, and then filtered by $H(\mathbf{f})$. As reference target scene, we have used four optical 8 bit, 512×512, images (*Lena*, *Barbara*, *San Francisco*, *Stockton*), which are shown in Figure 5.2[2].

In order to avoid the results to be biased by a specific shape of the filter, the parameters (A_z, B_z) have been randomly generated for each realization of the complex images. Ten realizations have been used for the computation of each performance index and the mean taken.

In Table 5.1–5.4, the PSNR, the MSSIM, the mean and the variance of the ratio image $\hat{u}$ are presented. The results are shown by using the cutoff frequency f_c (normalized to half the sampling frequency) as a parameter. For each considered despeckling filter, the results obtained by using the whitening stage (W) and without using it (NW) are reported. From the observation of the Tables, some considerations can be made. The whitening stage always improves reference–based performance indexes, i.e., PSNR and MSSIM, except for two specific cases in 5.3. This trend can be observed irrespective of the test image and of the despeckling filter. The performance gain is higher for lower cutoff frequencies. This fact is not surprising, since for lower cutoff frequencies speckle correlation is higher and poorer performances of despeckling filters based on the uncorrelated noise assumption are expected. The filter that benefits more from the use of whitening is the GG MAP-S, followed by the PPB. This can be explained by the fact that these filters rely more heavily on the uncorrelated speckle assumption.

The whitening stage also improves performance indexes which are not

[2]The corresponding degraded and filtered images are available at http://iapp.dinfo.unifi.it/index.php/decorrelation-despeckling-results.

Table 5.1: *Performance indexes obtained on* Lena *by means of different filters applied in the absence (NW) and in the presence (W) of a whitening stage (best index values for each cutoff frequency are highlighted in bold).*

	f_c	Γ–MAP		GG MAP-S		PPB	
		NW	W	NW	W	NW	W
PSNR	0.6	20.31	21.64	18.33	23.23	21.11	**24.53**
	0.7	21.04	22.07	20.88	24.75	23.60	**25.23**
	0.8	21.61	22.31	23.30	25.43	25.06	**25.62**
	0.9	21.78	22.31	24.26	25.70	25.47	**25.96**
MSSIM	0.6	0.405	0.447	0.273	0.529	0.453	**0.606**
	0.7	0.431	0.467	0.381	**0.650**	0.557	0.638
	0.8	0.454	0.481	0.525	**0.702**	0.618	0.651
	0.9	0.464	0.489	0.593	**0.716**	0.637	0.658
$\mathbb{E}[\hat{u}]$	0.6	**0.989**	0.988	0.904	0.926	0.914	0.936
	0.7	0.997	**0.999**	0.923	0.949	0.929	0.946
	0.8	**1.000**	1.007	0.936	0.962	0.936	0.949
	0.9	**1.001**	1.009	0.952	0.967	0.939	0.948
$\mathrm{Var}[\hat{u}]$	0.6	0.750	**0.825**	0.477	0.698	0.614	0.807
	0.7	0.791	**0.863**	0.593	0.819	0.716	0.859
	0.8	0.803	0.883	0.672	**0.894**	0.762	0.881
	0.9	0.807	0.870	0.785	**0.932**	0.806	0.881

Table 5.2: *Performance indexes obtained on* Barbara *by means of different filters applied in the absence (NW) and in the presence (W) of a whitening stage (best index values for each cutoff frequency are highlighted in bold).*

	f_c	Γ–MAP		GG MAP-S		PPB	
		NW	W	NW	W	NW	W
PSNR	0.6	19.13	20.04	17.62	21.04	19.64	**21.70**
	0.7	19.61	20.32	19.48	21.90	21.19	**22.12**
	0.8	19.91	20.39	20.99	22.27	22.03	**22.46**
	0.9	20.12	20.32	22.02	22.47	22.70	**22.93**
MSSIM	0.6	0.385	0.414	0.286	0.460	0.420	**0.520**
	0.7	0.407	0.431	0.366	0.535	0.495	**0.547**
	0.8	0.426	0.445	0.458	**0.567**	0.544	0.565
	0.9	0.445	0.459	0.536	0.582	0.584	**0.594**
$\mathbb{E}[\hat{u}]$	0.6	**0.984**	0.983	0.901	0.919	0.907	0.927
	0.7	**0.993**	0.990	0.919	0.936	0.923	0.931
	0.8	**0.997**	0.996	0.933	0.948	0.930	0.933
	0.9	**0.998**	1.003	0.944	0.953	0.931	0.931
$\mathrm{Var}[\hat{u}]$	0.6	0.740	**0.822**	0.473	0.695	0.597	0.795
	0.7	0.790	**0.852**	0.599	0.811	0.714	0.840
	0.8	0.805	0.867	0.702	**0.895**	0.774	0.866
	0.9	0.801	0.862	0.781	**0.938**	0.801	0.864

Table 5.3: *Performance indexes obtained on* San Francisco *by means of different filters applied in the absence (NW) and in the presence (W) of a whitening stage (best index values for each cutoff frequency are highlighted in bold).*

	f_c	Γ–MAP		GG MAP-S		PPB	
		NW	W	NW	W	NW	W
PSNR	0.6	21.41	21.96	20.53	22.79	21.77	**23.21**
	0.7	21.65	22.10	21.75	23.29	22.78	**23.48**
	0.8	21.92	22.11	23.03	23.51	23.58	**23.68**
	0.9	21.91	22.02	23.41	23.67	23.88	**23.93**
MSSIM	0.6	0.469	0.497	0.378	0.544	0.521	**0.581**
	0.7	0.488	0.511	0.457	0.586	0.573	**0.594**
	0.8	0.511	0.523	0.555	0.601	**0.605**	0.601
	0.9	0.521	0.533	0.583	0.607	**0.617**	0.610
$\mathbb{E}[\hat{u}]$	0.6	0.992	**0.998**	0.904	0.930	0.918	0.946
	0.7	**0.998**	1.003	0.920	0.947	0.931	0.951
	0.8	**0.999**	1.006	0.936	0.958	0.939	0.953
	0.9	**0.998**	1.011	0.948	0.963	0.941	0.953
$\mathrm{Var}[\hat{u}]$	0.6	0.767	0.847	0.499	0.709	0.637	**0.835**
	0.7	0.799	0.875	0.604	0.828	0.732	**0.890**
	0.8	0.811	0.880	0.714	0.907	0.797	**0.918**
	0.9	0.803	0.868	0.810	**0.955**	0.838	0.930

Table 5.4: *Performance indexes obtained on* Stockton *by means of different filters applied in the absence (NW) and in the presence (W) of a whitening stage (best index values for each cutoff frequency are highlighted in bold).*

	f_c	Γ–MAP		GG MAP-S		PPB	
		NW	W	NW	W	NW	W
PSNR	0.6	20.20	21.64	18.20	23.18	21.23	**24.24**
	0.7	20.95	22.16	20.67	24.73	23.41	**24.78**
	0.8	21.56	22.42	22.88	**25.32**	24.36	25.00
	0.9	21.82	22.42	24.08	**25.48**	24.80	25.13
MSSIM	0.6	0.317	0.364	0.199	0.436	0.366	**0.492**
	0.7	0.343	0.384	0.300	**0.533**	0.450	0.516
	0.8	0.367	0.401	0.416	**0.567**	0.493	0.525
	0.9	0.380	0.408	0.486	**0.571**	0.515	0.529
$\mathbb{E}[\hat{u}]$	0.6	**0.995**	1.007	0.909	0.952	0.933	0.966
	0.7	**1.002**	1.015	0.928	0.972	0.947	0.972
	0.8	**1.005**	1.018	0.945	0.982	0.954	0.973
	0.9	**1.007**	1.018	0.964	0.986	0.957	0.968
$\mathrm{Var}[\hat{u}]$	0.6	0.760	0.842	0.490	0.744	0.666	**0.852**
	0.7	0.802	0.877	0.606	0.863	0.757	**0.894**
	0.8	0.824	0.894	0.712	**0.934**	0.811	0.911
	0.9	0.834	0.886	0.833	**0.966**	0.849	0.905

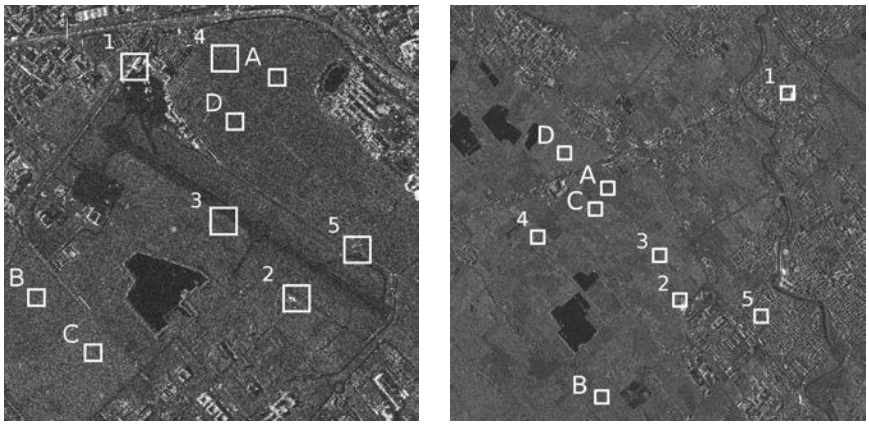

(a) (b)

Figure 5.3: *Original SLC SAR images:* Peretola *(a),* 1024×1024*, and* Campi Bisenzio *(b),* 2048×2048

based on reference image, i.e., $\mathbb{E}[\hat{u}]$ and $\mathrm{Var}[\hat{u}]$. The gain is particularly evident for $\mathrm{Var}[\hat{u}]$. In fact, all despeckling filters, in the presence of correlated noise, tend to underestimate the speckle–noise variance, so that their effectiveness in speckle removal is degraded.

5.5.3 Results on real SAR images

The results on true SAR data have been assessed by using two 16 bit, single–look complex images, extracted from 3–m resolution COSMO-SkyMed HImage Stripmap acquisitions. We used calibrated and focused in slant range-azimuth projection SAR data, referred to as *Level 1A SCS* product in the COSMO-SKyMed handbook [68]. The images represent two areas near Florence, Italy, denoted as *Peretola* and *Campi Bisenzio*, having dimensions 1024×1024 and 2048×2048, respectively. The images are shown in Figure 5.3.

Apart from the normalized autocorrelation $\rho(\mathbf{r})$, the values of ENL, $\mathbb{E}[\hat{u}]$, $\mathrm{Var}[\hat{u}]$, and Bias have been evaluated on four homogeneous areas manually selected in each of the two test images, whereas TCR has been computed on five patches containing point targets (the areas are indicated with squares in Figure 5.3). The size of the homogeneous areas are 40×40 and 64×64 for the images *Peretola* and *Campi Bisenzio*, respectively, whereas the TCR patches are 64×64 for both images.

In the case of real SAR images, it is interesting to evaluate the effectiveness of the whitening stage before despeckling, both in terms of decorrelation properties and preservation of radiometric features. In Figure 5.4, the fitting

of the periodograms computed on the COSMO-SkyMed images are shown. The results, presented for both the range and azimuth directions, demonstrate that a raised cosine function fits well the shape of the periodograms. It has to be noted that the periodograms of the original SAR data relative to the azimuth direction, shown in Figure 5.4-(b) and 5.4-(e), are affected by a frequency shift that has been compensated before fitting.

The normalized autocorrelation measured before and after applying the proposed whitening stage is shown in Tables 5.5 and 5.6, for *Peretola* and *Campi Bisenzio*, respectively. For both images, it is evident that the whitening approach effectively reduces speckle correlation.

As to the preservation of radiometric features, the values of TCR measured before and after the whitening stage, shown in Table 5.7, and the value of the bias, shown in Table 5.8, show that the whitening stage yields a good preservation of point targets and introduces only a small bias on homogeneous areas.

Table 5.5: *Values of* $\rho(\mathbf{r})$ *for* Peretola*, original image* $g(\mathbf{r})$ *and whitened image* $\hat{\sigma}_c(\mathbf{r})$.

	$g_c(\mathbf{r})$		$\hat{\sigma}_c(\mathbf{r})$	
	$r_x = 0$	$r_x = 1$	$r_x = 0$	$r_x = 1$
$r_y = 0$	1.000	0.296	1.000	0.044
$r_y = 1$	0.276	0.090	0.032	0.003

Table 5.6: *Values of* $\rho(\mathbf{r})$ *for* Campi Bisenzio*, original image* $g_c(\mathbf{r})$ *and whitened image* $\hat{\sigma}_c(\mathbf{r})$.

	$g_c(\mathbf{r})$		$\hat{\sigma}_c(\mathbf{r})$	
	$r_x = 0$	$r_x = 1$	$r_x = 0$	$r_x = 1$
$r_y = 0$	1.000	0.315	1.000	0.049
$r_y = 1$	0.302	0.103	0.034	0.004

Regarding the effect of the decorrelation approach on despeckling performance, the values of the ENL and the statistics of $\hat{u}$ evaluated on *Peretola* and *Campi Bisenzio* are reported in Table 5.9 and Table 5.10, respectively. We can observe that introducing the whitening stage always improves the ENL value for all the despeckling filters. The improvement is particularly significant for the GG MAP-S and the PPB filters.

As to the extracted speckle statistics, we note that the whitening stage has a beneficial effect as concerns $\mathrm{Var}[\hat{u}]$ that becomes quite close to the theoretical value for all despeckling filters. We observe also that the whitening

Table 5.7: *TCR values for original image $g_c(\mathbf{r})$ and whitened image $\hat{\sigma}_c(\mathbf{r})$.*

zone	*Peretola*		*Campi Bisenzio*	
	$g_c(\mathbf{r})$	$\hat{\sigma}_c(\mathbf{r})$	$g_c(\mathbf{r})$	$\hat{\sigma}_c(\mathbf{r})$
1	31.22	31.08	26.95	26.78
2	34.10	34.33	31.25	31.28
3	11.90	11.37	10.88	10.52
4	11.27	11.27	22.37	22.48
5	23.63	23.76	24.94	24.89

Table 5.8: *Bias (*dB*) measured between the original and the whitened image.*

zone	*Peretola*	*Campi Bisenzio*
A	-0.25	-0.14
B	-0.60	-0.31
C	-0.55	0.05
D	-0.44	-0.29

stage produces also a small increment of $\mathbb{E}[\hat{u}]$: while this fact tends to degrade the performance of the Γ-MAP filter, it usually compensates the bias affecting the GG MAP-S and PPB filters when applied without the whitening stage.

For a visual inspection, some results of the filtering are shown in Figure 5.5 and Figure 5.6. Specifically, a 512×512 detail of the two COSMO-SkyMed images is presented, together with the whitened image and the images filtered with the GG MAP-S and the PPB filters in the W and NW cases. As can be observed, the whitening stage produces a significant improvement of the visual quality of the filtered images. Even though some blurring can be noticed in Figure 5.6-(f), it is interesting to note that the whitened image shown in Figure 5.6-(b) still preserves all the details of the original image shown in Figure 5.6-(a), so that blurring has to be ascribed to the despeckling filter applied after the whitening stage.

As to the computational complexity, a MATLAB® implementation on an Intel® Core™2 Quad 2.0 GHz processor with 8 GB RAM performs the whitening step in about 4.7 seconds for the 2048×2048 *Campi Bisenzio* image. Such time is negligible with respect to the despeckling step, which on the same image requires about 240 seconds for the GG MAP-S filter and 1560 seconds for the PPB filter.

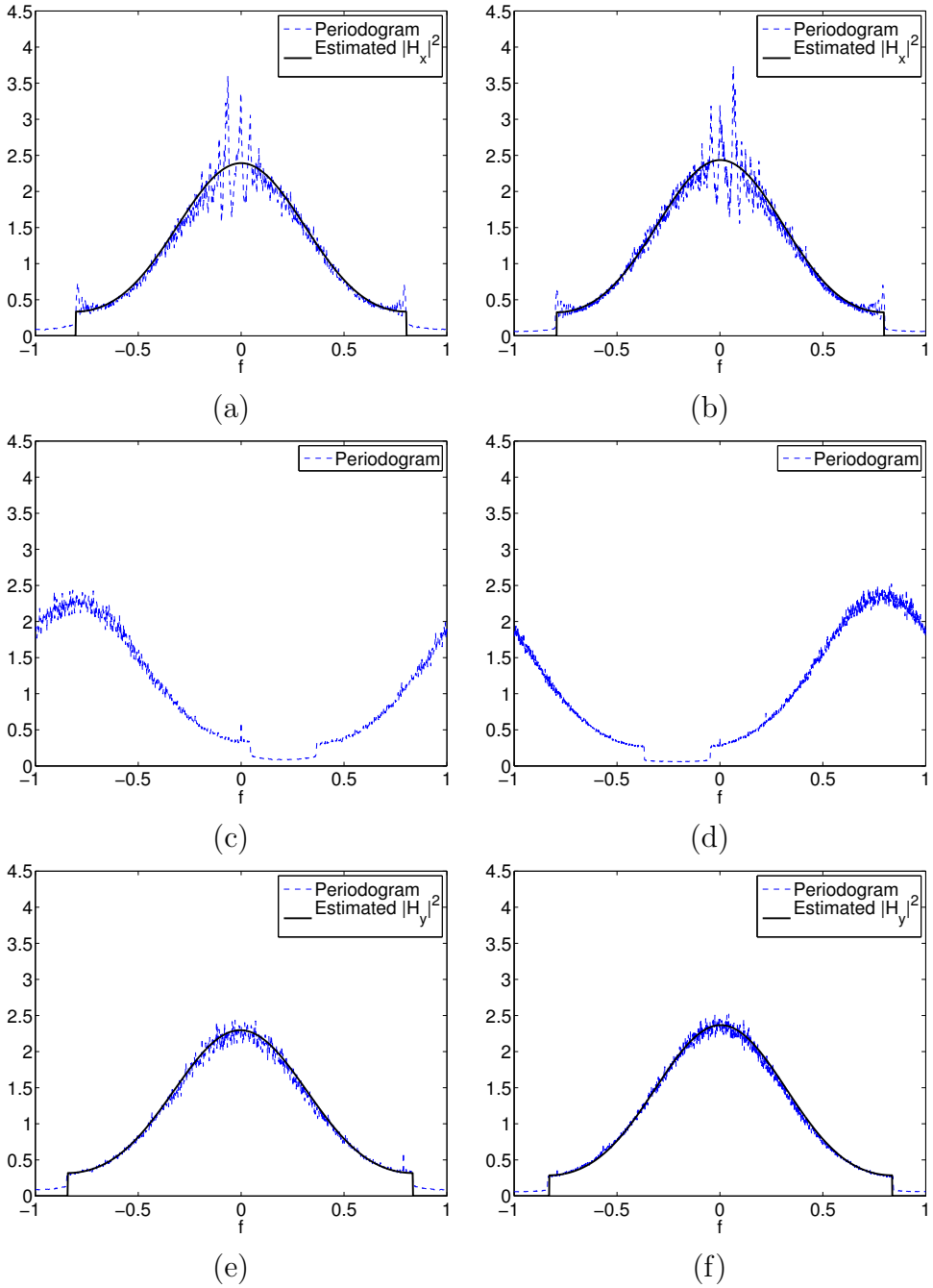

Figure 5.4: *Periodograms of* Peretola *(left) and* Campi Bisenzio *(right) and relative estimation of* $|H(\mathbf{f})|^2$*: along range (a),(b); along azimuth (c),(d) ; along azimuth after frequency shifting recovery (e),(f).*

Table 5.9: *Performance indexes obtained on* Peretola *(best index values are highlighted in bold).*

	zone	Γ–MAP		GG MAP-S		PPB	
		NW	W	NW	W	NW	W
ENL	A	19.27	24.64	27.90	142.29	78.44	**153.19**
	B	17.75	29.87	19.26	**184.24**	60.76	150.21
	C	18.03	29.17	30.52	329.48	90.91	**224.91**
	D	20.86	24.94	27.62	**196.06**	118.28	173.17
$\mathbb{E}[\hat{u}]$	A	**1.005**	1.033	0.940	0.997	0.921	0.979
	B	**0.989**	1.080	0.929	1.052	0.929	1.037
	C	**1.008**	1.092	0.964	1.070	0.962	1.062
	D	**1.002**	1.111	0.950	1.069	0.967	1.069
$\mathrm{Var}[\hat{u}]$	A	0.847	0.928	0.702	**0.936**	0.740	0.887
	B	0.844	1.063	0.684	1.087	0.767	**1.021**
	C	0.804	0.975	0.707	1.036	0.761	**0.985**
	D	0.788	0.972	0.661	**0.994**	0.749	0.962

Table 5.10: *Performance indexes obtained on* Campi Bisenzio *(best index values are highlighted in bold).*

	zone	Γ–MAP		GG MAP-S		PPB	
		NW	W	NW	W	NW	W
ENL	A	12.53	20.71	15.21	83.57	37.86	**90.58**
	B	12.12	18.87	22.07	105.50	68.28	**98.03**
	C	16.73	24.88	24.87	**243.45**	82.78	146.27
	D	14.40	15.18	22.45	123.23	79.52	**126.68**
$\mathbb{E}[\hat{u}]$	A	1.012	1.035	0.944	**1.003**	0.959	0.984
	B	**1.018**	1.091	0.947	1.045	0.956	1.042
	C	**1.002**	1.017	0.949	0.991	0.971	0.972
	D	**1.003**	1.064	0.943	1.032	0.958	1.028
$\mathrm{Var}[\hat{u}]$	A	0.842	0.939	0.681	**0.965**	0.802	0.904
	B	0.879	1.070	0.731	1.100	0.834	**1.052**
	C	0.808	0.887	0.699	**0.931**	0.808	0.864
	D	0.801	0.939	0.682	**1.001**	0.784	0.972

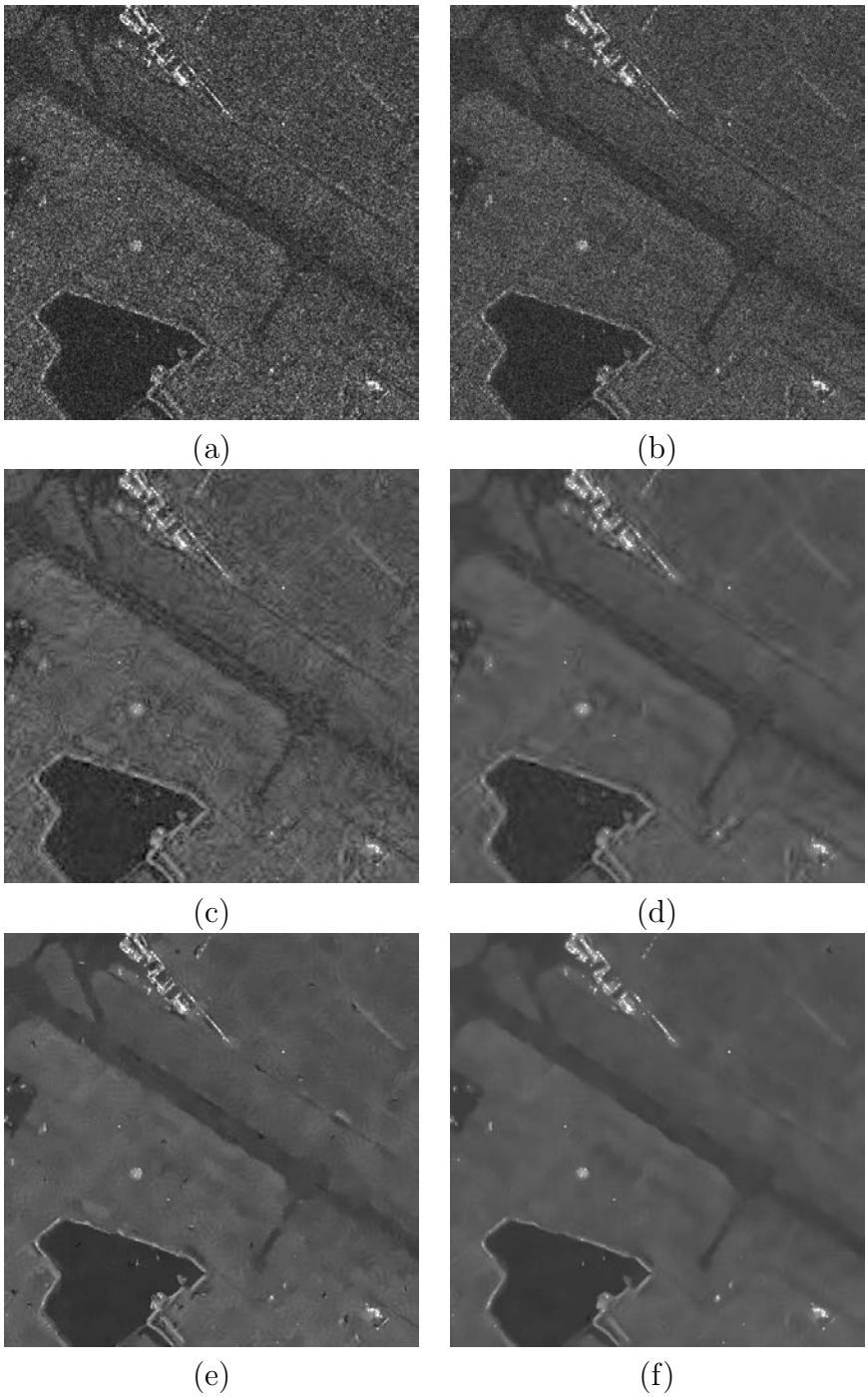

Figure 5.5: Peretola, *left to right, top to bottom: original detail (a); after the whitening stage (b); GG MAP-S filtering obtained in the NW (c) and W (d) cases; PPB filtering obtained in the NW (e) and W (f) cases.*

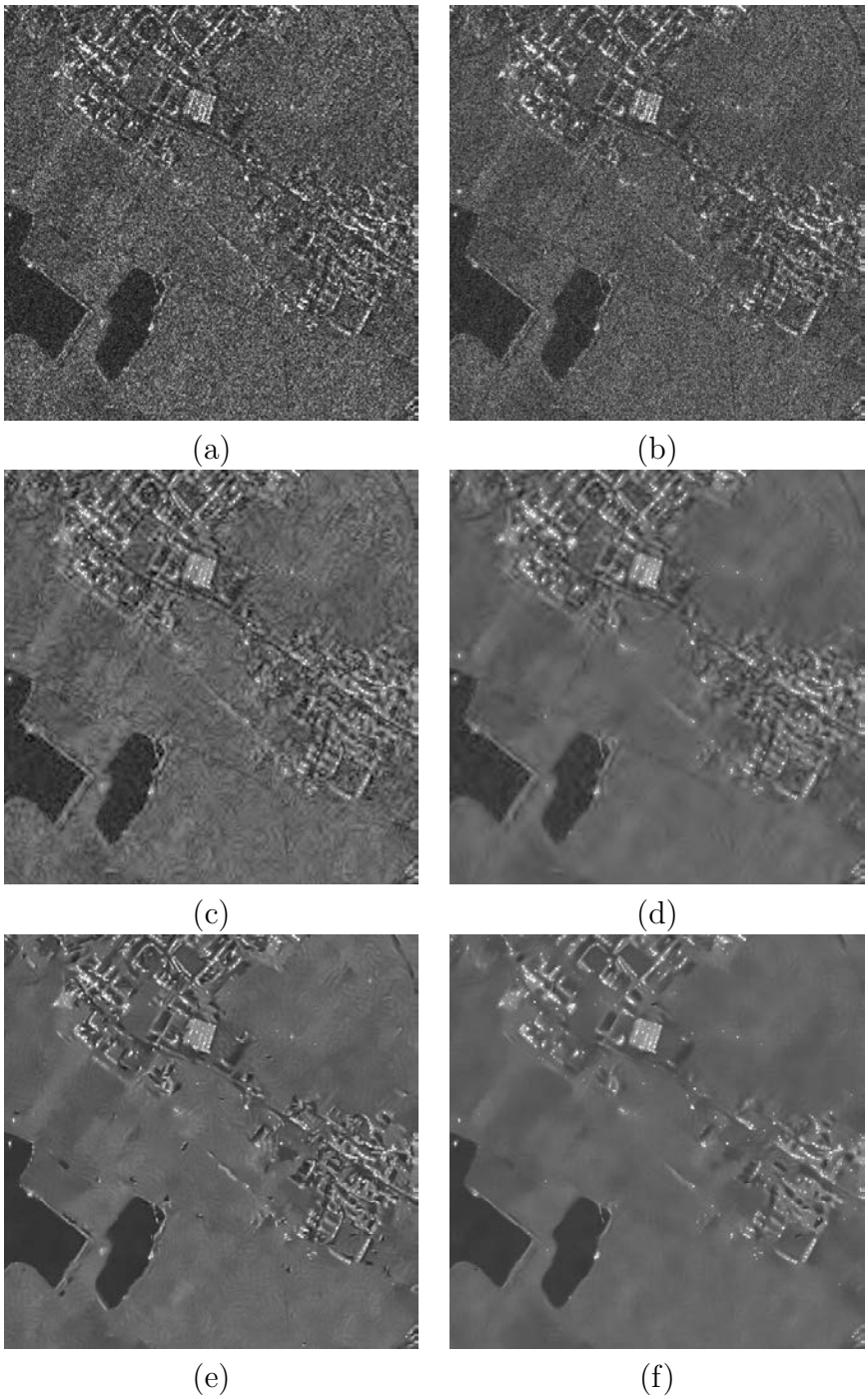

Figure 5.6: Campi Bisenzio, *left to right, top to bottom: original detail (a); after the whitening stage (b); GG MAP-S filtering obtained in the NW (c) and W (d) cases; PPB filtering obtained in the NW (e) and W (f) cases.*

5.6 Conclusions

In this chapter, the problem of despeckling single–look complex SAR images affected by correlated noise has been addressed. Several despeckling filters in the literature have been developed under the hypothesis of white speckle noise, so that they suffer from a significant loss of performance when used in the correlated speckle case. We have demonstrated that this is not the case if a whitening stage, restoring the hypothesis of whiteness on the single–look complex image, is introduced before filtering. The motivation of the whitening stage has been formally derived by using classical and Bayesian estimation frameworks. Specifically, it has been shown that estimators can be derived equivalently in the correlated and whitened domain, and that the approach is optimal if the SAR system has an invertible transfer function.

Based on Madsen's work, a robust estimation of the SAR system point spread function, relying only upon the acquired single–look complex SAR image, has been proposed; practical implementation issues, such as the treatment of point targets, has been faced as well. The experimental results confirm that despeckling filters based on the uncorrelated speckle assumption can be successfully applied also in the correlated speckle case when the proposed procedure is applied. Interestingly, a significant performance gain is obtained even when a perfect whitening of the single–look SAR image can not be achieved, for example when the SAR system frequency response is zero in some interval. Results on true SAR images also demonstrate that the proposed decorrelation technique adequately preserves radiometric features.

5.7 Appendix

5.7.1 CRLB and efficient estimators of $\boldsymbol{\sigma}$

In order to prove the efficiency of the whitening stage, we firstly derive the CRLB for the estimation of the target scene $\boldsymbol{\sigma} = [\sigma(0) \cdots \sigma(N-1)]^T$ given the observation of $\mathbf{g_c}$ expressed by (5.7). Since $\mathbf{g_c}$ is a zero-mean Gaussian vector, the Fisher information matrix $\mathbf{I}_{\mathbf{g_c}}(\boldsymbol{\sigma})$ relative to any estimator of $\boldsymbol{\sigma}$ is given by [25]

$$[\mathbf{I}_{\mathbf{g_c}}(\boldsymbol{\sigma})]_{n,m} = \frac{1}{2}\mathrm{tr}\left[\mathbf{C}_{\mathbf{g_c}}{}^{-1}\frac{\partial \mathbf{C}_{\mathbf{g_c}}}{\partial \sigma(n)}\mathbf{C}_{\mathbf{g_c}}{}^{-1}\frac{\partial \mathbf{C}_{\mathbf{g_c}}}{\partial \sigma(m)}\right] \tag{5.54}$$

where, from (5.11), we have

$$\begin{aligned} {\mathbf{C}_{\mathbf{g_c}}}^{-1} &= \mathbf{H}^{-T}{\mathbf{C}_{\sigma_\mathbf{c}}}^{-1}\mathbf{H}^{-1} \\ \frac{\partial \mathbf{C}_{\mathbf{g_c}}}{\partial \sigma(p)} &= \mathbf{H}\frac{\partial \mathbf{C}_{\sigma_\mathbf{c}}}{\partial \sigma(p)}\mathbf{H}^{T} \end{aligned} \tag{5.55}$$

for $0 \leq p < N$. From (5.10) we get

$$\begin{aligned} {\mathbf{C}_{\sigma_\mathbf{c}}}^{-1} &= 2 \cdot \operatorname{diag}\left(\left[\boldsymbol{\sigma}^T, \boldsymbol{\sigma}^T\right]^T\right)^{-1} \\ \left[\frac{\partial \mathbf{C}_{\sigma_\mathbf{c}}}{\partial \sigma(p)}\right]_{n,m} &= \begin{cases} \frac{1}{2}, & \text{for } m = n = p, m = n = p + N, \\ 0, & \text{otherwise.} \end{cases} \end{aligned} \tag{5.56}$$

In (5.55), both $\mathbf{H}$ and $\mathbf{C}_{\sigma_\mathbf{c}}$ are required to be invertible; while the former condition is strictly dependent on the the expression given in (5.9), the latter one is always verified if $\boldsymbol{\sigma}$ has no zero entries. Hence, substituting (5.55) into (5.54) yields

$$\begin{aligned} \left[\mathbf{I}_{\mathbf{g_c}}(\boldsymbol{\sigma})\right]_{n,m} =& \frac{1}{2}\operatorname{tr}\left[\mathbf{H}^{-T}{\mathbf{C}_{\sigma_\mathbf{c}}}^{-1}\mathbf{H}^{-1}\mathbf{H}\frac{\partial \mathbf{C}_{\sigma_\mathbf{c}}}{\partial \sigma(n)}\mathbf{H}^{T}\right. \\ & \left. \times\, \mathbf{H}^{-T}{\mathbf{C}_{\sigma_\mathbf{c}}}^{-1}\mathbf{H}^{-1}\mathbf{H}\frac{\partial \mathbf{C}_{\sigma_\mathbf{c}}}{\partial \sigma(m)}\mathbf{H}^{T}\right] \\ =& \frac{1}{2}\operatorname{tr}\left[\mathbf{H}^{-T}{\mathbf{C}_{\sigma_\mathbf{c}}}^{-1}\frac{\partial \mathbf{C}_{\sigma_\mathbf{c}}}{\partial \sigma(n)}{\mathbf{C}_{\sigma_\mathbf{c}}}^{-1}\frac{\partial \mathbf{C}_{\sigma_\mathbf{c}}}{\partial \sigma(m)}\mathbf{H}^{T}\right] \\ =& \frac{1}{2}\operatorname{tr}\left[\mathbf{H}^{T}\mathbf{H}^{-T}{\mathbf{C}_{\sigma_\mathbf{c}}}^{-1}\frac{\partial \mathbf{C}_{\sigma_\mathbf{c}}}{\partial \sigma(n)}{\mathbf{C}_{\sigma_\mathbf{c}}}^{-1}\frac{\partial \mathbf{C}_{\sigma_\mathbf{c}}}{\partial \sigma(m)}\right] \\ =& \frac{1}{2}\operatorname{tr}\left[{\mathbf{C}_{\sigma_\mathbf{c}}}^{-1}\frac{\partial \mathbf{C}_{\sigma_\mathbf{c}}}{\partial \sigma(n)}{\mathbf{C}_{\sigma_\mathbf{c}}}^{-1}\frac{\partial \mathbf{C}_{\sigma_\mathbf{c}}}{\partial \sigma(m)}\right] \end{aligned} \tag{5.57}$$

where the property $\operatorname{tr}(\mathbf{AB}) = \operatorname{tr}(\mathbf{BA})$ has been used in the third equality. Furthermore, from (5.56), it follows that

$$\begin{aligned} &\left[{\mathbf{C}_{\sigma_\mathbf{c}}}^{-1}\frac{\partial \mathbf{C}_{\sigma_\mathbf{c}}}{\partial \sigma(p)}\right]_{n,m} \\ &\qquad = \begin{cases} \sigma^{-1}(p), & \text{for } m = n = p, m = n = p + N, \\ 0, & \text{otherwise} \end{cases} \end{aligned} \tag{5.58}$$

that is, such an $N \times N$ matrix has all zero entries but in the pth and $(N+p)$th positions of the main diagonal. Consequently, for $p \neq q$ we have

$$\mathbf{C}_{\sigma_\mathbf{c}}{}^{-1} \frac{\partial \mathbf{C}_{\sigma_\mathbf{c}}}{\partial \sigma(p)} \mathbf{C}_{\sigma_\mathbf{c}}{}^{-1} \frac{\partial \mathbf{C}_{\sigma_\mathbf{c}}}{\partial \sigma(q)} = \mathbf{0} \tag{5.59}$$

whereas for $p = q$ we have

$$\left[\mathbf{C}_{\sigma_\mathbf{c}}{}^{-1} \frac{\partial \mathbf{C}_{\sigma_\mathbf{c}}}{\partial \sigma(p)} \mathbf{C}_{\sigma_\mathbf{c}}{}^{-1} \frac{\partial \mathbf{C}_{\sigma_\mathbf{c}}}{\partial \sigma(p)} \right]_{n,m} = \begin{cases} \sigma^{-2}(p), & \text{for } m = n = p, m = n = p + N, \\ 0, & \text{otherwise.} \end{cases} \tag{5.60}$$

Substituting relations (5.59) and (5.60) into (5.57) yields

$$[\mathbf{I}_{\mathbf{g_c}}(\boldsymbol{\sigma})]_{n,m} = \begin{cases} \sigma^{-2}(n) & n = m \\ 0 & \text{otherwise} \end{cases} \tag{5.61}$$

or, more compactly,

$$\mathbf{I}_{\mathbf{g_c}}(\boldsymbol{\sigma}) = \operatorname{diag}(\boldsymbol{\sigma})^{-2} \tag{5.62}$$

By applying the CRLB theorem [25], the covariance matrix $\mathbf{C}_{\hat{\boldsymbol{\sigma}}}$ of every unbiased estimator $\hat{\boldsymbol{\sigma}}$ of $\boldsymbol{\sigma}$ satisfies

$$\mathbf{C}_{\hat{\boldsymbol{\sigma}}} - \mathbf{I}_{\mathbf{g_c}}{}^{-1}(\boldsymbol{\sigma}) \geq \mathbf{0} \tag{5.63}$$

where equality holds if the estimator is efficient. Hence, substituting (5.62) into the last inequality yields the explicit expression of the CRLB of the despeckling problem given in (5.12).

Now, we demonstrate that the estimator in (5.14) is efficient. It is straightforward to show that $\hat{\boldsymbol{\sigma}}_{\text{eff}}$ is unbiased, that is (for the sake of clearness, vector entries are indicated by a subscript index)

$$\begin{aligned} \mathbb{E}\left\{[\hat{\boldsymbol{\sigma}}_{\text{eff}}]_n\right\} &= \mathbb{E}\left\{ \left| \left[\mathbf{H}^{-1}\mathbf{g_c}\right]_n \right|^2 + \left| \left[\mathbf{H}^{-1}\mathbf{g_c}\right]_{n+N} \right|^2 \right\} \\ &= \mathbb{E}\left\{ \left| [\boldsymbol{\sigma_c}]_n \right|^2 \right\} + \mathbb{E}\left\{ \left| [\boldsymbol{\sigma_c}]_{n+N} \right|^2 \right\} \\ &= [\boldsymbol{\sigma}]_n / 2 + [\boldsymbol{\sigma}]_n / 2 = [\boldsymbol{\sigma}]_n \end{aligned} \tag{5.64}$$

where equation (5.7) and the statistical model (5.10) have been used in the

second and third equality, respectively. Similarly, it can be shown that

$$\begin{aligned}
&\mathbb{E}\left\{\left|\left[\mathbf{H}^{-1}\mathbf{g_c}\right]_p\right|^2\left|\left[\mathbf{H}^{-1}\mathbf{g_c}\right]_q\right|^2\right\}\\
&\quad=\mathbb{E}\left\{\left|\left[\boldsymbol{\sigma_c}\right]_p\right|^2\left|\left[\boldsymbol{\sigma_c}\right]_q\right|^2\right\}\\
&\quad=\begin{cases}\mathbb{E}\left\{\left|\left[\boldsymbol{\sigma_c}\right]_p\right|^2\right\}\cdot\mathbb{E}\left\{\left|\left[\boldsymbol{\sigma_c}\right]_q\right|^2\right\} & ,p\neq q\\ \mathbb{E}\left\{\left|\left[\boldsymbol{\sigma_c}\right]_p\right|^4\right\} & ,p=q\end{cases}\\
&\quad=\begin{cases}\left[\boldsymbol{\sigma}\right]_p\left[\boldsymbol{\sigma}\right]_q/4 & ,p\neq q\\ 3\cdot\left|\left[\boldsymbol{\sigma}\right]_p\right|^2/4 & ,p=q,\end{cases}
\end{aligned}\tag{5.65}$$

where we have exploited the fact that the entries of $\boldsymbol{\sigma_c}$ are independent Gaussian variables. By using the last expression, each entry of the autocorrelation matrix of $\hat{\boldsymbol{\sigma}}_{\text{eff}}$, $\mathbf{R}_{\hat{\boldsymbol{\sigma}}_{\text{eff}}}$, is given by

$$\begin{aligned}
\left[\mathbf{R}_{\hat{\boldsymbol{\sigma}}_{\text{eff}}}\right]_{n,m}&=\mathbb{E}\left\{\left[\hat{\boldsymbol{\sigma}}_{\text{eff}}\right]_n\left[\hat{\boldsymbol{\sigma}}_{\text{eff}}\right]_m\right\}\\
&=\mathbb{E}\left\{\left[\left|\left[\mathbf{H}^{-1}\mathbf{H}\boldsymbol{\sigma_c}\right]_n\right|^2+\left|\left[\mathbf{H}^{-1}\mathbf{H}\boldsymbol{\sigma_c}\right]_{n+N}\right|^2\right]\right.\\
&\quad\left.\cdot\left[\left|\left[\mathbf{H}^{-1}\mathbf{H}\boldsymbol{\sigma_c}\right]_m\right|^2+\left|\left[\mathbf{H}^{-1}\mathbf{H}\boldsymbol{\sigma_c}\right]_{m+N}\right|^2\right]\right\}\\
&=\begin{cases}\left[\boldsymbol{\sigma}\right]_n\left[\boldsymbol{\sigma}\right]_m & ,m\neq n\\ 2\cdot\left|\left[\boldsymbol{\sigma}\right]_n\right|^2 & ,m=n.\end{cases}
\end{aligned}\tag{5.66}$$

The covariance matrix of $\hat{\boldsymbol{\sigma}}_{\text{eff}}$, $\mathbf{C}_{\hat{\boldsymbol{\sigma}}_{\text{eff}}}$, obtained by its definition and (5.66), is given by

$$\left[\mathbf{C}_{\hat{\boldsymbol{\sigma}}_{\text{eff}}}\right]_{n,m}=\left[\mathbf{R}_{\hat{\boldsymbol{\sigma}}_{\text{eff}}}\right]_{n,m}-\left[\boldsymbol{\sigma}\right]_n\left[\boldsymbol{\sigma}\right]_m=\begin{cases}0 & ,m\neq n\\ \left|\left[\boldsymbol{\sigma}\right]_n\right|^2 & ,m=n,\end{cases}\tag{5.67}$$

or, in compact form,

$$\mathbf{C}_{\hat{\boldsymbol{\sigma}}_{\text{eff}}}=\operatorname{diag}\left(\boldsymbol{\sigma}\right)^2.\tag{5.68}$$

By replacing $\mathbf{C}_{\hat{\boldsymbol{\sigma}}}$ with $\mathbf{C}_{\hat{\boldsymbol{\sigma}}_{\text{eff}}}$ in (5.12), the equality is verified; thus $\hat{\boldsymbol{\sigma}}_{\text{eff}}$ is an efficient estimator for the despeckling problem.

5.7.2 Pseudo-inverse of $H(\mathbf{f})$.

Let us rewrite the model in (5.1) in complex vector notation as

$$\tilde{\mathbf{g}}_{\mathbf{c}} = \tilde{\mathbf{H}}\tilde{\boldsymbol{\sigma}}_{\boldsymbol{c}} \tag{5.69}$$

where $\tilde{\mathbf{g}}_{\mathbf{c}} = [g_c(0), \ldots, g_c(N-1)]^T$ and $\tilde{\boldsymbol{\sigma}}_{\boldsymbol{c}} = [\sigma_c(0), \ldots, \sigma_c(N-1)]^T$ whereas $\tilde{\mathbf{H}}$ models 2-D convolution by $h(\mathbf{r})$. When the matrix $\tilde{\mathbf{H}}$ has not full rank, it is well known that the minimum ℓ^2 norm solution of (5.69) is given by

$$\hat{\tilde{\boldsymbol{\sigma}}}_{\boldsymbol{c}} = \tilde{\mathbf{H}}^{\dagger}\tilde{\mathbf{g}}_{\mathbf{c}} \tag{5.70}$$

where $\tilde{\mathbf{H}}^{\dagger}$ denotes the Moore-Penrose pseudo-inverse of $\tilde{\mathbf{H}}$ [69].

In the case of a circular 2-D convolution, the matrix $\tilde{\mathbf{H}}$ is block circulant and can be diagonalized using a unitary 2-D discrete Fourier transform (DFT) matrix $\mathbf{W}_{2D}$ [70], that is

$$\tilde{\mathbf{H}} = \mathbf{W}_{2D}^{H}\boldsymbol{\Lambda}_{\mathbf{H}}\mathbf{W}_{2D} \tag{5.71}$$

where $\boldsymbol{\Lambda}_{\mathbf{H}}$ is a diagonal matrix whose diagonal contains the 2-D DFT of $h(\mathbf{r})$, rearranged by stacking its columns. If we assume that $H(\mathbf{f})$ is different from zero only on a given passband, this can be expressed as

$$\tilde{\mathbf{H}} = \mathbf{W}_{2D,P}^{H}\boldsymbol{\Lambda}_{\mathbf{H},P}\mathbf{W}_{2D,P} \tag{5.72}$$

where $\boldsymbol{\Lambda}_{\mathbf{H},P}$ is a diagonal matrix obtained by removing the zero diagonal elements from $\boldsymbol{\Lambda}_{\mathbf{H}}$ and $\mathbf{W}_{2D,P}$ is obtained by removing the corresponding columns from $\mathbf{W}_{2D}$. In this case, the Moore-Penrose pseudo-inverse of $\tilde{\mathbf{H}}$ is readily found as

$$\tilde{\mathbf{H}}^{\dagger} = \mathbf{W}_{2D,P}^{H}\boldsymbol{\Lambda}_{\mathbf{H},P}^{-1}\mathbf{W}_{2D,P}. \tag{5.73}$$

Hence, the above formula shows that equation (5.25) is equivalent to computing the minimum norm solution of the whitening problem.

Chapter 6

Quality assessment of despeckling methods

In this chapter, the non–trivial task of quality assessment for the despeckling filters is discussed. In the first part a review of the most popular indexes used in the literature is presented; such list includes also measures which have been used in the previous chapters. In the second part, a fully automatic method for quality assessment of despeckled SAR images is proposed; such a method does not require a reference image to be computed.

6.1 Overview

One of the most challenging tasks is the validation and quality assessment of data processed for speckle reduction. The most evident problem is that the noise-free reflectivity that we wish to estimate is unknown, so that no comparison can be carried out between the output of the despeckling process and the actual *ground truth*. Another important issue is the relationship between quality and fidelity of despeckled SAR data. Like many other denoising frameworks, the quality of a processed SAR image is usually evaluated in terms of blurring of homogeneous areas, i.e., suppression of speckle noise, and detail preservation in heterogeneous areas. Nonetheless, in incoherent SAR imagery, a fundamental part of the information is represented by the relative values of the reflectivity of the targets, which allow measurements and inferences on the target scene. The radiometric preservation of the signal is an important requirement, that is, a good despeckling filter should not introduce bias on the reflectivity.

An immediate and subjective approach for quality assessment is represented by visual inspection of filtered images. Visual inspection permits

detection of the main *human–visible* features that characterize the behaviour of a despeckling filter. Such features include edge preservation capability, degree of blur, point target preservation, as well as structural artifacts which are hardly detected by objective and direct measurements. On the other hand, visual assessment does not allow either quantitative comparisons between the performances of different despeckling filters to be made or the bias introduced by the filter to be effectively estimated.

In order to overcome the limitations of visual comparison, several objective performance indexes have been proposed in the literature for the quality assessment of despeckling filters. They can be mainly divided into two classes: *with–reference* and *without–reference* indexes.

With–reference indexes are commonly used in the image denoising field. Their use implies that the noise–free, or *reference*, image is known. A typical approach consists in choosing a reference image, either optical or synthetic, representing the actual reflectivity or *ground–truth*, and creating a *synthetically* degraded version according to a given signal model. These indexes permit a quantitative and objective comparison between the performances of different filters, which are expected to perform similarly on real SAR images. Moreover, insights on filters behaviour on specific image features, like edge preservation and homogeneous areas smoothing, can be easily highlighted by choosing appropriate reference images and even synthetic–generated patterns. Unfortunately, experimental results carried out on simulated SAR images often are not sufficient to infer the performances of despeckling filters on real SAR images, since the synthetically speckled image may not be consistent with the actual SAR image formation and acquisition processes. Furthermore, the statistical properties of the chosen reference image and of a real ground–truth reflectivity can substantially differ.

On the contrary, without–reference indexes do not trust on the knowledge of the ground–truth. They are uniquely based on specific statistical hypotheses on the signal model. Since the signal model is strongly dependent on the degree of scene heterogeneity, a supervised selection of the most appropriate areas for the computation of a specific index, e.g., homogeneous areas, may be required.

In the following, the most used indexes belonging to both the above mentioned classes are presented. Note that the statistical operator of expectation $E[\cdot]$ and the moments of the involved variables, such as the variance and covariance, here denoted as $\mathrm{Var}[\cdot]$ and $\mathrm{Cov}[\cdot]$ for the sake of simplicity, should be replaced by their empirical versions based on spatial averages when evaluating the indexes.

6.1.1 With–reference indexes

The mean square error (MSE), or Euclidean distance, between the ground–truth f and the despeckled image $\hat{f}$, defined as

$$\mathrm{MSE}(f, \hat{f}) = \mathrm{E}[(\hat{f} - f)^2], \tag{6.1}$$

has been widely used for the quality assessment of both denoising and despeckling [71]. Other common related measurements are the *Signal–To–Noise Ratio* (SNR) [22]

$$\mathrm{SNR}(f, \hat{f}) = 10 \cdot \log_{10} \left[\frac{\mathrm{Var}[f]}{\mathrm{MSE}(f, \hat{f})} \right], \tag{6.2}$$

the *Signal–to–Mean Square Error* (SMSE) [72]

$$\mathrm{SMSE}(f, \hat{f}) = 10 \cdot \log_{10} \left[\frac{\mathrm{E}[f^2]}{\mathrm{MSE}(f, \hat{f})} \right], \tag{6.3}$$

and the *Peak Signal–To–Noise Ratio* (PSNR) [41]

$$\mathrm{PSNR}(f, \hat{f}) = 10 \cdot \log_{10} \left[\frac{f_{\mathrm{PEAK}}^2}{\mathrm{MSE}(f, \hat{f})} \right]. \tag{6.4}$$

where f_{PEAK} denotes the maximum value allowed by the samples dynamic range. Unlike the case of additive signal–independent noise, in the presence of signal–dependent noise the MSE is strongly influenced by the average signal level of the ground truth. Consequently, a quantitative evaluation of despeckling filters using this kind of indexes is strongly dependent on the content of the ground–truth image, even though performance hierarchy is usually preserved across different images.

MSE–based measurements are useful to obtain a global performance assessment on the whole image, but usually they yield little information about the preservation of specific features, for which other indexes can be used. The *mean structural similarity index measurement* (MSSIM) [58], proposed for the general denoising framework and adopted also in the context of despeckling, underlines the perceived changes in structural information varia-

tion after the filtering process. The MSSIM is defined as

$$\begin{aligned}\mathrm{MSSIM} =& \frac{1}{M}\sum_{p=0}^{M-1}\left[\frac{2\cdot \mathrm{E}\left[f_p\right]\cdot \mathrm{E}\left[\hat{f}_p\right]+C_1}{\mathrm{E}\left[f_p^2\right]+\mathrm{E}\left[\hat{f}_p^2\right]+C_1}\right. \\ & \left.\cdot\frac{2\cdot \mathrm{Cov}\left[f_p,\hat{f}_p\right]+C_2}{\mathrm{Var}\left[f_p\right]+\mathrm{Var}\left[\hat{f}_p\right]+C_2}\right],\end{aligned} \tag{6.5}$$

where f_p and $\hat{f}_p$, $p = 0, \ldots, M-1$, represent two corresponding patches in the original image and in the despeckled one, respectively, and C_1, C_2 are two suitable constants. MSSIM takes values over the interval $[0, 1]$, where 0 and 1 indicate no structural similarity and perfect similarity, respectively. As demonstrated in [58], MSSIM can substantially differ between images having very similar MSE values.

The *edge correlation* (EC) index has been proposed as a measure of edge preservation for despeckling of echographic images [73] and has been extended to the SAR field [74]; it is defined as the correlation coefficient ($0 \leq \mathrm{EC} \leq 1$) between highpass versions of the original image f^H and despeckled one $\hat{f}^H$, that is

$$\mathrm{EC} = \frac{\mathrm{Cov}\left[f^H, \hat{f}^H\right]}{\sqrt{\mathrm{Var}\left[f^H\right]\cdot \mathrm{Var}\left[\hat{f}^H\right]}}. \tag{6.6}$$

This index may be distorted by possible residual speckle noise that is enhanced by the highpass filtering.

Another index of edge preservation is Pratt's *figure of merit* (FOM) [75], which has been used in [76] for the quality assessment of despeckled SAR and ultrasound images. FOM is defined on a local patch of the image containing an edge as

$$\mathrm{FOM} = \frac{1}{\max(\hat{N}, N)}\sum_{n=1}^{\hat{N}}\frac{1}{1+d_n^2\alpha}, \tag{6.7}$$

where N and $\hat{N}$ are the points belonging to the edge in the original and despeckled patches, respectively; d_n^2 is the Euclidean distance between the edge pixel in the despeckled image patch and the nearest ideal edge pixel in the original one, and α is a suitable constant. The more similar the edge maps, the closer to zero the FOM values. Consequently, this index is strictly related to the map edge detector that is used, which is crucial especially for the despeckled image when a residual noise component is present.

Table 6.1 summarizes the above mentioned indexes.

In order to show despeckling how filters' performances are measured by the previous indexes, in the following we present some experimental results. A synthetically speckled images has been produced starting from a 512×512 digitized aerial photograph of San Francisco. Firstly, the original speckle-free image, regarded as an amplitude format, has been squared and multiplied by an exponentially distributed fading term, in order to simulate a single-look SAR image in intensity format. The simulated speckle is spatially uncorrelated and fully developed. The noisy intensity image, together with all filtered intensity versions, has been square rooted, for displaying convenience, and is shown together with the 8-bit original, regarded as an amplitude image, in Fig. 6.1-(b) and Fig. 6.1-(a), respectively.

The filters compared here are representative of different approaches : GG MAP-S [41] and LG MAP-S (Section 3.3.2) as Bayesian filters in the wavelet domain (input format is square root of intensity); Probability Patch–Based (PPB) [57] and SAR–BM3D [77] as non–local mean filters in the spatial and wavelet domain. Visual comparisons of the results obtained with the same filters can be made observing Fig. 6.1. Clearly, all filters fail to reconstruct the textured area in the bottom-right of the image. Performance indexes obtained by means of the test despeckling filters are reported in Table 6.2. Interestingly, There is no filter leading in all indexes. Moreover, there is no common trend between the EC and the FOM indexes which are supposed to measure similar features.

A second set of experiments have been carried out by simulating a 4–look SAR image in intensity format, that is, by multiplying the original speckle-free image by a unitary variance Γ distributed fading term having variance 1/4. Results are reported in Table 6.3. Results are quite aligned with those ones obtained in the case of the single–look speckle realization. The only exception is represented by the GG MAP-S filter which scored the best in terms of FOM in the previous case.

6.1.2 Without–reference indexes

As previously stated, without–reference indexes do not rely on the complete knowledge of the true reflectivity, but are based on the statistical model of the SAR signal as well as on some simple assumptions and the degree of heterogeneity of the underlying scene.

The *equivalent number of look* (ENL) [78] is an index suitable for evaluating the level of smoothing in homogeneous areas, that is where the scene variation is supposed to be negligible with respect to speckle noise fluctua-

Table 6.1: *List of commonly used with-reference indexes for evaluating performances of despeckling algorithms.*

Index	Note
$\mathrm{MSE} = \mathrm{E}[(\hat{f} - f)^2]$	f, $\hat{f}$: speckle–free despeckled images
$\mathrm{SNR} = 10 \cdot \log_{10}\left[\frac{\mathrm{Var}[f]}{\mathrm{MSE}}\right]$	$\mathrm{Var}[f]$: speckle–free image variance
$\mathrm{PSNR} = 10 \cdot \log_{10}\left[\frac{f_{\mathrm{PEAK}}^2}{\mathrm{MSE}}\right]$	f_{PEAK}: maximum value allowed by the samples dynamic range
$\mathrm{SMSE} = 10 \cdot \log_{10}\left[\frac{\mathrm{E}[f^2]}{\mathrm{MSE}}\right]$	$\mathrm{E}[f^2]$: speckle–free image power
$\mathrm{MSSIM} = \frac{1}{M}\sum_{p=0}^{M-1}\left[\frac{2\cdot\mathrm{E}[f_p]\cdot\mathrm{E}\left[\hat{f}_p\right]+C_1}{\mathrm{E}\left[f_p^2\right]+\mathrm{E}\left[\hat{f}_p^2\right]+C_1} \cdot \frac{2\cdot\mathrm{Cov}\left[f_p,\hat{f}_p\right]+C_2}{\mathrm{Var}[f_p]+\mathrm{Var}\left[\hat{f}_p\right]+C_2}\right]$	f_p, $\hat{f}_p$, $p = 0,\ldots,M-1$: speckle–free and despeckled image patches; C_1, C_2: suitable constants.
$\mathrm{EC} = \frac{\mathrm{Cov}\left[f^H,\hat{f}^H\right]}{\sqrt{\mathrm{Var}[f^H]\cdot\mathrm{Var}\left[\hat{f}^H\right]}}$	f^H, $\hat{f}^H$: highpass–filtered speckle–free and despeckled images
$\mathrm{FOM} = \frac{1}{\max(\hat{N},N)}\sum_{n=1}^{\hat{N}}\frac{1}{1+d_n^2\alpha}$	N, $\hat{N}$: number of points belonging to an edge in speckle–free and despeckled image patches; d_n^2: Euclidean distance between the edge pixels in the despeckled image patch and the nearest ideal edge pixel in the speckle–free one; α: suitable constant.

Table 6.2: *Performances of with–reference indexes obtained on* San Francisco *corrupted with 1–look speckle noise*

	ideal	noisy	GG MAP-S	LG MAP-S	PPB	SAR–BM3D
PSNR	∞	19.02	26.08	26.13	24.73	26.00
MSSIM	1	0.411	0.707	0.709	0.696	0.724
EC	1	0.279	0.372	0.397	0.304	0.374
FOM	1	0.133	0.302	0.285	0.282	0.286

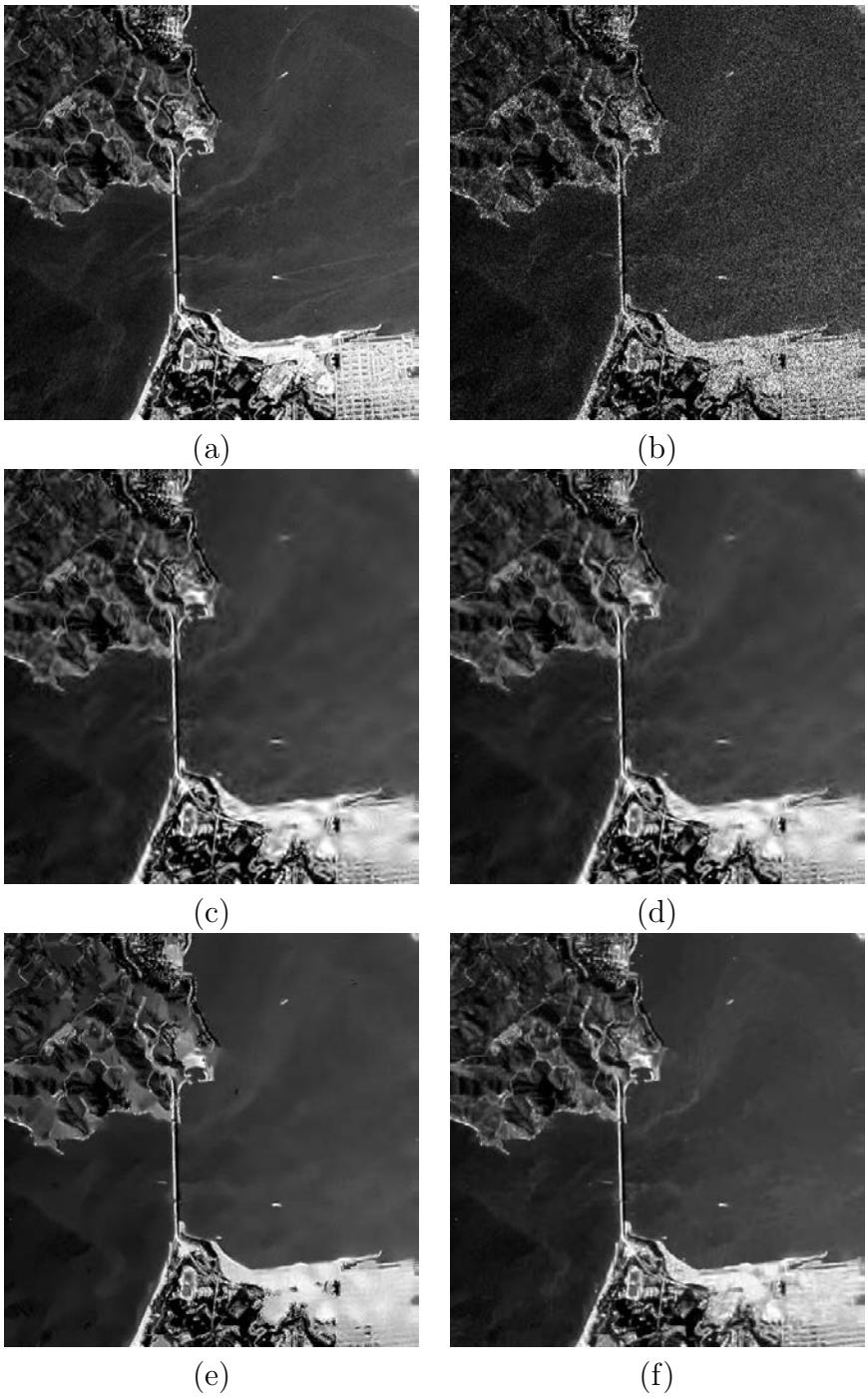

Figure 6.1: *Results on* San Francisco *corrupted with 1–look synthetic speckle noise: (a) noise-free reference; (b) noisy (1-look); (c) GG MAP-S; (d) LG MAP-S; (e) PPB; (f) SAR–BM3D.*

Table 6.3: *Performances of with–reference indexes obtained on* San Francisco *corrupted with 4–look speckle noise*

	ideal	noisy	GG MAP-S	LG MAP-S	PPB	SAR–BM3D
PSNR	∞	24.67	28.93	29.37	27.60	29.06
MSSIM	1	0.668	0.806	0.815	0.782	0.820
EC	1	0.515	0.635	0.657	0.522	0.632
FOM	1	0.255	0.426	0.469	0.460	0.471

tions. The ENL is defined as

$$\mathrm{ENL} = \frac{\mathrm{E}\left[\hat{f}\right]^2}{\mathrm{Var}\left[\hat{f}\right]}. \tag{6.8}$$

The ENL of the original SAR image is related to the nominal number of looks through the autocorrelation function of speckle [79], whereas it increases after the despeckling stage according to the smoothing capability of the filter.

Other typical measures can be computed from the *ratio image* r, defined as the point–by–point ratio between the noisy and the filtered image [17]

$$r(n) = \frac{g(n)}{\hat{f}(n)}. \tag{6.9}$$

The ratio image is a useful information in both homogeneous and heterogeneous scenes, wherever fully developed speckle model holds. It represents the noise pattern removed by the despeckling filter that, according to the model, should be Γ-distributed. An ideal filter should result in a pure random pattern, whereas poor speckle noise removal causes structural informations, such as borders and edges, to be clearly visible in the ratio image. The mean and the variance of r, that is

$$\mu_r = \mathrm{E}[r], \qquad \sigma_r^2 = \mathrm{Var}[r] \tag{6.10}$$

should be as close as possible to the respective theoretical statistical moments of the speckle noise process. For this reason, they are often used as indexes of bias and speckle power suppression, respectively.

A *measure of bias* is also given by the B index [19],defined as

$$\mathrm{B} = \mathrm{E}\left[\frac{(g - \hat{f})}{g}\right], \tag{6.11}$$

where a value close to zero indicates an unbiased estimation.

Under the hypothesis of multiplicative speckle noise, a measure of texture preservation on heterogeneous areas is given by the comparison between the *scene coefficient of variation* $C_{\hat{f}}$, defined as

$$\mathrm{C}_{\hat{f}} = \frac{\sqrt{\mathrm{Var}\left[\hat{f}\right]}}{\mathrm{E}\left[\hat{f}\right]}, \tag{6.12}$$

with its expected theoretical value C_f [11], given by

$$\mathrm{C}_f = \sqrt{\frac{C_I^2 - C_u^2}{1 + C_u^2}}, \tag{6.13}$$

where C_I and C_u are the coefficient of variations of the observed image and of the speckle noise, respectively. Intuitively, a poor preservation of details yields $C_S > C_F$, while the introduction of strong artefacts leads to $C_S < C_F$.

Since the speckle model does not hold in the presence of strong scatterers or point targets, despeckling filters should keep their values unchanged. A point target is usually characterized by a cluster of pixels whose reflectivity values are much higher, even some orders of magnitude, than the mean reflectivity of the surrounding scene. The *target–to–clutter ratio* (TCR) [80, 81] aims at measuring the relative value of strong scatterers with respect to the values of the surrounding pixels. It is defined as

$$\mathrm{TCR} = 20 \log_{10} \frac{\max_{\mathcal{P}}[g]}{\mathrm{E}_{\mathcal{P}}[g]}, \tag{6.14}$$

where $\mathcal{P}$ is a patch containing a point target. TCR values computed before and after the despeckling stage are indicative about how a filter preserves the radiometric properties in the patch.

Table 6.4 summarizes the most commonly used without-reference indexes for evaluating despeckling algorithms performance.

Fig. 6.2 reports the visual results obtained by filtering an original 1024×1024 1–look StripMap COSMO–SkyMed SAR image representing *Cascine*, an area of Florence. The relative without–reference indexes are presented in Table 6.5; ENL, μ_r and σ_r^2 have been computed in the zone indicated by "A" in Fig. 6.2, $\mathrm{C}_{\hat{f}}$ has been computed in "B", TCR in "C", while B has been computed on the whole image. PPB filter scores the best results for all indexes but B. On the other side, the relative visual result looks like artificial

Table 6.4: *List of commonly used without-reference indexes for evaluating performances of despeckling algorithms.*

Index	Note
$\mathrm{ENL} = \frac{\mathrm{E}\left[\hat{f}\right]^2}{\mathrm{Var}\left[\hat{f}\right]}$	f, $\hat{f}$: speckle–free and despeckled images; ENL is evaluated in homogeneous areas
$\mu_r = \mathrm{E}[r]$, $\sigma_r^2 = \mathrm{Var}[r]$	$r(n) = \frac{g(n)}{\hat{f}(n)}$: ratio image
$\mathrm{B} = \mathrm{E}\left[\frac{(g-\hat{f})}{g}\right]$	
$\mathrm{C}_{\hat{f}} = \frac{\sqrt{\mathrm{Var}\left[\hat{f}\right]}}{\mathrm{E}\left[\hat{f}\right]}$	$\mathrm{C}_f = \sqrt{\frac{C_g^2 - C_u^2}{1+C_u^2}}$ (expected value); C_g, C_u: coefficients of variation of the observed noisy image g and of the speckle noise u
$\mathrm{TCR} = 20\log_{10}\frac{\max_{\mathcal{P}}[g]}{\mathrm{E}_{\mathcal{P}}[g]}$	$\mathcal{P}$: patch containing a point target; $\max_{\mathcal{P}}$, $\mathrm{E}_{\mathcal{P}}$ computed over the patch

due to the *mosaic* behaviour which is typical of this kind of filter.

Table 6.5: *Performances of without–reference indexes obtained on* Cascine

	ideal	noisy	GG MAP-S	LG MAP-S	PPB	SAR–BM3D
ENL	∞	1.05	29.36	22.15	82.14	13.56
μ_r	1	1.000	0.926	0.914	0.940	0.919
σ_r^2	1	0.000	0.651	0.607	0.719	0.527
B	0	0.000	-4.086	-3.980	-3.978	-3.431
$\mathrm{C}_{\hat{f}}$	0.355	1.119	0.458	0.448	0.321	0.580
TCR	48.238	48.238	47.964	48.017	48.148	48.106

A 512×512 4–look version of the same image has been also generated by means of spatial multilooking (that is, applying a 2×2 box filter and a subsampling by 2 in both range–azimuth directions). The resulting indexes are presented in Table 6.6. PPB filter still exhibits an outperforming ENL. Interestingly, the ENL of the noisy image is not 4 as expected, because both the randomness of the noise realization and the not perfect homogeneity of the scene in the zone "A". GG MAP-S and LG MAP-S now achieve the best performances in terms of bias avoidance (μ_r and σ_r^2, respectively). This fact is explained by considering that the multilooking process reduces the correlation of speckle and allow all filter to operate in more ideal hypotheses.

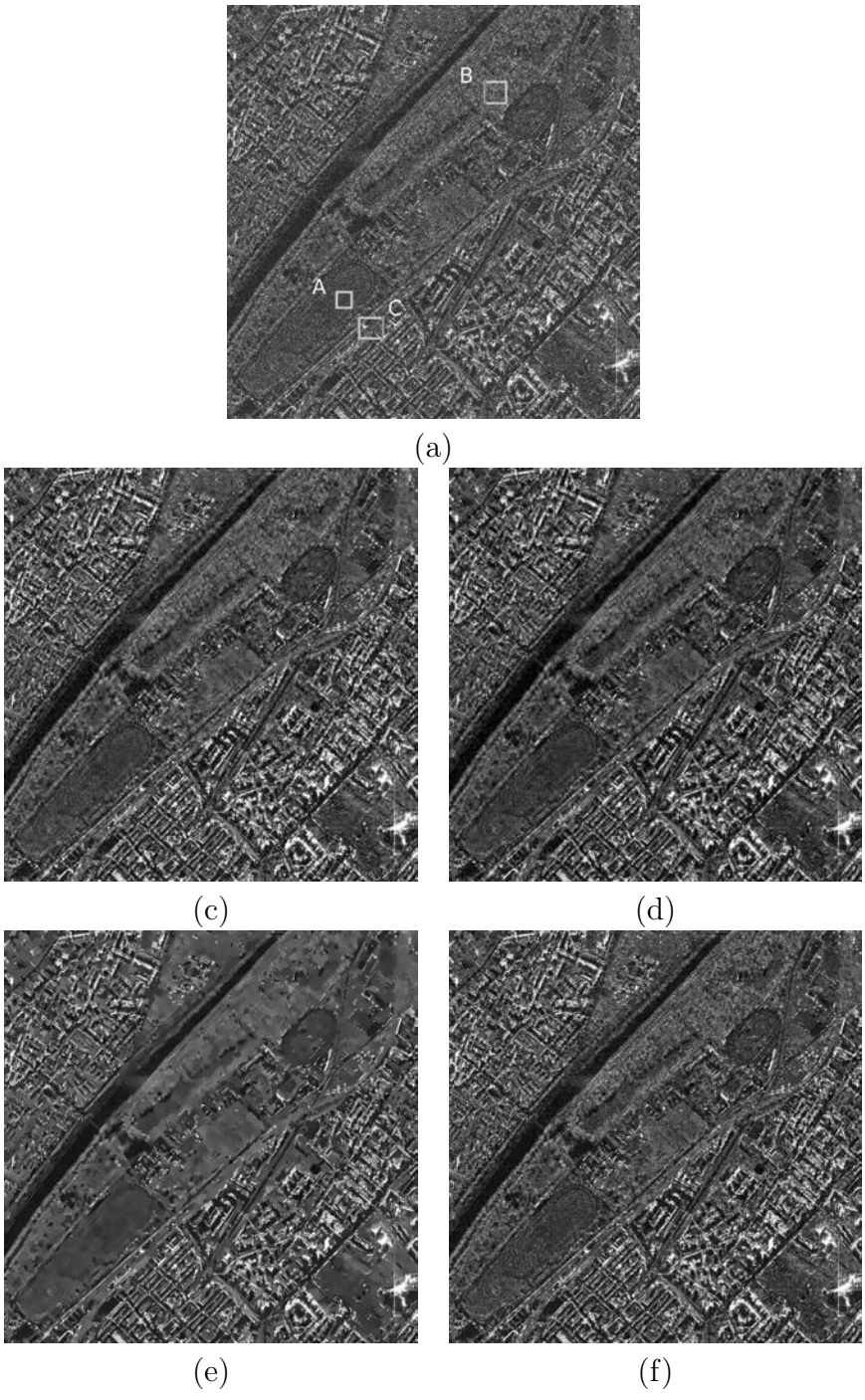

Figure 6.2: *Results on* Cascine*, an 1–look StripMap COSMO–SkyMed SAR image: (a) original, with highlighted interesting zones; (b) GG MAP-S; (c) LG MAP-S; (d) PPB; (e) SAR–BM3D.*

Table 6.6: *Performances of without–reference indexes obtained on 4–L version of* Cascine

	ideal	noisy	GG MAP-S	LG MAP-S	PPB	SAR–BM3D
ENL	∞	2.49	31.79	26.86	220.80	20.54
μ_r	1	1.000	0.999	0.986	0.980	0.941
σ_r^2	0.25	0.000	0.263	0.237	0.309	0.157
B	0	0.000	-0.359	-0.345	-0.425	-0.320
C_F	0.544	0.788	0.395	0.389	0.354	0.477
TCR	43.001	43.001	42.949	42.992	42.982	42.964

6.2 The unsupervised change detection feature

6.2.1 Motivations and rationale for a new quality assessment index

From the discussion developed in Section 6.1, it emerges that the evaluation of the quality of despeckling is a difficult task. With–reference indexes can be used by corrupting a test image by means of synthetic noise with speckle statistics and computing a distance metrics between the original noise free and the filtered noisy image. Unfortunately this approach is correct only for scenes where speckle is fully developed. In the presence of natural textures, e.g., forests, and of man-made structures, e.g., roads together with buildings, the fully developed speckle model no longer holds. As a limit case, a persistent scatterer produces an almost deterministic image, without any speckle.

Since despeckling filters should be optimized on true SAR images, where speckle may not be fully developed on textured areas, the problem arises even if the evaluation is performed by means of the most popular without–references indexes. Indeed, no indexes is capable to evaluate the behaviour of filtering on textures, where speckle may be not fully developed. Hence, the evaluation on such areas is usually carried out only by visual inspection.

Another important issue is that evaluation indexes are often supervised. For instance, let's consider the ratio of the original to the despeckled image (e.g. [11]), which is taken on suitable manually chosen regions of interest

(ROI), where speckle is assumed to be fully developed; then its statistics (e.g. mean, variance, correlation, skewness) are matched to the nominal ones of speckle. Unfortunately, suitable regions may not be available on such images (e.g. highly textured areas as cities) or they could be even wrongly chosen by the supervisor, yielding to misleading results.

Goal of this section is the development and evaluation of a fully automatic method for quality assessment of despeckled SAR images. The rationale of the proposed approach is that any structural perturbation introduced by despeckling, e.g. a local bias of mean or the blur of a sharp edge or the suppression of a point target, may be regarded as the introduction of a new structure, or the suppression of an existing one. Conversely, plain removal of random noise does not changes the structures in the image. Implementation of the new method is performed on the two-dimensional scatterplot between local means of the filtered and unfiltered image, or equivalently on the bivariate distribution obtained after binning. An ideally optimal filter would yield a scatterplot constituted by the superposition of several clusters, corresponding to classes encountered in the image. The ensemble of clusters is aligned along the diagonal of the first quadrant and spread across the plane far apart from the diagonal, where, however, all centers of clusters lie. The presence of filtering impairments produce secondary clusters that may be significantly far apart from the diagonal. Under this perspective, a measure of the accuracy of despeckling for each pixel may be formulated in the following way. For each point in the scatterplot, corresponding to one pixel in the original and in the filtered image, apply the mean shift algorithm to attract the scatterpoint towards its dominant cluster. If the final position of the point is on the diagonal, the corresponding pixel in the image has been correctly filtered. If the scatterpoint is attracted by a secondary cluster not lying on the diagonal, filtering was inaccurate. A measure of such inaccuracy is given in terms of the offset of the attracting cluster from the main diagonal. A fast implementation is obtained by preliminarily binning the scatterplot and by applying the mean shift algorithm to the central scatterpoint of each bin.

In the following, after validating the proposed feature by means of simulated speckled images, results on true SAR images are presented. Bayesian estimators presented in 63 and operating in the undecimated wavelet domain are considered for experimental results. Quality measurements of despeckled SAR images carried out by means of the proposed method are discussed exploiting visual comparisons.

6.2.2 Description of algorithm

The key of the proposed change detection feature is to define a statistical feature measuring the degree of impairment undergone by the SAR image after filtering. The problem may be stated a a structural change detection between original and filtered image. Actually all pixels in the filtered image are changed with respect to the original because speckle noise has been removed. Hence the original and filtered images are statistically different but should be structurally similar.

The rationale is that ideally, the scatterplot of despeckled to original image should contain clouds of points, whose gravity centers lie along the main diagonal. Whenever this does not occur, filtering moves clusters of scatterpoints far from the diagonal, same as if changes were occurred between original and filtered images. The offset of a cluster from the main diagonal is a measure on the amount of change occurred.

All joint probabilities are calculated by quantizing the 2D histogram (scatterplot) of locally windowed backscatters values according to the following procedure:

1. Let $g_1(m,n)$ and $g_2(m,n)$ denote noisy and denoised SAR images, respectively.

2. Local averaging with Gaussian windowing

   - Compute the square root of the Gaussian-weighted local means of pixel intensities: $\overline{g_1}(m,n)$ and $\overline{g_2}(m,n)$, over a $(2p+1)\times(2p+1)$ sliding window (best trade-off is $p=3$)

3. Scatter plot

   - Report $\overline{g_2}(m,n)$ against $\overline{g_1}(m,n)$ in a scatter plot

4. Quantization (binning) ($L=512$ or $L=256$)

   - Partition the scatterplot plane into $L\times L$ blocks, obtaining a 2D histogram $h(i,j)$, $i \leftrightarrow \overline{g_2}$ and $j \leftrightarrow \overline{g_1}$

5. Normalization

   - Normalize the scatterplot to the overall number of points $\Rightarrow$ approximated discrete joint pdf $\hat{p}(i,j) \sim p(\overline{g_2}, \overline{g_1})$

6. Clustering & migration

- Apply mean-shift clustering [82] to $\hat{p}(i,j)$ bins by adopting a flat kernel of radius 3/2 (1.5 times the bin size), obtaining a map $q(i,j)$ of clusters' gravity centers
- Each point $p(i,j)$ is now associated to one and only one cluster; be w the vector function which binds each point (i,j) of p to the gravity center (i',j') of the corresponding cluster $q(i',j')$: $(i',j') = w(i,j)$

7. Compute the pixel change feature $\mathcal{C}(m,n)$, for each pixel (m,n):

$$\mathcal{C}(m,n) = j' - i', \quad \text{where } (i',j') = w(i,j) = w\left(\lfloor \overline{g_2}(m,n) \rfloor, \lfloor \overline{g_1}(m,n) \rfloor\right)$$

   - whenever $j' > i'$, the change feature $\mathcal{C}(m,n)$ is by excess
   - whenever $j' < i'$, the change feature $\mathcal{C}(m,n)$ is by defect.

8. The two maps of changes by excess and by defect can be superimposed to obtain a unique change map, or kept separate.

The size of the Gaussian sliding window and the resolution of binning represent two important settings which have to be considered to balance between stability and sensitivity of the final feature. Indeed, a smaller window and/or a finest binning allow a more accurate joint pdf to be obtained, at the cost of a nosier 2D histogram, that is, more modes are likely to appear. On the contrary, a greater window and/or a coarser binning can lead to a smoother 2D histogram, but at risk resolution loss.

Mean shift clustering is necessary to detect the clusters' gravity centers, which are the main modes of the joint pdf. The number of clusters and their sizes can be set by modifying the radius of the flat kernel: the greater the radius, the lower the number of clusters and, consequently, the bigger their sizes. It follows that, in case of too big radius, closer clusters that would be naturally separated are more likely to merge, altering the change measure. Similarly, a lower radius implies an increased number of smaller clusters; a too small radius would fragment valid clusters, leading to wrong bindings and wrong change measures. Hence, the radius dimension is also a key parameter which represents a trade-off between stability and sensitivity of the measure.

Finally, it should be noted that the measure of change is actually represented by the vertical offset between a cluster center and the main diagonal. A possible alternative to this is choice is represented, for instance, by the Euclidean distance between the cluster center and the main diagonal. Metrics based on concepts of information theory, such as Kullback–Leibler divergence, could be also exploited. However, according to our tests, the vertical

offset between a cluster center and the main diagonal has pointed out the most interesting results.

6.2.3 Experimental results

Simulated speckled data

A synthetically speckled image has been produced starting from a 512 × 512, 8–bit, digitized aerial photograph of San Francisco. The original noise-free image, regarded as an amplitude format, has been squared and multiplied by an exponentially distributed fading term, in order to simulate a single-look SAR image in intensity format. The simulated speckle is spatially uncorrelated and fully developed. The noisy intensity image, together with all filtered intensity versions, has been gamma-corrected, namely square rooted, for displaying convenience and is shown together with the 8-bit original, regarded as an amplitude image, in Fig. 6.3.

Despeckling filters that have been compared are all based on undecimated wavelet transform: LMMSE [35], GG MAP-S [41], MAP-LG and LG MAP-S. Biorthogonal 9/7 wavelet filters and four levels of decomposition have been used in all despeckling filters. For each filtered version, the error map (pixel difference map between filtered noisy version and noise-free original) has been calculated. Its positive values indicate that filtering has introduced a change by excess; negative values a change by defect.

Table 6.7 report values for the following parameters:

- ρ: correlation coefficient between the error map and the structural change map;
- ρ_+: correlation coefficient between the error map and the structural change map (only positive part of both);
- σ^2_C: global variance of the structural change map;
- $\sigma^2_{C,+}$: global variance of the structural change map (only positive part);
- σ^2_E: global variance of the error map;
- $\sigma^2_{E,+}$: global variance of the error map (only positive part).

Concerning the error between noise-free and filtered images, it is evident that segmentation is rewarding. The LMMSE estimator in [35] includes a multiscale adjustment to scene heterogeneity, which is substantially a rough segmentation. The MAP-LG method provides the poorest results. The GG MAP-S method is far the best, closely followed by LG MAP-S.

Fig. 6.4, Fig. 6.5 and Fig. 6.6 show filtered noisy test image, map of error between noise-free original and filtered noisy version and change map between noisy version and filtered noisy version, respectively, for the four despeckling filters that are compared. The structural change feature exhibits a significant correlation with the error map. Correlation is even better between the positive values of change and the positive values of error. In Figs. 6.5 and 6.6, positive values are shown in light gray, while negative values in dark gray. Table 6.7 highlights that correlation between change and error is around 0.6 and reaches value over 0.7 when negative values of error and feature are removed. The ranking of filtering methods based on the variance of positive values of change is identical to the ranking based on the variance of positive error values. The variance of positive change is different from zero for the original image, unlike what one would expect; however its value is far lower than that of any other filtered image.

(a) (b)

Figure 6.3: *Simulated image of San Francisco (*512×512*): (a) original; (b) speckled, single-look.*

COSMO-SkyMed data

A true X-band SAR image produced by the COSMO-SkyMed satellite constellation has been processed for despeckling. The image has been acquired and processed in HImage Stripmap mode and is stored as a single-look complex format. The detected intensity image, having spatial resolution of approximately three meters and nominal SNR equal to 0 dB, contains both natural and man-made structures. It is believed to provide a challenging

	ρ	ρ_+	σ^2_C	$\sigma^2_{C,+}$	σ^2_E	$\sigma^2_{E,+}$
Original	-	-	0.502	0.273	-	-
LMMSE	0.599	0.693	1.158	0.891	44.02	29.17
MAP-LG	0.649	0.716	1.201	0.911	51.65	36.80
LG MAP-S	0.584	0.661	1.088	0.786	41.10	27.21
GG MAP-S	0.537	0.607	0.982	0.693	37.98	24.26

Table 6.7: *Results on simulated image of San Francisco.*

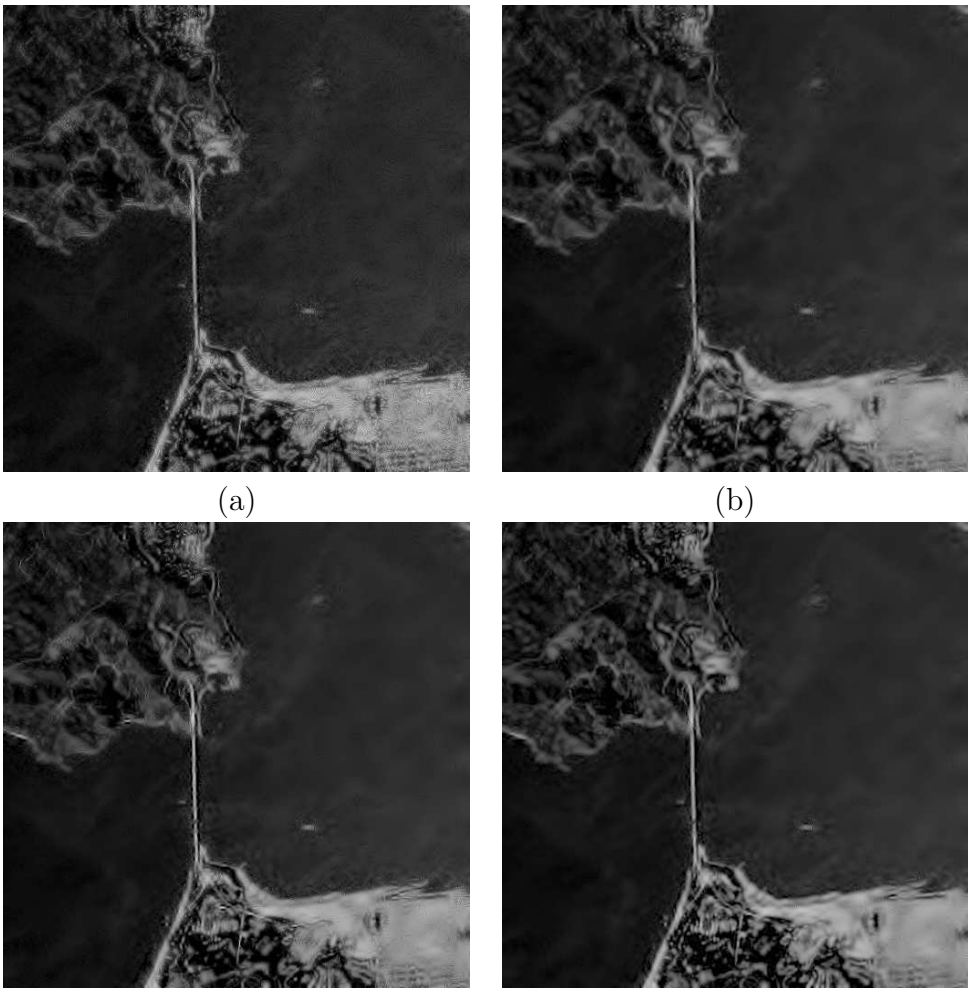

(a) (b) (c) (d)

Figure 6.4: *Results obtained despeckling the San Francisco image: (a) LMMSE; (b) MAP-LG; (c) LG MAP-S; (d) GG MAP-S.*

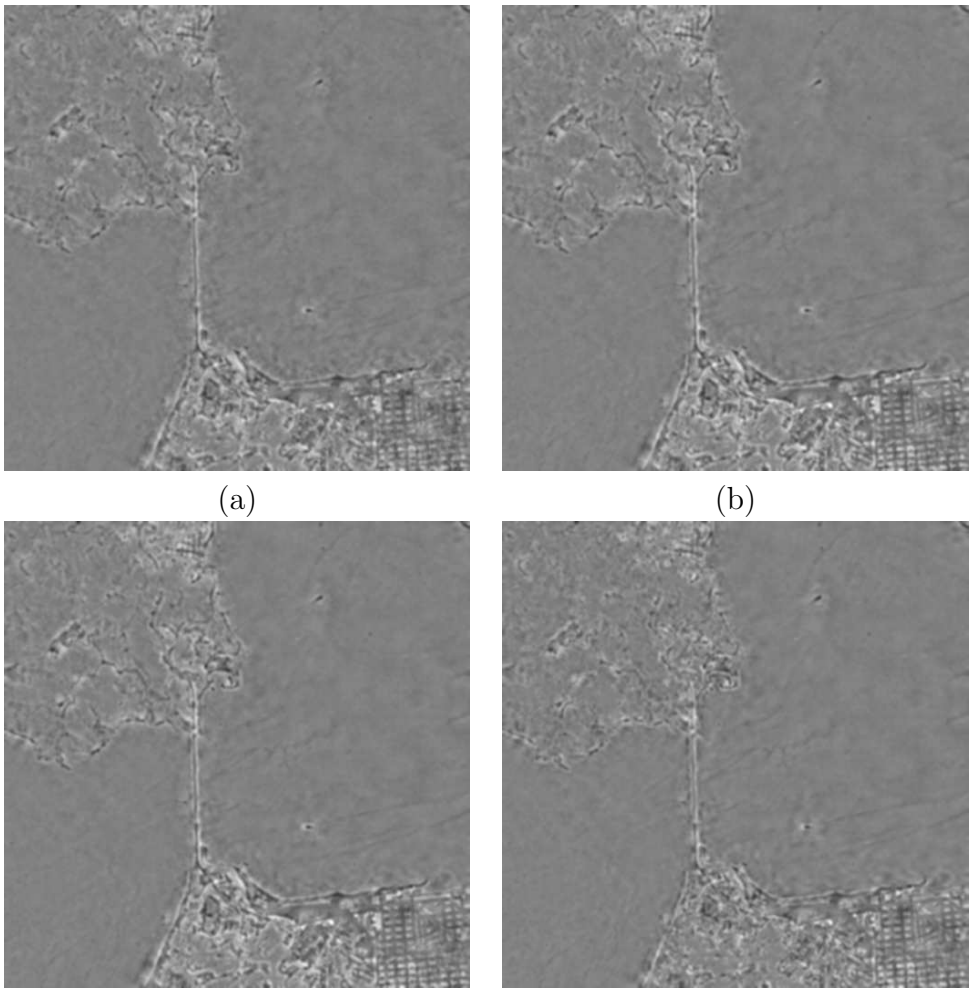

(a) (b)

(c) (d)

Figure 6.5: *Error map on the San Francisco image measured with respect to the original image: (a) LMMSE; (b) MAP-LG; (c) LG MAP-S; (d) GG MAP-S.*

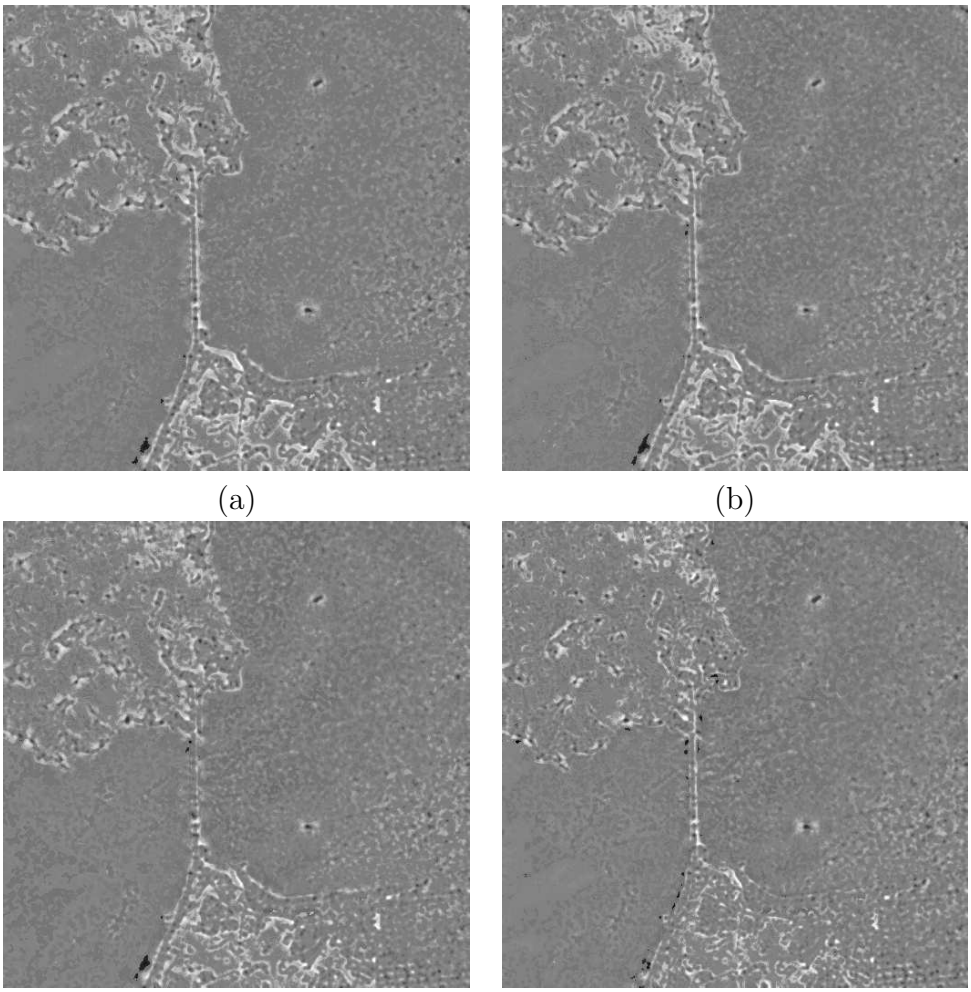

(a) (b)

(c) (d)

Figure 6.6: *Structural change map on the San Francisco image obtained with the proposed algorithm: (a) LMMSE; (b) MAP-LG; (c) LG MAP-S; (d) GG MAP-S.*

subject for despeckling, being the worst case that can be encountered. Two different scenes of the same image, featuring different types and amounts of texture and point targets, are shown in Fig. 6.7.

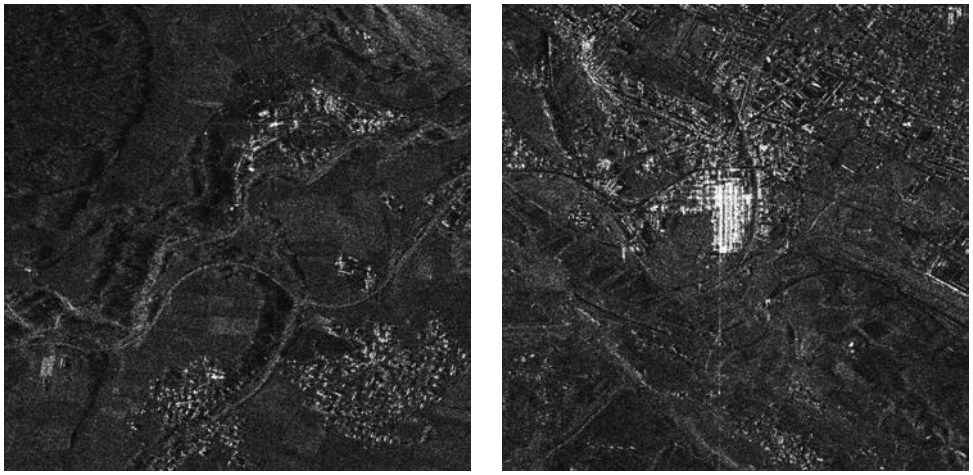

(a) (b)

Figure 6.7: *Single-look SAR images from COSMO-SkyMed (*1024 × 1024*, 3m pixel size, amplitude format): (a) CS-1; (b) CS-2.*

Table 6.8 reports variances of change feature σ_C^2 and of positive part of change feature $\sigma_{C,+}^2$ for the two Cosmo-SkyMed images. Differences in accuracy of methods follow a trend similar to that in Table 6.7. The sole exception is that LMMSE is now ranked second instead of third. The explanation is that LMMSE [35] is not a plain LMMSE estimator in undecimated wavelet domain, but contains adjustments specifically devised for true SAR images, which are ineffective for simulated SAR images. The ranking of methods still highlights that GG MAP-S provides the most accurate despeckling and that the sole scheme not exploiting segmentation (MAP-LG) is the poorest. Interestingly, the second image CS-2 is more textured and hence its changes are larger than those of CS-1, but the ranking of methods stemming from the proposed feature is identical for the two images.

The visual comparison of the filtered images in Figs. 6.8 and 6.10 show that all methods are comparable in performances, even though GG MAP-S, seems to be slightly more accurate on textures. The maps of the proposed feature, shown in Figs. 6.9 and 6.11, highlight that the GG MAP-S filtered image is the least impaired and that the second image CS-2, being more textured, is less accurately filtered than CS-1, in average.

	CS-1		CS-2	
	σ_C^2	$\sigma_{C,+}^2$	σ_C^2	$\sigma_{C,+}^2$
LMMSE	0.185	0.116	0.287	0.183
MAP-LG	0.227	0.146	0.367	0.246
LG MAP-S	0.205	0.138	0.353	0.224
GG MAP-S	0.174	0.109	0.303	0.166

Table 6.8: *Variances of change feature for filtered COSMO-SkyMed images.*

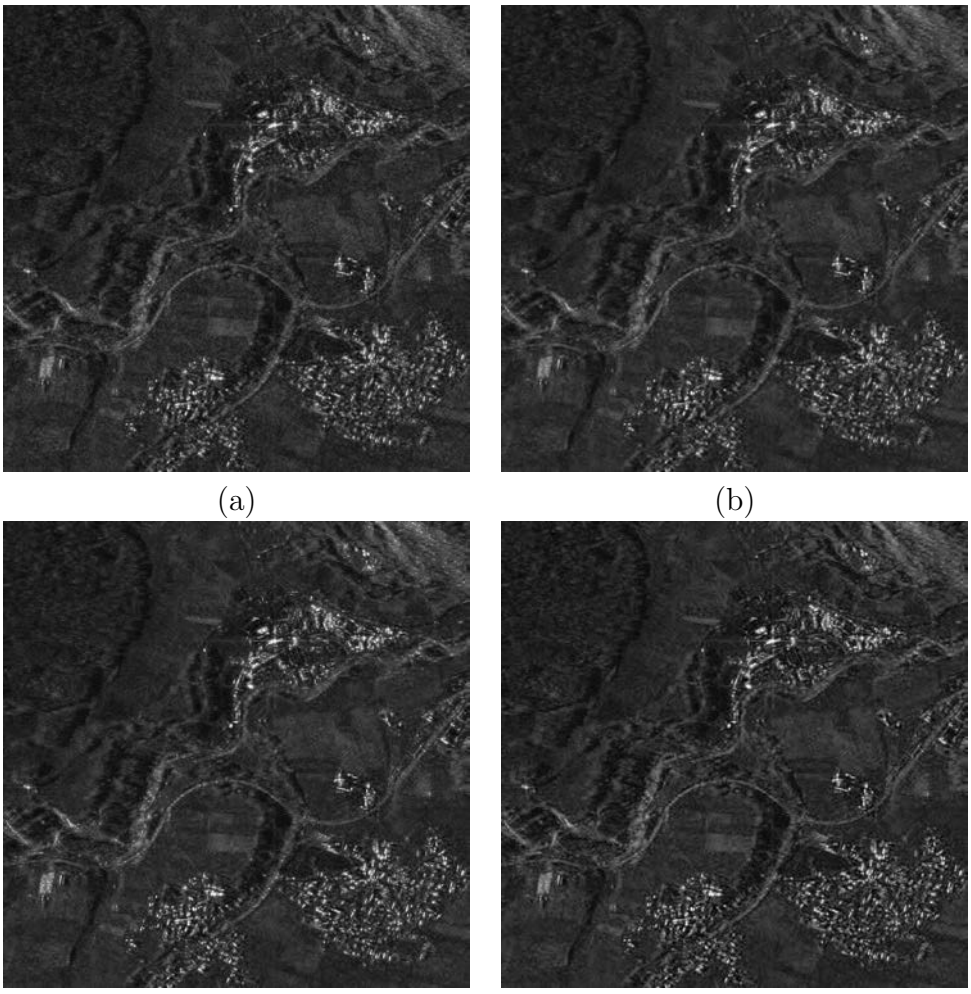

(a) (b) (c) (d)

Figure 6.8: *Results obtained by despeckling the COSMO-SkyMed image CS-1: (a) LMMSE; (b) MAP-LG; (c) LG MAP-S; (d) GG MAP-S.*

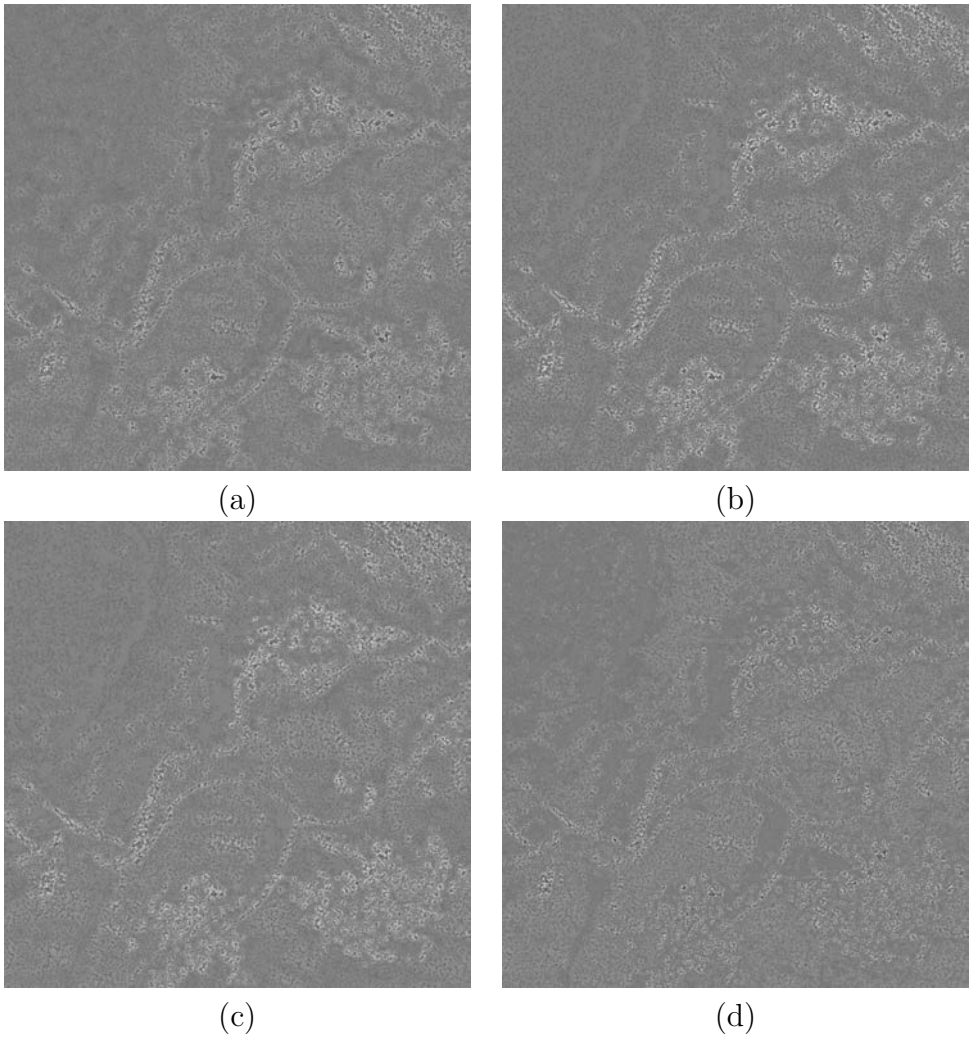

Figure 6.9: *Structural change map of the filtered COSMO-SkyMed image CS-1: (a) LMMSE; (b) MAP-LG; (c) LG MAP-S; (d) GG MAP-S.*

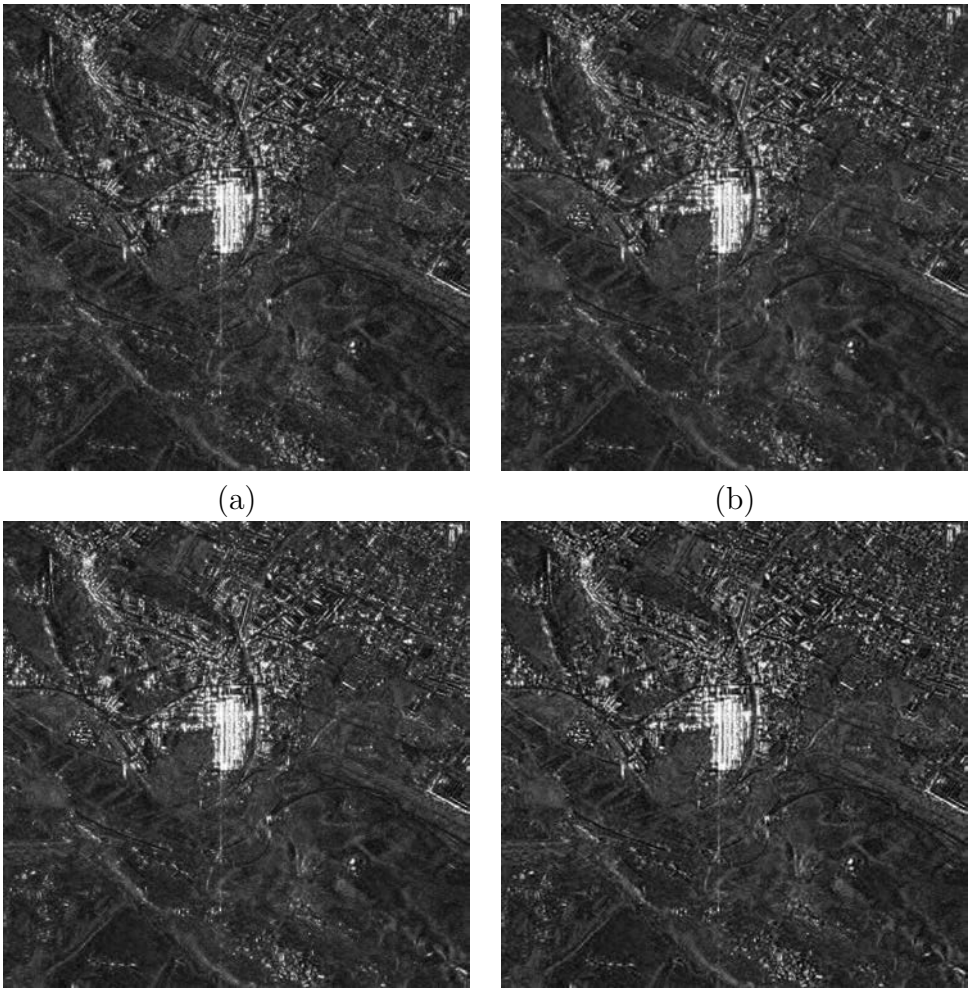

(a) (b) (c) (d)

Figure 6.10: *Results obtained by despeckling the COSMO-SkyMed image CS-2: (a) LMMSE; (b) MAP-LG; (c) LG MAP-S; (d) GG MAP-S.*

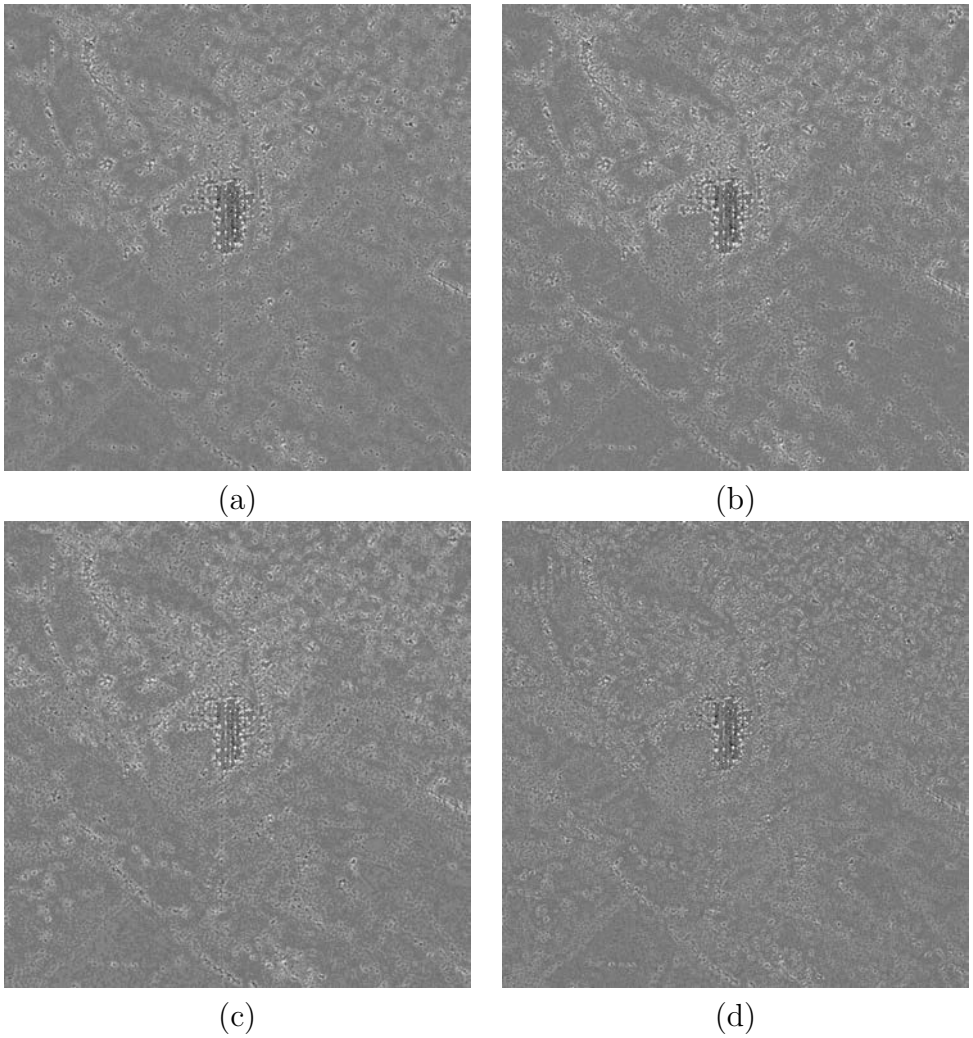

Figure 6.11: *Structural change map of the filtered COSMO-SkyMed image CS-2: a) LMMSE; b) MAP-LG; c) LG MAP-S; d) GG MAP-S.*

6.3 Conclusions

The assessment of the performances of despeckling filters on real SAR data is often problematic due to the lack of with–reference indexes. Without–reference indexes have been used in the literature by several authors, but they are valid only in areas where the signal have specific statistical properties. Moreover, the supervision of an expert is required.

In order to overcome such problems, a possible idea (not discussed in this thesis) is to use electromagnetic SAR image generators [83]. Such simulators are based on more physical–oriented models, which consider the propagation of the electromagnetic wave and its interaction with targets and surfaces, and usually require a more detailed parametric description of the target scene with respect to the models used in signal processing applications. In [84, 85], the authors use an electromagnetic SAR image generator to simulate several independent acquisitions of the same scene. If the number of acquisitions is sufficiently high, their average can be considered as a good approximation of the noise-free reflectivity and can be used to compute with–reference indexes. The advantage of this technique is that the simulated images do not necessarily obey the fully developed speckle model and provide insights on the behaviour of the filter on point targets and highly heterogeneous areas. On the other hand, the underlying reflectivity follows a synthetically generated pattern, which may not be fully representative of the reflectivity usually encountered in real SAR images, especially in complex scenes, due to the ideal models of objects fed to the simulator.

In this thesis, a viable alternative approach based on a novel change feature has been devised to measure despeckling impairments. It relies on the joint probability density function of the amplitude values of original and despeckled SAR images and exploits the mean–shift clustering algorithm to improve detection of filtering inaccuracies. A preliminary validation has been carried out on simulated SAR images, with a good correlation between the proposed feature and the objective filtering error. Experiments on Stripmap Cosmo-SkyMed images (single look) have highlighted that the automatic ranking of filtering methods matches subjective trials of experts. The proposed feature detects filtering impairments but is unable to measure the overall effectiveness of filtering. Therefore its use must be coupled with another method measuring the effectiveness of noise cleaning, regardless of its accuracy.

Chapter 7

Conclusions

Different thematics inherently the despeckling of SAR images have been examined in depth during the three years of the Ph.D. course. In the last two decades, despeckling has generally experienced a dramatic increasing of interest from the scientific community, mainly thanks to the introduction of the multiresolution analysis. The key features of despeckling in the multiresolution domain is represented by the higher degree of freedom in statistical characterization of coefficients than in the spatial domain, where strict constraints due to the physical model are unavoidable.

Since the advent of the first wavelets-based despeckling filters it has been clear that the new tools could ensure a considerable performance boost. Nevertheless, two different approaches have been developed. Several authors have chosen overfitting models sacrificing space adaptivity, while others have tried to keep the advantages of an adaptivity in both scale and space by using pdf with few parameters to be estimated locally on subbands/frames. In this thesis, Bayesian estimators in the undecimated wavelet domain have been discussed and proposed according to the latter approach. A preprocessing step of point targets that must retain their radiometry after despeckling and a segmented approach, in which sample statistics are calculated on homogeneous segments, complete Bayesian despeckling in wavelet domain.

In the literature, further improvements have been demonstrated to be achievable by introducing the concept of segmentation in the wavelet domain. By following this idea, a strategy based on adopting different fast despeckling filters according to classification of texture has been successfully proposed and discussed.

As previously stated, Bayesian estimators in the transformed domain allow to overcome the statistical constraints present in the spatial domain. Specifically, each pdf model of wavelet coefficients can be reasonably assumed valid independently of different image formats. A unified framework

for different image formats have been presented and it has been shown that artefacts due to undecimated wavelet synthesis stage can be effectively reduced by using the square root of intensity instead of intensity.

The problem of removal of correlated speckle has been also addressed. It is known that despeckling filters usually exhibit performance losses due to the focusing window applied to the complex SAR signal, which introduces correlation in the speckle process. A common solution is represented by the multilooking processing, which allows to trade-off resolution loss with lower power and correlation of speckle noise. As an alternative, a preprocessing stage, which aims to whiten the speckle by estimating and inverting the focusing window system, has been developed. Experimental results have shown that, when such a whitening stage is used, noticeable performance improvements are achievable by different kinds of already known despeckling filters.

By now, the state-of-the-art despeckling methods are consolidated and validated. Some improvements of already know filters have been recently proposed in order to slightly increase filtering effectiveness and/or efficiency. New research fields, such as compressive sensing for despeckling, are presently under investigation, but no noticeable performance boosts have been obtained so far. On the other side, the problem of quality assessment for despeckling filters is still open. A fully-automatic method based on the measure of change between noisy image and filtered one has been presented; it has been shown to be able to detect local impairments occurred in real SAR images after despeckling, even though overall effectiveness must be evaluated also by means of global indexes.

References

[1] F. Argenti, A. Lapini, T. Bianchi, and L. Alparone, "A tutorial on speckle reduction in synthetic aperture radar images," *IEEE Geoscience and Remote Sensing Magazine*, vol. 1, no. 3, pp. 6–35, 2013.

[2] F. Argenti, T. Bianchi, A. Lapini, and L. Alparone, "Fast MAP despeckling based on Laplacian–Gaussian modeling of wavelet coefficients," *IEEE Geoscience and Remote Sensing Letters*, vol. 9, no. 1, pp. 13–17, Jan. 2012.

[3] F. Argenti, T. Bianchi, A. Lapini, and L. Alparone, "Bayesian despeckling of SAR images based on Laplacian–Gaussian modeling of undecimated wavelet coefficients," in *Proc. IEEE Int. Conf. on Acoustics, Speech and Signal Processing (ICASSP)*, 2011, pp. 1445–1448.

[4] F. Argenti, T. Bianchi, A. Lapini, and L. Alparone, "Simplified MAP despeckling based on Laplacian-Gaussian modeling of undecimated wavelet coefficients," in *Proc. 19th European Signal Processing Conf. (EUSIPCO)*, 2011, pp. 1140–1144.

[5] T. Bianchi, F. Argenti, A. Lapini, and L. Alparone, "Amplitude vs intensity Bayesian despeckling in the wavelet domain for SAR images," *Digital Signal Processing*, , no. 5, pp. 1353–1362, Sep. 2013.

[6] T. Bianchi, F. Argenti, A. Lapini, and L. Alparone, "Amplitude vs intensity despeckling in the wavelet domain using Bayesian estimators," in *Proc. Tyrrhenian Workshop on Advances in Radar and Remote Sensing*, 2012, pp. 267–274.

[7] A. Lapini, T. Bianchi, F. Argenti, and L. Alparone, "Blind speckle decorrelation for SAR image despeckling," *IEEE Transactions on Geoscience and Remote Sensing*, vol. 52, no. 2, pp. 1044–1058, 2014.

[8] A. Lapini, T. Bianchi, F. Argenti, and L. Alparone, "Blind whitening of correlated speckle to enforce despeckling of single-look high-resolution SAR images," in *SAR Image Analysis, Modeling, and Techniques XII*, 2012, vol. 8537 of *Proc. of SPIE*, pp. 85370Z–85370Z–8.

[9] A. Lapini, T. Bianchi, F. Argenti, and L. Alparone, "Blind whitening of correlated speckle to enforce despeckling of single-look high-resolution SAR images," in *Proc. SPIE 8537, Image and Signal Processing for Remote Sensing XVIII*, Nov. 2012, vol. 8537, p. 85370Z.

[10] B. Aiazzi, L. Alparone, F. Argenti, S. Baronti, T. Bianchi, and A. Lapini, "An unsupervised method for quality assessment of despeckling: an evaluation on COSMO-SkyMed data," 2011, vol. 8197 of *Proc. of SPIE*, pp. 81790D–81790D–10.

[11] R. Touzi, "A review of speckle filtering in the context of estimation theory," *IEEE Transactions on Geoscience and Remote Sensing*, vol. 40, no. 11, pp. 2392–2404, Nov. 2002.

[12] C. Elachi and J. J. van Zyl, *Introduction To The Physics and Techniques of Remote Sensing*, John Wiley & Sons, Hoboken, NJ, 2006.

[13] F. T. Ulaby, R. K. Moore, and A. K. Fung, *Microwave Remote Sensing: Active and Passive, Volume II: Radar Remote Sensing and Surface Scattering and Emission Theory*, Artech House, Norwood, MA, 1986.

[14] J. W. Goodman, "Some fundamental properties of speckle," *J. Opt. Soc. Am.*, vol. 66, no. 11, pp. 1145–1150, Nov. 1976.

[15] M. Tur, K. C. Chin, and J. W. Goodman, "When is speckle multiplicative?," *Applied Optics*, vol. 21, no. 7, pp. 1157–1159, Apr. 1982.

[16] J. C. Curlander and R. N. McDonough, *Synthetic Aperture Radar: Systems & Signal Processing*, John Wiley & Sons, New York, 1991.

[17] C. Oliver and S. Quegan, *Understanding Synthetic Aperture Radar Images*, Artech House, Boston, MA, 1998.

[18] S. N. Madsen, "Spectral properties of homogeneous and nonhomogeneous radar images," *IEEE Transactions on Aerospace and Electronic Systems*, vol. AES-23, no. 4, pp. 583–588, Jul. 1987.

[19] S. Solbø and T. Eltoft, "A stationary wavelet-domain Wiener filter for correlated speckle," *IEEE Transactions on Geoscience and Remote Sensing*, vol. 46, no. 4, pp. 1219–1230, Apr. 2008.

[20] A. Lapini, T. Bianchi, F. Argenti, and L. Alparone, "A whitening method for the despeckling of SAR images affected by correlated speckle noise," in *Proc. 20th European Signal Processing Conf. (EUSIPCO)*, 2012, pp. 2487–2491.

[21] H. H. Arsenault and M. Levesque, "Combined homomorphic and local-statistics processing for restoration of images degraded by signal-dependent noise," *Appl. Optics*, vol. 23, no. 6, pp. 845–850, Mar. 1984.

[22] H. Xie, L. E. Pierce, and F. T. Ulaby, "Statistical properties of logarithmically transformed speckle," *IEEE Transactions on Geoscience and Remote Sensing*, vol. 40, no. 3, pp. 721–727, Mar. 2002.

[23] I. Daubechies, "Orthonormal bases of compactly supported wavelets," *Commun. Pur. Appl. Math.*, vol. 41, pp. 909–996, 1988.

[24] S. Mallat, "A theory for multiresolution signal decomposition: the wavelet representation," *IEEE Transactions on Pattern Analysis and Machine Intelligence*, vol. PAMI-11, no. 7, pp. 674–693, Jul. 1989.

[25] S. M. Kay, *Fundamentals of Statistical Processing, Volume I: Estimation Theory*, Prentice Hall, Engl. Cliffs, NJ, 1993.

[26] M. J. Shensa, "The discrete wavelet transform: wedding the à trous and Mallat algorithms," *IEEE Transactions on Signal Processing*, vol. 40, no. 10, pp. 2464–2482, Oct. 1992.

[27] G. P. Nason and B. W. Silverman, "The stationary wavelet transform and some statistical applications," in *Wavelets and Statistics*, A. Antoniadis and G. Oppenheim, Eds., vol. 103 of *Lecture Notes in Statistics*, pp. 281–299. Springer-Verlag, New York, 1995.

[28] F. Argenti G. Torricelli and L. Alparone, "Signal dependent noise removal in the undecimated wavelet domain," in *Proc. IEEE Int. Conf. on Acoustics, Speech and Signal Processing (ICASSP)*, 2002, vol. 4, pp. 3293–3296.

[29] P. P. Vaidyanathan, *Multirate Systems and Filter Banks*, Prentice Hall, Engl. Cliffs, NJ, 1992.

[30] Minh N. Do and M. Vetterli, "The contourlet transform: An efficient directional multiresolution image representation," *IEEE Transactions on Image Processing*, vol. 14, no. 12, pp. 2091–2106, Dec. 2005.

[31] E. Candès and D. Donoho, "Curvelets – a surprisingly effective nonadaptive representation for objects with edges," in *Curves and Surface Fitting: Saint-Malo 1999*, A. Cohen, C. Rabut, and L. Schumaker, Eds. 2000, pp. 105–120, Vanderbilt University Press.

[32] J. L. Starck, E. J. Candès, and D. L. Donoho, "The curvelet transform for image denoising," *IEEE Transactions on Image Processing*, vol. 11, no. 6, pp. 670–684, Jun. 2002.

[33] F. Argenti, T. Bianchi, G. Martucci di Scarfizzi, and L. Alparone, "LMMSE and MAP estimators for reduction of multiplicative noise in the nonsubsampled contourlet domain," *Signal Processing*, vol. 89, no. 10, pp. 1891–1901, Oct. 2009.

[34] L. Alparone, F. Argenti, T. Bianchi, and A. Lapini, "An evaluation of Bayesian estimators and PDF models for despeckling in the undecimated wavelet domain," in *SAR Image Analysis, Modeling, and Techniques X*, C. Notarnicola, Ed., 2010, vol. 7829 of *Proc. of SPIE*, pp. 782902–1–782902–12.

[35] F. Argenti and L. Alparone, "Speckle removal from SAR images in the undecimated wavelet domain," *IEEE Transactions on Geoscience and Remote Sensing*, vol. 40, no. 11, pp. 2363–2374, Nov. 2002.

[36] F. Argenti, T. Bianchi, and L. Alparone, "Multiresolution MAP despeckling of SAR images based on locally adaptive generalized Gaussian PDF modeling," *IEEE Transactions on Image Processing*, vol. 15, no. 11, pp. 3385–3399, Nov. 2006.

[37] S. Foucher, G. B. Bénié, and J.-M. Boucher, "Multiscale MAP filtering of SAR images," *IEEE Transactions on Image Processing*, vol. 10, no. 1, pp. 49–60, Jan. 2001.

[38] D. L. Donoho, "Denoising by soft-thresholding," *IEEE Transactions on Information Theory*, vol. 41, no. 3, pp. 613–627, Mar. 1995.

[39] R. Coifman and D. L. Donoho, "Translation-invariant de-noising," in *Wavelets and Statistics*, A. Antoniadis, Ed., Lecture Notes. Springer-Verlag, Berlin, Heidelberg, New York, 1995.

[40] H. Rabbani, M. Vafadust, P. Abolmaesumi, and S. Gazor, "Speckle noise reduction of medical ultrasound images in complex wavelet domain using mixture priors," *IEEE Transactions on Biomedical Engineering*, vol. 55, no. 9, pp. 2152–2160, Sep. 2008.

[41] T. Bianchi, F. Argenti, and L. Alparone, "Segmentation-based MAP despeckling of SAR images in the undecimated wavelet domain," *IEEE Transactions on Geoscience and Remote Sensing*, vol. 46, no. 9, pp. 2728–2742, Sep. 2008.

[42] A. Lopès, E. Nezry, R. Touzi, and H. Laur, "Maximum a posteriori speckle filtering and first order texture models in SAR images," in *Proc. IEEE Int. Geoscience and Remote Sensing Symp. (IGARSS)*, 1990, pp. 2409–2412.

[43] A. Lopès, R. Touzi, and E. Nezry, "Adaptive speckle filters and scene heterogeneity," *IEEE Transactions on Geoscience and Remote Sensing*, vol. 28, no. 6, pp. 992–1000, Nov. 1990.

[44] B. Aiazzi, L. Alparone, S. Baronti, and A. Garzelli, "Coherence estimation from incoherent multilook SAR imagery," *IEEE Transactions on Geoscience and Remote Sensing*, vol. 41, no. 11, pp. 2531–2539, Nov. 2003.

[45] Jong-Sen Lee, I. Jurkevich, P. Dewaele, P. Wambacq, and A. Oosterlinck, "Speckle filtering of synthetic aperture radar images: a review," *Remote Sens. Rev.*, vol. 8, no. 4, pp. 313–340, 1994.

[46] E.A. Carvalho, D.M. Ushizima, F.N.S. Medeiros, C.I.O. Martins, R.C.P. Marques, and I.N.S. Oliveira, "SAR imagery segmentation by statistical region growing and hierarchical merging," *Digital Signal Processing*, vol. 20, no. 5, pp. 1365 – 1378, 2010.

[47] S. Solbø and T. Eltoft, "Homomorphic wavelet-based statistical despeckling of SAR images," *IEEE Transactions on Geoscience and Remote Sensing*, vol. 42, no. 4, pp. 711–721, Apr. 2004.

[48] M. Amirmazlaghani, H. Amindavar, and A. Moghaddamjoo, "Speckle suppression in SAR images using the 2-D GARCH model," *IEEE Transactions on Image Processing*, vol. 18, no. 2, pp. 250 – 259, feb 2009.

[49] Biao Hou, Xiaohua Zhang, Xiaoming Bu, and Hongxiao Feng, "SAR image despeckling based on nonsubsampled shearlet transform," *IEEE Journal of Selected Topics in Applied Earth Observations and Remote Sensing*, vol. 5, no. 3, pp. 809 – 823, june 2012.

[50] A. Achim, A. Bezerianos, and P. Tsakalides, "Novel Bayesian multiscale method for speckle removal in medical ultrasound images," *IEEE Transactions on Medical Imaging*, vol. 20, no. 8, pp. 772–783, Aug. 2001.

[51] S. Gupta, L. Kaur, R. C. Chauhan, and S. C. Saxena, "A versatile technique for visual enhancement of medical ultrasound images," *Digital Signal Processing*, vol. 17, no. 3, pp. 542–560, May 2007.

[52] Fabien Chaillan, Christophe Fraschini, and Philippe Courmontagne, "Speckle noise reduction in SAS imagery," *Signal Processing*, vol. 87, no. 4, pp. 762 – 781, 2007.

[53] M.I.H. Bhuiyan, M.O. Ahmad, and M.N.S. Swamy, "Spatially adaptive thresholding in wavelet domain for despeckling of ultrasound images," *IET Image Processing*, vol. 3, no. 3, pp. 147 –162, june 2009.

[54] Ashish Khare, Manish Khare, Yongyeon Jeong, Hongkook Kim, and Moongu Jeon, "Despeckling of medical ultrasound images using Daubechies complex wavelet transform," *Signal Processing*, vol. 90, no. 2, pp. 428–439, 2010.

[55] V. S. Frost, J. A. Stiles, K. S. Shanmugan, and J. C. Holtzman, "A model for radar images and its application to adaptive digital filtering of multiplicative noise," *IEEE Transactions on Pattern Analysis and Machine Intelligence*, vol. PAMI-4, no. 2, pp. 157–166, Feb. 1982.

[56] M. G. Kendall and A. Stuart, *The Advanced Theory of Statistics*, vol. 1, Charles Griffin & Co., Ltd., London, UK, 4th edition, 1977.

[57] C.-A. Deledalle, L. Denis, and F. Tupin, "Iterative weighted maximum likelihood denoising with probabilistic patch-based weights," *IEEE Transactions on Image Processing*, vol. 18, no. 12, pp. 2661–2672, Dec. 2009.

[58] Zhou Wang, A. C. Bovik, H. R. Sheikh, and E. P. Simoncelli, "Image quality assessment: from error visibility to structural similarity," *IEEE Transactions on Image Processing*, vol. 13, no. 4, pp. 600–612, Apr. 2004.

[59] I. Daubechies, *Ten Lectures on Wavelets*, vol. 61 of *CBMS-NSF Reg. Conf. Series Appl. Math.*, SIAM, Philadelphia, PA, 1992.

[60] D. T. Kuan, A. A. Sawchuk, T. C. Strand, and P. Chavel, "Adaptive restoration of images with speckle," *IEEE Transactions on Acoustics, Speech, and Signal Processing*, vol. ASSP-35, no. 3, pp. 373–383, Mar. 1987.

[61] O.V. Michailovich and A. Tannenbaum, "Despeckling of medical ultrasound images," *IEEE Transactions on Ultrasonics, Ferroelectrics, and Frequency Control*, vol. 53, no. 1, pp. 64–78, Jan. 2006.

[62] A. Wong and P. Fieguth, "A new Bayesian source separation approach to blind decorrelation of SAR data," in *Proc. IEEE Int. Geoscience and Remote Sensing Symp. (IGARSS)*, July 2010, pp. 4035–4038.

[63] D. Kundur and D. Hatzinakos, "Blind image deconvolution revisited," *IEEE Signal Processing Magazine*, vol. 13, no. 6, pp. 61–63, Nov. 1996.

[64] G. R. Ayers and J. C. Dainty, "Iterative blind deconvolution method and its applications," *Optics Letters*, vol. 13, pp. 547–549, July 1988.

[65] A. C. Likas and N. P. Galatsanos, "A variational approach for Bayesian blind image deconvolution," *IEEE Transactions on Signal Processing*, vol. 52, no. 8, pp. 2222–2233, Aug. 2004.

[66] D. Iraca, L. Landini, and L. Verrazzani, "Power spectrum equalization for ultrasonic image restoration," *IEEE Transactions on Ultrasonics, Ferroelectrics, and Frequency Control*, vol. 36, no. 2, pp. 216–222, Mar. 1989.

[67] M. H. Hayes, *Statistical digital signal processing and modeling*, Wiley, New York, 1996.

[68] Italian Space Agency (ASI), *COSMO-SkyMed SAR Products Handbook*, 2007.

[69] G.H. Golub and C.F. Van Loan, *Matrix Computations*, Johns Hopkins Studies in the Mathematical Sciences. Johns Hopkins University Press, 1996.

[70] B. R. Hunt, "The application of constrained least squares estimation to image restoration by digital computer," *IEEE Transactions on Computers*, vol. C-22, no. 9, pp. 805–812, Sept. 1973.

[71] M. Walessa and M. Datcu, "Model-based despeckling and information extraction from SAR images," *IEEE Transactions on Geoscience and Remote Sensing*, vol. 38, no. 5, pp. 2258–2269, Sep. 2000.

[72] A. Achim, E. E. Kuruoglu, and J. Zerubia, "SAR image filtering based on the heavy-tailed Rayleigh model," *IEEE Transactions on Image Processing*, vol. 15, no. 9, pp. 2686–2693, Sep. 2006.

[73] F. Sattar, L. Floreby, G. Salomonsson, and B. Lovstrom, "Image enhancement based on a nonlinear multiscale method," *IEEE Transactions on Image Processing*, vol. 6, no. 6, pp. 888–895, Jun. 1997.

[74] A. Achim, P. Tsakalides, and A. Bezerianos, "SAR image denoising via Bayesian wavelet shrinkage based on heavy-tailed modeling," *IEEE Transactions on Geoscience and Remote Sensing*, vol. 41, no. 8, pp. 1773–1784, Aug. 2003.

[75] W. K. Pratt, *Digital Image Processing*, J. Wiley & Sons, New York, 1991.

[76] Yongjian Yu and S. T. Acton, "Speckle reducing anisotropic diffusion," *IEEE Transactions on Image Processing*, vol. 11, no. 11, pp. 1260–1270, Nov. 2002.

[77] S. Parrilli, M. Poderico, C. V. Angelino, and L. Verdoliva, "A nonlocal SAR image denoising algorithm based on LLMMSE wavelet shrinkage," *IEEE Transactions on Geoscience and Remote Sensing*, vol. 50, no. 2, pp. 606–616, Feb. 2012.

[78] Jong-Sen Lee, "Speckle analysis and smoothing of synthetic aperture radar images," *Comput. Graph. Image Process.*, vol. 17, no. 1, pp. 24–32, Sep. 1981.

[79] B. Aiazzi, L. Alparone, F. Argenti, S. Baronti, T. Bianchi, and A. Lapini, "An experimental setup for multiresolution despeckling of COSMO-SkyMed image products," in *SAR Image Analysis, Modeling, and Techniques XII*, 2012, vol. 8536 of *Proc. of SPIE*, pp. 853603–853603–6.

[80] G. R. Benitz, "High-definition vector imaging," *Lincoln Lab. J.*, vol. 10, no. 2, pp. 147–170, 1997.

[81] M. Çetin, W. C. Karl, and D. A. Castañon, "Evaluation of a regularized SAR imaging technique based on recognition-oriented features," in *Algorithms for Synthetic Aperture Radar Imagery VII*, 2000, vol. 4053 of *Proc. of SPIE*, pp. 40–51.

[82] Yizong Cheng, "Mean shift, mode seeking, and clustering," *IEEE Transactions on Pattern Analysis and Machine Intelligence*, vol. 17, no. 8, pp. 790–799, 1995.

[83] G. Franceschetti, M. Migliaccio, D. Riccio, and G. Schirinzi, "SARAS: a synthetic aperture radar SAR raw signal simulator," *IEEE Transactions on Geoscience and Remote Sensing*, vol. 30, no. 1, pp. 110–123, Jan. 1992.

[84] G. Di Martino, M. Poderico, G. Poggi, D. Riccio, and L. Verdoliva, "SAR image simulation for the assessment of despeckling techniques," in *Proc. IEEE Int. Geoscience and Remote Sensing Symp. (IGARSS)*, 2012, pp. 1797–1800.

[85] G. Di Martino, M. Poderico, G. Poggi, D. Riccio, and L. Verdoliva, "Benchmarking framework for SAR despeckling," *IEEE Transactions on Geoscience and Remote Sensing*, Article in Press.